THE UNIVERSITY *of* EDINBURGH

Simplified Kinetic Modelling of Polyatomic Gases and Liquid-Vapour Flows

Shaokang Li

Doctor of Philosophy

THE UNIVERSITY OF EDINBURGH

2025

Abstract

The relentless miniaturization of technology has pushed fluid dynamics into previously unexplored territories at the micro- and nanoscale. In these domains, micro- and nano-electromechanical systems (MEMS and NEMS) encounter unique fluid behaviors, particularly rarefaction effects, which fundamentally affect their performance. Traditional modelling approaches face a critical dilemma: continuum models, such as the Navier-Stokes equations, fail to capture these phenomena, while molecular dynamics (MD) simulations, though accurate, remain computationally intractable for practical applications. Kinetic theory bridges this gap by providing an efficient framework for capturing these effects. It offers a statistical framework for describing the behavior of large numbers of particles in terms of a distribution function, i.e. the probability of particles having particular velocities and positions at a given time. The cornerstone of kinetic theory is the Boltzmann equation, a fundamental tool that captures the evolution of distribution functions through its two components: a free-stream term, which describes the motion of particles under external forces, and a collision term, which accounts for interactions between molecules. While the Boltzmann equation is well-suited for rarefied monatomic gases, extensions such as the Rykov equation for polyatomic gases and the Enskog equation for dense gases address more complex conditions by incorporating additional effects in the collision term. However, the original Boltzmann equation is a highly complex nonlinear integro-differential equation, and its extensions are even more intricate, making them challenging to apply in practical engineering contexts. This thesis focuses on developing simplified kinetic models for polyatomic gases and liquid-vapour flows, validating these models against experimental and MD simulation results, and exploring their applicability across a variety of engineering scenarios.

In the first part of this thesis, a simplified kinetic model for polyatomic gases is developed and applied to the numerical study of sound waves generated by a vibrating plate in a rarefied polyatomic gas environment confined within microchannels. The goal is to accurately capture gas damping, particularly the surface forces acting on the plates of MEMS devices. Unlike monatomic gases, polyatomic gases exhibit bulk viscosity, and both translational and rotational degrees of freedom contribute to their thermal conductivity. To understand the effects of these two transport coefficients, sound wave propagation is studied over a wide range of rarefaction conditions and plate vibration frequencies. The results reveal that bulk viscosity significantly influences the pressure amplitude (equivalent to the surface force) and the resonance frequency, primarily in the slip flow regime at high oscillation frequencies. Additionally, at high bulk viscosity, the internal degrees of freedom are effectively frozen, causing the pressure amplitude of sound waves in a polyatomic gas to resemble that of a monatomic gas. In contrast, thermal conductivity has a limited effect on the pressure amplitude across

all simulated conditions. For thermoacoustic waves, the study confirms the validity of the Onsager-Casimir reciprocal relation (OCRR) for polyatomic gases, demonstrating that the pressure deviation induced by temperature changes equals the heat flux generated by plate vibrations. Validating this relation enhances simulation efficiency by reducing the required number of kinetic coefficients and provides an additional criterion for numerical accuracy.

Building on the work involving polyatomic gases, this thesis transitions to the kinetic modelling of liquid-vapour flows, which are critical for NEMS applications such as cooling systems and water desalination membranes. A simplified kinetic model is developed to simulate nanoscale evaporation processes, striking a balance between computational efficiency and accuracy. This model captures the entire flow field, encompassing both the liquid and vapour phases as well as their interface. Unlike previous models that predominantly assumed isothermal conditions, this model accounts for temperature variations during evaporation. The model's validity is demonstrated through three benchmark cases: liquid-vapour equilibrium, evaporation into near-vacuum conditions, and evaporation into a vapour environment. The results show excellent agreement with benchmark solutions, with a significant reduction in computation time of almost two orders of magnitude, without compromising accuracy.

The final part of the thesis extends the one-dimensional modelling of liquid-vapour flows to two dimensions and examines droplet ripening—a near-equilibrium process in which larger droplets grow at the expense of smaller ones. This process, which is poorly understood at the micro- and nanoscale, where interfacial-bulk interactions dominate, has significant implications for natural phenomena and technological applications, such as cloud formation and nanomaterial synthesis. The results reveal that the primary driving force behind droplet growth is the pressure difference between the vapour phase and the droplets. Notably, the rate of change in droplet size is found to be linear with the Laplace pressure when the small droplet has a bulk region, while non-linear effects emerge when the bulk region disappears. Furthermore, the slope of the rate of change in the linear regime increases exponentially with temperature, independent of droplet number or arrangement.

This thesis contributes to the development of simplified kinetic models for polyatomic gases and liquid-vapour flows, providing new insights into sound wave propagation, one-dimensional non-equilibrium evaporation, and two-dimensional droplet ripening. The findings offer a foundation for advancing kinetic modelling techniques, with important implications for both fundamental research and engineering applications.

Lay Summary

Micro- and nano-electro-mechanical systems (MEMS and NEMS) have revolutionized modern technology, enabling precise drug delivery, thermal management in microelectronics, and advanced gas sensing. At these microscopic scales, fluid behavior defies conventional understanding as molecular interactions dominate over bulk flow phenomena. Traditional fluid dynamics models, such as the Navier-Stokes equations, fail to capture this essential molecular physics, whereas molecular dynamics (MD) simulations, though accurate, remain computationally prohibitive for practical engineering applications. This gap calls for a middle ground: kinetic theory modelling that balances computational efficiency with the ability to capture the essential physics of small-scale systems. However, the standard kinetic equations that from the mathematical basis remain computationally expensive for the engineering problems mentioned. Therefore, developing simplified kinetic models is essential to improving their practicality.

This thesis focuses on developing simplified kinetic models to study polyatomic gases and liquid-vapour flows, which are central to many advanced technologies. The first part of this thesis focuses on sound wave propagation in polyatomic gases, which is important for applications like MEMS devices, where sound wave damping can significantly impact performance. Unlike monatomic gases (such as helium), polyatomic gases have internal energy modes, including molecular rotation and stretching, that affect their behaviour. Using a simplified kinetic equation, this work shows how bulk viscosity which acts as internal friction within a molecule resisting changes in shape or size, and thermal conductivity affect sound wave behaviour. For instance, at high frequencies, bulk viscosity can "freeze" molecular vibrations, making the gas behave more like a monatomic gas. These findings provide insights not only for MEMS design but also for broader applications involving sound wave manipulation in molecularly confined systems.

The second part investigates nanoscale evaporation, a critical process for technologies such as cooling systems in electronics and water desalination membranes. Evaporation at such scales is far from the idealized, steady process we imagine; temperature variations and fluid interactions at the liquid-vapour interface play a major role. This work introduces a simplified kinetic model that captures these effects while avoiding the computational cost of complex simulations. The model is validated against benchmarks, showing excellent accuracy and achieving simulation times two orders of magnitude faster. These advancements make it possible to optimize evaporation processes for practical applications and improve the efficiency of systems relying on nanoscale heat and mass transfer.

The third part extends the study to droplet ripening, a process in which larger droplets grow at the expense of smaller ones. This phenomenon is fundamental to applications ranging from cloud formation and material synthesis to the stability of emulsions in food and cosmetics. By extending the evaporation model to two dimensions, this work shows how pressure differences between droplets and the surrounding vapour drive growth. The results highlight that temperature plays a crucial role, with the rate of droplet growth increasing exponentially with temperature. These findings deepen the understanding of droplet formation at micro- and nanoscale levels and provide tools for controlling this process across industrial applications.

In summary, this thesis develops and applies simplified kinetic models to capture flow behaviour at scales where conventional approaches fail. By balancing the detailed accuracy of molecular descriptions with the computational efficiency of engineering approximations, the work advances our ability to analyze and design technologies that operate at the micro- and nanoscale, such as MEMS and NEMS devices.

Acknowledgements

I would like to extend my deepest gratitude to all those who have supported me throughout this rewarding and demanding PhD journey. Their encouragement, insight, and thoughtful guidance have been indispensable in overcoming the challenges faced along the way. As I move forward, I carry with me the knowledge, experiences, and perspectives shared by those who have contributed to this work. Each individual, through their unique influence, has helped shape the ideas and accomplishments presented in this thesis.

First and foremost, I would like to express my heartfelt gratitude to my principal supervisor, Prof. Yonghao Zhang. His profound insights into the field of gas kinetic theory have consistently inspired my research and guided me to the forefront of key scientific issues. Moreover, he has always been prompt and attentive in addressing my queries and resolving my doubts whenever I sought assistance, for which I am deeply grateful. I would also like to extend my sincere thanks to Dr. Livio Gibelli, who became my principal supervisor in the second year of my PhD project. We have had numerous fruitful discussions about my research topics. He has been instrumental in guiding me through complex mathematical and physical concepts. I am truly grateful to both of my supervisors for their unwavering support and invaluable guidance throughout my academic journey.

I would like to express my sincere gratitude to my friends and colleagues, both within the Multiscale Flow X group and beyond, for their engaging discussions and friendship. The conversations and collaborative exchanges have greatly enriched my research experience. I am also deeply grateful to my family and lifelong friends for their unwavering love and belief throughout the challenges of this academic journey. Your support has given me the emotional strength to overcome obstacles and persist through tough times.

This thesis is a reflection of not only my efforts but also the collective support and encouragement of those around me. To everyone who has played a role in this journey, thank you from the bottom of my heart.

Contents

Figures and Tables

Figures

Tables

Chapter 1

Introduction

Fluid flow modelling faces increasing challenges as technologies advance to microscopic scales where traditional continuum approaches are no longer sufficient. Indeed, the rise of micro- and nanoscale applications requires more sophisticated tools to capture molecular-level phenomena. Kinetic models have bridged this gap by incorporating molecular collision dynamics while remaining computationally simpler than full molecular dynamics simulations (Section 1.1). Originally developed for rarefied monatomic gases, these models have evolved to handle more complex scenarios, including polyatomic gases and dense gas flows. Their practical value has been demonstrated in a wide range of engineering applications, from microfluidic devices to hypersonic vehicles (Section 1.2). However, as kinetic models become more sophisticated to capture the complexity of the real world, they also become increasingly computationally intensive. This computational burden drives the central aim of this thesis (Section 1.3): to develop efficient numerical methods that preserve the accuracy of extended kinetic models while making them more practical for engineering applications.

1.1 Overview of Approaches in Fluid Modelling

Fluid dynamics spans multiple spatial scales, from macroscopic to microscopic. At the molecular level, the statistical outcomes of particle collisions determine observable fluid properties such as density, velocity, temperature and pressure. These collisions dictate the exchange of momentum, energy, and mass, shaping the overall flow behaviour. The mean free path λ is a fundamental concept that refers to the average distance a molecule travels between successive collisions with other molecules. It quantifies how far molecules move, on average, before their trajectories are interrupted by interactions. For an ideal gas composed of hard spheres, λ can be calculated using

$$\lambda = \frac{1}{\sqrt{2}\pi\sigma^2 n}, \tag{1.1}$$

where σ is the molecular diameter, and n is the number density, defined as the number of molecules per unit volume. The ratio of the molecular mean free path λ to a characteristic flow length H, known as the Knudsen number (Kn), is a key parameter for identifying flow regimes and selecting the appropriate modelling approach:

$$Kn = \frac{\lambda}{H}. \tag{1.2}$$

Flow regimes are typically classified based on the Kn number as follows: continuum flow ($Kn \lesssim 0.001$), slip flow ($0.001 \lesssim Kn \lesssim 0.1$), transition flow ($0.1 \lesssim Kn \lesssim 10$), and free molecular flow ($Kn \gtrsim 10$). The reduced number density, defined as $\eta = \frac{\pi}{6} n\sigma^3$, becomes necessary alongside Kn to guide fluid modelling for non-ideal gases, especially when $Kn \gtrsim 0.1$. A regime map, shown in Figure 1.1, provides a reference for selecting the appropriate, most computationally efficient technique for modelling hard-sphere fluids under different flow conditions. For small Kn, the continuum assumption holds, and macroscopic equations such as the Navier-Stokes equations are applicable. As Kn increases, non-equilibrium effects become significant. In the slip flow regime, the Navier-Stokes equations with slip boundary conditions can still be used to capture some non-equilibrium effects. However, in the transition and free molecular regimes, the Navier-Stokes framework breaks down, requiring mesoscale modelling via the Boltzmann equation for dilute gases. At higher densities, the Enskog equation provides a more accurate description for the moderately dense gases, while at very high densities, molecular-scale approaches such as event-driven molecular dynamics simulations become necessary. The following section provides a brief introduction to these modelling approaches.

1.1.1 Continuum Models

In the continuum regime, the characteristic flow length is much larger than the molecular mean free path, allowing the fluid to reach a local thermodynamic equilibrium state. In this state, the macroscopic properties change smoothly in space and time due to frequent molecular collisions. The fluid behaviour in this regime is governed by the balance of mass, momentum, and energy:

$$\frac{\partial \rho}{\partial t} + \nabla \cdot (\rho \boldsymbol{u}) = 0, \tag{1.3a}$$

$$\frac{\partial (\rho \boldsymbol{u})}{\partial t} + \nabla \cdot (\rho \boldsymbol{u}\boldsymbol{u} + \boldsymbol{P}) = \boldsymbol{F}, \tag{1.3b}$$

$$\frac{\partial (\rho E)}{\partial t} + \nabla \cdot (\rho E \boldsymbol{u} + \boldsymbol{P}\boldsymbol{u} + \boldsymbol{q}) = \boldsymbol{F} \cdot \boldsymbol{u}, \tag{1.3c}$$

where ρ is the density, t is time, and $\boldsymbol{u}$ is the bulk velocity. The stress tensor $\boldsymbol{P} = p\boldsymbol{I} + \boldsymbol{P}_d$ consists of the normal pressure p and the deviatoric term $\boldsymbol{P}_d$, while $\boldsymbol{I}$ is the unit tensor. $\boldsymbol{F}$ represents external forces, E is the total energy which includes both internal and kinetic contributions, and $\boldsymbol{q}$ denotes the heat flux vector. However, these equations are not closed,

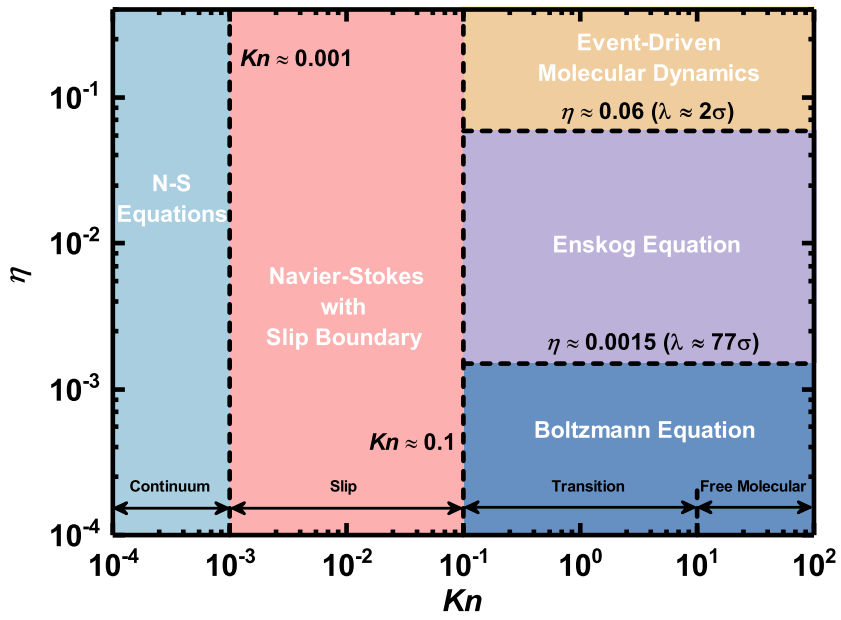

Figure 1.1: Regime diagram indicatively showing the most computationally efficient technique to model hard-sphere fluids for a given combination of Knudsen number and reduced number density. The flow field is assumed to be large enough for fluctuations to be negligible.

as the deviatoric term of stress tensor and heat flux vector remain unknown. Constitutive relations, such as Newton's law for viscosity:

$$\boldsymbol{P}_d = \mu \left[\nabla \boldsymbol{u} + (\nabla \boldsymbol{u})^T\right] + \mu_b (\nabla \cdot \boldsymbol{u}) \boldsymbol{I}, \tag{1.4}$$

and Fourier's law for heat conduction:

$$\boldsymbol{q} = -\kappa \nabla T, \tag{1.5}$$

are commonly used to determine these parameters, where μ and μ_b are the shear and bulk viscosities, respectively, related by the Stokes hypothesis ($\mu_b + \frac{2}{3}\mu = 0$) for monatomic gases, and κ is thermal conductivity. The Eqs. 1.3, 1.4, and 1.5 are known as the Navier-Stokes-Fourier equations. In confined flows with solid boundaries, the no-slip boundary condition is typically applied, assuming zero relative velocity between the fluid and the solid surface (Lauga, Michael, & Stone, 2005; Richardson, 1973). They provide a complete description of fluid behavior within the continuum regime.

However, no-slip boundaries are no longer valid when the Kn number increases ($Kn \gtrsim 0.001$), as molecular collisions become insufficient and the fluid shifts from a local equilibrium to a non-equilibrium state (Maxwell, 1878). For example, in confined gas flow with $Kn \gtrsim 0.001$, non-equilibrium effects emerge near solid surfaces, causing the gas to slip along the surface

and breaking the no-slip condition. In this regime, slip boundary conditions, which account for velocity or temperature gradients between the fluid and solid surfaces, are used with the Navier-Stokes equations. As the Kn number increases further, the gas flow enters the transition or free molecular regimes, where non-equilibrium effects spread into the bulk of the flow. In such cases, kinetic theory and molecular dynamics simulations must be used to make accurate predictions of flow behaviour.

1.1.2 Kinetic Theory for Dilute Gases

Kinetic theory plays a crucial role in capturing flow behaviour by explicitly accounting for molecular collisions, particularly at higher Knudsen numbers ($Kn \gtrsim 0.1$). For sufficiently low densities ($\eta < 0.0015$) (Bird, 1994), the gas can be treated as dilute, allowing the use of the Boltzmann equation, which was formulated in the 19th century to describe dilute monatomic gases. The Boltzmann equation provides a statistical representation of gas dynamics by governing the evolution of the molecular velocity distribution function $f(\boldsymbol{x},\boldsymbol{\xi},t)$, which describes the number of particles within an infinitesimal phase space element $d\boldsymbol{x}d\boldsymbol{\xi}$ around position $\boldsymbol{x}$ and molecular velocity $\boldsymbol{\xi}$ at time t (Boltzmann, 1872). Macroscopic properties such as density, bulk velocity, and temperature are obtained by integrating f over all molecular velocities, thereby linking microscopic dynamics to observable fluid behaviour. Transport coefficients, such as viscosity and thermal conductivity, are derived by expanding the velocity distribution function in a Taylor series. This expansion enables the constitutive relations to go beyond Newton's and Fourier's laws, effectively capturing rarefaction effects (Kremer, 2010). In addition to monatomic gases, the Boltzmann equation has been extended to model dilute polyatomic gases, which consist of molecules with internal degrees of freedom, such as rotational and vibrational modes. By incorporating energy distribution across these modes, the extended models can predict key thermodynamic and transport properties, including bulk viscosity and the contributions of translational and internal motions to thermal conductivity (Eucken, 1913; Tisza, 1942a).

However, the Boltzmann equation and its extensions rely on the dilute gas assumption, where collisions are treated as instantaneous and localized. As gas density increases, molecular finite size effects become significant, leading to higher collision frequencies and non-local momentum and energy transfer. This breakdown of the dilute gas assumption necessitates a different approach for modelling dense gases. The transition to dense gas behaviour is typically characterized by the reduced number density, with significant deviations occurring when $\eta > 0.0015$ (Bird, 1994). To address these effects, a kinetic model known as the Enskog equation is developed to provide a more accurate description of moderately dense gases, which will be introduced in the next section.

1.1.3 Kinetic Theory for Moderately Dense Gases

Enskog (1922) was the first to modify the Boltzmann equation to account for the moderately dense gases. The modified kinetic equation, named Enskog equation, governs the evolution of the velocity distribution function f, with a collision term that incorporates spatially separated colliding molecules and an increased collision frequency to account for the finite size effects of gas molecules. While the Enskog equation significantly improves the modelling of moderately dense gases, it has a key limitation: it assumes gas molecules are hard spheres and neglects the long-range intermolecular forces. As a result, it struggles to accurately predict thermodynamic and transport properties, particularly in real gases or those with strong intermolecular interactions. To improve the accuracy of Enskog equation, several modifications were introduced. For example, molecular softness was incorporated to account for changes in molecular diameter during collisions, and alternative molecular potential models were adopted to recover accurate transport coefficients (Chapman & Cowling, 1952; Hanley, McCarty, & Cohen, 1972). Additionally, since the original Enskog equation only considered repulsive intermolecular forces, a long-range attractive force was later included, which is particularly important for simulating two-phase flows (Sobrino, 1967). These modifications expanded the applicability of the Enskog equation.

As shown in Figure 1.1, the Enskog equation is an efficient approach but has an upper density limit of $\eta \approx 0.06$. At higher gas densities, individual molecular motion plays a crucial role in flow behaviour, making statistical kinetic models inadequate. For instance, in methane extraction from shale reservoirs, methane is primarily stored in nanopores, where frequent molecular interactions with pore surfaces give rise to significant effects such as surface adsorption and surface diffusion. These fluid-wall interaction effects, governed by the precise trajectories of individual molecules, cannot be fully captured by kinetic models like the Boltzmann and Enskog equations (Dąbrowski, 2001). In such cases, molecular dynamics simulations become essential for accurately predicting flow properties, as discussed in the following section.

1.1.4 Molecular Dynamics Simulations

Given the limitations of kinetic models in capturing explicit molecular-scale interactions for high-density gases, molecular dynamics (MD) simulations offer an alternative by directly resolving individual molecular behaviour. It provides the atomic-level detail necessary to capture molecular interactions by simulating the behaviour of individual atoms or molecules. By using appropriate intermolecular potentials, such as the Lennard-Jones potential, MD simulations track particle trajectories based on Newton's equations of motion (Alder & Wainwright, 1957). Macroscopic quantities, such as density and temperature, are derived through time averaging

of molecular velocities and positions, while transport coefficients can be computed using Green-Kubo relations, based on linear response theory (Green, 1954; Kubo, 1957). These characteristics make MD simulations particularly suitable for applications requiring molecular specificity and atomistic precision.

For systems composed of hard-sphere molecules interacting via the Lennard-Jones potential, event-driven molecular dynamics (EDMD) is often preferred over classical MD simulations (Alder & Wainwright, 1959). Unlike classical MD simulations, which require costly evaluations of multibody intermolecular forces at each time step, EDMD tracks only binary collisions, updating particle positions and velocities between successive collision events. This event-based approach significantly reduces computational cost while maintaining an exact representation of monatomic hard-sphere dynamics. Moreover, in contrast to Enskog theory, which provides an approximate treatment of moderately dense gas behaviour, EDMD offers an exact description of hard-sphere fluids across the entire range of reduced fluid densities (Pöschel & Schwager, 2005).

While these MD simulations are crucial for studying processes dominated by atomic-level interactions, they are computationally expensive and time-consuming, limiting their applicability to small systems and short timescales. For larger systems or longer-term processes, MD simulations are often supplemented by kinetic or continuum models, which connect atomic-level details with macroscopic phenomena. Additionally, in many engineering applications, the non-equilibrium effects and molecular interactions must be accounted for, while full molecular simulations may be impractical. In such cases, kinetic theory provides a valuable alternative, offering a balance between accuracy and computational efficiency. By statistically modelling molecular collisions and transport processes, kinetic theory extends the applicability of fluid modelling beyond the continuum assumption while significantly reducing computational expense compared to MD simulations. The next section will explore its diverse applications across different engineering domains.

1.2 Engineering Applications of Kinetic Theory

Recent advancements in micro- and nanotechnology require models that accurately capture nonequilibrium transport phenomena and molecular interactions. As discussed in Section 1.1, kinetic theory serves as an efficient tool to address engineering challenges where continuum approaches are physically inappropriate and MD simulations are computationally prohibitive. This section presents examples demonstrating how kinetic theory serves as a robust framework for problems ranging from micro- and nanoscale transport in devices such as MEMS and NEMS to macroscopic hypersonic aerodynamics.

In MEMS, where surface interactions and thermal effects dominate, kinetic theory is crucial for capturing behaviour that continuum models cannot. For instance, in MEMS resonators and sensors with channel dimensions on the order of hundreds of nanometers, surface forces and gas damping significantly affect performance (Gad-el Hak, 1999). Kinetic-based models accurately describe slip flow and rarefaction effects, which are essential for predicting energy losses and optimizing device efficiency. Similarly, in microchip thermal management, where heat dissipation is constrained, kinetic models account for non-equilibrium effects in heat transfer (Gavasane, Agrawal, Pradeep, & Bhandarkar, 2017), enabling better predictions of temperature distributions and improving device performance and reliability.

In the nanoscale liquid-vapour flows, kinetic theory provides essential insights that are beyond the reach of continuum approaches. While these approaches can effectively describe bulk heat and mass transfer, kinetic models reveal the flow properties at the liquid-vapour interface, which spans only a few molecular diameters and exhibits significant temperature and density gradients (Frezzotti, Gibelli, & Lorenzani, 2005b). This is particularly relevant for NEMS applications such as chip cooling and nanofluidics. As mentioned in Section 1.1.4, MD simulations are commonly used to study molecular behaviour at nanoscale (Perumanath, Borg, Chubynsky, Sprittles, & Reese, 2019). However, their high computational cost limits their feasibility for efficient modelling entire liquid-vapour systems.

Beyond the aforementioned applications, kinetic theory is widely employed in macroscopic hypersonic aerodynamics. In aerospace engineering, it plays a crucial role in scenarios where the Navier-Stokes equations fail to capture essential flow characteristics, such as high-altitude and high-speed flight in low-density, low-pressure environments. Kinetic theory provides a robust framework for understanding non-equilibrium gas dynamics, which is critical for predicting shock wave structures and heat transfer in rarefied flows (Alsmeyer, 1976; P. Wang, Wu, Ho, Li, & Zhang, 2020). Moreover, it aids in the design of hypersonic vehicles and spacecraft by optimizing re-entry dynamics, thermal protection systems, and surface interactions (Gan, Chen, & Zhang, 2023).

These diverse applications underscore the crucial role of kinetic theory in bridging the gap between continuum and MD descriptions, offering valuable insights for engineering innovations. However, despite its ability to capture non-equilibrium effects, the practical application of kinetic models remains largely confined to simple geometries and lower-dimensional systems due to the complexity of real-world gas environments. For instance, MEMS devices typically operate in air, requiring models for polyatomic gases, while liquid-vapour flows involve dense gases and interfacial regions with strong molecular interactions. As the number of degrees of freedom increases (e.g., from monatomic to polyatomic gases) or as molecular collisions become increasingly nonlocal (e.g., from dilute to dense gases), the computational

cost rises exponentially. This significantly limits the feasibility of kinetic simulations for complex structures and higher-dimensional systems. To overcome these challenges, simplified kinetic models are necessary. The next chapter will introduce the theoretical and computational background, covering both original and simplified kinetic models.

1.3 Thesis Outline

The reminding chapters are organized as following,

Chapter 2 - **Theoretical and Computational Background** provides an overview of kinetic models for rarefied monatomic gases, rarefied polyatomic gases, and dense monatomic gases. It begins with the Boltzmann equation as the foundation of kinetic theory for rarefied monatomic gases. Modifications incorporating internal energy are then introduced to extend the framework to rarefied polyatomic gases. The chapter further presents a kinetic model based on Enskog theory for dense monatomic gases. In each section, simplified kinetic models are derived to improve computational efficiency while maintaining accuracy. Finally, commonly used numerical methods, including particle and deterministic approaches, are reviewed.

Chapter 3 - **Simplified Kinetic Modelling of Polyatomic Gases** is the first chapter to present new findings. This study examines sound wave propagation in rarefied polyatomic gases using simplified Boltzmann collision term, focusing on energy transfer between translational and rotational modes across different rarefaction levels and oscillation frequencies. For thermoacoustic waves, the relationship between thermodynamic fluxes and driving forces is explored, demonstrating that pressure deviations induced by temperature variations are equivalent to heat fluxes generated by plate oscillations.

Chapter 4 - **Simplified Kinetic Modelling of One-Dimensional Liquid-Vapour Flows: Evaporation Dynamics** is the second chapter to present new findings. This study investigates liquid and vapour phases and their interface using a simplified Enskog collision term. Unlike traditional kinetic models that treat the liquid phase and interface as an boundary and rely on a Hertz-Knudsen-type evaporation model, the proposed model captures macroscopic variations during evaporation without requiring a phenomenological model. Comparisons with particle-based methods demonstrate that the simplified kinetic model significantly reduces computational cost while maintaining accuracy, achieving an average speedup of nearly two orders of magnitude for the cases studied.

Chapter 5 - **Simplified Kinetic Modelling of Two-Dimensional Liquid-Vapour Flows: Droplet Ripening** is the final chapter to present new findings. This study investigates droplet ripening in a two-dimensional system using an higher dimensional simplified kinetic model from Chapter 4. The results confirm that the ripening process is driven by the pressure difference, consistent with theoretical predictions. The relationship between droplet growth rate

and Laplace pressure is examined, revealing a linear trend when droplets retain a bulk region, while non-linear effects emerge as the bulk region vanishes. Furthermore, the slope of this linear relationship increases exponentially with temperature, regardless of droplet number and arrangement.

Chapter 6 - **Concluding Remarks** summarizes the key findings and explores potential future research directions that could build upon the work presented in this thesis.

Chapter 2

Theoretical and Computational Background

This chapter introduces standard kinetic models and the numerical methods used to solve them. At the foundation of these models is the Boltzmann equation, which describes the behaviour of monatomic rarefied gas flows (Section 2.1). However, practical applications often involve more complex gas conditions, such as polyatomic or dense gases. For polyatomic gases, the kinetic models extend the Boltzmann equation by incorporating internal energy transitions into the collision term (Section 2.2). Similarly, dense gas models are developed by modifying the Boltzmann equation's collision term to account for molecular volume effects (Section 2.3). It should be noted that while these modifications are necessary for physical accuracy, they significantly increase the mathematical complexity of the already complicated collision integral. To address this complexity, simplified kinetic models are derived and presented in each section. The chapter concludes with a brief overview of numerical methods for integration required in engineering applications (Section 2.4)

2.1 Basics of Kinetic Theory

2.1.1 Boltzmann Equation

The Boltzmann equation provides the fundamental statistical framework in kinetic theory for modelling rarefied monoatomic gas flows. This equation is derived under the following key assumptions (Kremer, 2010):

- The probability of collisions involving more than two molecules is significantly lower than that of binary encounters.
- The influence of external forces on molecules during the mean collision time is negligible compared to the forces arising from molecular interactions.
- The asymptotic pre-collisional velocities of two molecules are uncorrelated, as are their post-collisional velocities.
- The distribution function remains nearly constant over a time interval that is longer than the mean collision time but shorter than the mean free time.

The Boltzmann equation is expressed as

$$\frac{\partial f}{\partial t} + \boldsymbol{\xi} \cdot \frac{\partial f}{\partial \boldsymbol{x}} + \frac{\boldsymbol{F}}{m} \cdot \frac{\partial f}{\partial \boldsymbol{\xi}} = \Omega_B, \tag{2.1a}$$

$$\Omega_B = \int (f(\boldsymbol{x}, \boldsymbol{\xi}^{'}, t) f(\boldsymbol{x}, \boldsymbol{\xi}_1^{'}, t) - f(\boldsymbol{x}, \boldsymbol{\xi}, t) f(\boldsymbol{x}, \boldsymbol{\xi}_1, t)) \boldsymbol{g} \cdot \boldsymbol{k} \mathrm{d}\boldsymbol{k} \mathrm{d}\boldsymbol{\xi}_1, \tag{2.1b}$$

where m is the mass of molecule, $\boldsymbol{g} = \boldsymbol{\xi}_1 - \boldsymbol{\xi}$ is the relative velocity of two collision molecules, and $\boldsymbol{k}$ is the unit vector, which is related to the relative position of the collision molecules. $\boldsymbol{\xi}$ and $\boldsymbol{\xi}_1$ are post-collision molecular velocities while $\boldsymbol{\xi}^{'}$ and $\boldsymbol{\xi}_1^{'}$ are pre-collision molecular velocities. The spatial and velocity evolution of the distribution function in the Boltzmann equation is governed by two contributions: a free-stream contribution on the left-hand side, which describes the free motion of particles and their evolution under the influence of external forces, and a collision contribution on the right-hand side, which accounts for interactions between molecules. It has been established that the Boltzmann equation preserves important physical and mathematical properties. For instance, the mass, momentum, and energy balance laws can be derived directly from the Boltzmann equation using the Chapman-Enskog expansion (Chapman & Cowling, 1952). Furthermore, the Boltzmann equation satisfies the H-theorem, which asserts that the H-function, defined as

$$H = \int f \ln f \mathrm{d}\boldsymbol{\xi}, \tag{2.2}$$

monotonically decreases over time during the evolution of a gas, provided that the system is isolated. This monotonic decrease reflects the irreversible nature of macroscopic processes and is consistent with the second law of thermodynamics. At equilibrium, the H-function reaches its minimum value, corresponding to the state of maximum entropy. Under this condition, the distribution function becomes the Maxwellian equilibrium distribution function f^{eq}, given by

$$f^{eq} = n \left(\frac{m}{2\pi k_B T} \right)^{3/2} \exp\left(-\frac{mC^2}{2k_B T} \right), \tag{2.3}$$

where k_B is the Boltzmann constant and $\boldsymbol{C} = \boldsymbol{\xi} - \boldsymbol{u}$ is the peculiar velocity. At this state, the collision term in the Boltzmann equation vanishes, indicating that the system has achieved thermodynamic equilibrium.

2.1.2 Boltzmann-Like Simplified Kinetic Models

The Boltzmann equation is a nonlinear integro-differential equation. While its direct solution can yield reliable results, the computational cost is prohibitively high for practical applications. For specific flow regimes, simpler methods are often chosen to avoid the complexity of the Boltzmann framework. As discussed in Section 1.1, in the slip flow regime, non-equilibrium effects are primarily confined to the thin Knudsen layer near surfaces, while the bulk flow is adequately described by the Navier-Stokes equations. These non-equilibrium effects can be effectively captured using modified boundary conditions that incorporate velocity slip and temperature jump. In the transition flow regime, however, the thickness of the Knudsen layer becomes comparable to the characteristic scale of the flow field, rendering boundary condition corrections insufficient. In such cases, hydrodynamic equations are extended, such as the Burnett (Chapman & Cowling, 1952), super-Burnett (Shavaliyev, 1993), and moment equations (Torrilhon, 2016), which introduce additional field variables and higher-order derivatives to account for phenomena beyond the scope of conventional continuum theory.

However, for analyzing gas flows over a wide range of rarefaction, the Boltzmann framework remains the most robust and comprehensive choice. To enhance its computational efficiency, simplified kinetic models have been developed for the Boltzmann equation. One such widely used model is the Bhatnagar-Gross-Krook (BGK) model, where the collision term Ω_{BGK} is expressed as (Bhatnagar, Gross, & Krook, 1954):

$$\Omega_{BGK} = \frac{f^{eq} - f}{\tau}. \tag{2.4}$$

The relaxation time, τ, quantifies the effects of molecular collisions and governs the rate at which the gas approaches equilibrium. It can be determined using the Chapman-Enskog expansion, to be $\tau = \mu / p_0$, where μ is the gas viscosity and p_0 is the gas pressure. Despite its simplicity, this model captures key hydrodynamic properties, such as mass, momentum, and energy conservation, as well as the tendency of the distribution function to approach equilibrium, which is described by the H-theorem. However, the BGK model has a limitation: it does not provide the correct ratio for the transport coefficients. The Prandtl number (Pr), which is the ratio of thermal conductivity to viscosity, is equal to 1 in the BGK model, rather than the correct value of 2/3 for monatomic gas. This inherent limitation hinders its ability to simultaneously represent the correct values of viscosity and thermal conductivity in rarefied gas flows.

To address this issue, the Shakhov model (Shakhov, 1968) was developed as an extension of the BGK model to match the correct the value of the Pr while maintaining simplicity. Specifically, the Maxwellian distribution function in the BGK collision term is modified by multiplying a term proportional to heat flux. As a result, the collision term Ω_S is expressed

as

$$\Omega_S = \frac{f^S - f}{\tau}, \tag{2.5a}$$

$$f^S = f^{eq}\left[1 + \frac{2m(1-Pr)\boldsymbol{q}\cdot\boldsymbol{C}}{5n(k_BT)^2}\left(\frac{m\boldsymbol{C}^2}{2k_BT} - \frac{5}{2}\right)\right]. \tag{2.5b}$$

At equilibrium, the Shakhov model accurately predicts both viscosity and thermal conductivity, ensuring consistency with physical transport properties. However, it does not satisfy the H-theorem, as the additional term introduced to correct the Prandtl number disrupts the strict monotonic decrease of the entropy production rate, which is a fundamental requirement of the theorem. In addition to the Shakhov model, a similar extension of the Boltzmann equation, known as the Ellipsoidal Statistical (ES) model (Holway, 1966), was developed. In the ES model, the Maxwellian distribution function is replaced by an anisotropic Gaussian distribution that is related to the stress tensor. The ES model is capable of reproducing the correct Prandtl number and also satisfies the H-theorem. Numerous studies have shown that these two models yield similar results in the continuum regime (Meng, Wu, Reese, & Zhang, 2013; Mieussens & Struchtrup, 2004). However, in the transition regime, the Shakhov model provides more accurate predictions for gas flows. On the other hand, for flows dominated by temperature gradients, the ES model performs better due to its strict adherence to the H-theorem and the guarantee of a non-negative distribution function (S. Chen, Xu, & Cai, 2015; Fei, Liu, Liu, & Zhang, 2020).

2.2 Kinetic Theory Description of Rarefied Polyatomic Gases

While the Boltzmann equation and its simplified models effectively simulate monatomic gases, the behaviour of polyatomic gases introduces additional complexity due to their internal energy modes. The monatomic gas, such as noble gases (e.g., argon and neon), consists of a single atom which has only translational degrees of freedom, where the atom can move in a three-dimensional space. In contrast, polyatomic gases, such as oxygen, nitrogen, and carbon dioxide, are composed of molecules with multiple atoms. In addition to translational motion, these atoms can rotate about their axes, contributing rotational energy to the internal energy. Furthermore, they may oscillate about their equilibrium positions, contributing vibrational energy to the internal energy. In principle, the activation of each mode depends on the thermal energy of the gas, which is characterized by its temperature. Translational and rotational modes are typically active at room temperature, while vibrational modes require significantly higher temperatures to become energetically accessible, as their activation thresholds correspond to the energy levels associated with bond stretching or bending. For instance, the translational and rotational modes of nitrogen are actives at room temperature, whereas its

vibrational mode becomes active at approximately $T \approx 3370K$ (Tantos, Ghiroldi, Valougeorgis, & Frezzotti, 2016). These internal energy modes significantly influence macroscopic flow properties, necessitating the development of extended kinetic models specifically tailored for polyatomic gases.

2.2.1 Wang-Chang-Uhlenbeck Model

The first relatively successful kinetic model for polyatomic gases was developed by Wang-Chang and Uhlenbeck, incorporating a semi-quantum mechanical framework (Wang-Chang & Uhlenbeck, 1951). In this model, the internal molecular motion is represented by discrete internal energy states. The distribution function f_α in this framework depends on time, molecular velocity, position, and internal energy state α_i, where i is the quantum numbers of internal energy state. Thus, the Wang-Chang-Uhlenbeck equation is expressed as (Kremer, 2010; Wu, 2022)

$$\frac{\partial f_\alpha}{\partial t} + \boldsymbol{\xi} \cdot \frac{\partial f_\alpha}{\partial \boldsymbol{x}} + \frac{\boldsymbol{F}}{m} \cdot \frac{\partial f_\alpha}{\partial \boldsymbol{\xi}} = \Omega_{WCU}, \tag{2.6a}$$

$$\Omega_{WCU} = \sum_{\alpha_1, \alpha', \alpha_1'} \int P^{\alpha\alpha_1}_{\alpha'\alpha_1'} (f_{\alpha'} f_{\alpha_1'} - f_\alpha f_{\alpha_1}) \boldsymbol{g} \cdot \boldsymbol{k} \mathrm{d}\boldsymbol{k} \mathrm{d}\boldsymbol{\xi}_1, \tag{2.6b}$$

where the $P^{\alpha\alpha_1}_{\alpha'\alpha_1'}$ denotes the probability of the transfer from internal energy states $\alpha^{'}$ and $\alpha_1^{'}$ to the states α and α_1. As reflected in the collision term, internal energy exchange is captured through transitions between energy states resulting from both elastic and inelastic collisions. Similarity, macroscopic quantities, such as number density, bulk velocity, and temperature, are obtained by integrating the distribution function over all molecular velocities and internal energy states. While it provides a kinetic theory description of polyatomic gases, the analytical and numerical implementation of the Wang-Chang-Uhlenbeck model remains highly challenging and computationally expensive. Studies on hypersonic flow have shown that its computational cost is approximately two orders of magnitude higher than that for monatomic gases (Tcheremissine & Agarwal, 2008).

2.2.2 Hanson-Morse Model

To improve the computational efficiency of Wang-Chang-Uhlenbeck model, Hanson and Morse (1967) developed a linearized kinetic model, similar to the construction of linearized Boltzmann equation (Gross & Jackson, 1959). This model is suited for gas flows near equilibrium, where pressure and temperature gradients are small. Following the assumption of small deviation, the distribution function can be approximated by

$$f_\alpha = f_\alpha^0 (1 + \phi_\alpha(\boldsymbol{x}, \boldsymbol{\xi}, t, \alpha)), \tag{2.7}$$

where f_α^0 is the Maxwellian distribution function for polyatomic gas and $\phi_\alpha \ll 1$ represents the small perturbation, capturing the deviation of the system from equilibrium. By placing the Eq. 2.7 into the Eq. 2.6a and Eq. 2.6b, the original Wang-Chang-Uhlenbeck model can be linearized as

$$\frac{\partial \phi_\alpha}{\partial t} + \boldsymbol{\xi} \cdot \frac{\partial \phi_\alpha}{\partial \boldsymbol{x}} = \Omega_{WCUlinear}, \tag{2.8}$$

by neglecting external forces and higher-order terms of ϕ_a. Then, in the linearized collision term $\Omega_{WCUlinear}$, ϕ_a is expanded as a series of orthogonal velocity polynomials with space- and time-dependent coefficients, which can be determined through empirical models (Boley, Desai, & Tenti, 1972; Pan, Shneider, & Miles, 2004; Tenti, Boley, & Desai, 1974). These treatments significantly enhance the computational efficiency of the kinetic model, making it more suitable for practical numerical simulations. Notably, the linearized kinetic model preserves the same relaxation rates as the original Wang-Chang-Uhlenbeck equation, ensuring consistency with the underlying physical behaviour.

2.2.3 Rykov Model

Since the Hanson-Morse model is limited to near-equilibrium gas flows, Rykov (1975) developed a practical model to address nonlinear flow scenarios for non-vibrating polyatomic gases. Similar to the Wang-Chang-Uhlenbeck model, the distribution function f_R in the Rykov model depends not only on time, molecular velocity, and position but also on rotational energy. The collision term is modified into BGK form, consisting of two components: an elastic term that conserves both translational and rotational energies, and an inelastic term that accounts for energy exchange between translational and rotational modes. In the absence of external forces, the governing equation is given by:

$$\frac{\partial f_R}{\partial t} + \boldsymbol{\xi} \cdot \frac{\partial f_R}{\partial \boldsymbol{x}} = \frac{f_R^t - f_R}{\tau_t} + \frac{f_R^r - f_R}{\tau_r}, \tag{2.9}$$

where the index t refers to the translational contribution and r refers to the rotational contribution. In order to improve the numerical efficiency, Rykov further introduced two distribution functions to eliminate the rotational energy

$$f_0 = \int f_R \mathrm{d}E_r, \quad f_1 = \int E_r f_R \mathrm{d}E_r, \tag{2.10}$$

where E_r denotes the rotational energy. Thus, the original governing equation can be written as

$$\frac{\partial f_0}{\partial t} + \boldsymbol{\xi} \cdot \frac{\partial f_0}{\partial \boldsymbol{x}} = \frac{f_0^t - f_0}{\tau_t} + \frac{f_0^r - f_0}{\tau_r}, \tag{2.11a}$$

$$\frac{\partial f_1}{\partial t} + \boldsymbol{\xi} \cdot \frac{\partial f_1}{\partial \boldsymbol{x}} = \frac{f_1^t - f_1}{\tau_t} + \frac{f_1^r - f_1}{\tau_r}. \tag{2.11b}$$

Here, f_0^t, f_1^t, f_0^r and f_1^r are local Maxwellian distribution functions corresponding to the translational and rotational motions. The relaxation terms have a form similar to those in the BGK model

$$\tau_t = \frac{\mu_t}{p_t}\frac{Z}{Z-1}, \quad \tau_r = \frac{\mu_t}{p_t}Z, \tag{2.12}$$

where Z is dimensionless rotational collision number which is a function only of translational and rotational contributions of temperature. The Rykov model is widely employed for simulating polyatomic gas flows, such as normal shock wave phenomena (Larina & Rykov, 2010; Liu, Yu, Xu, & Zhong, 2014). While the model successfully predicts the density profile, it fails to provide an accurate temperature profile due to the use of a single relaxation time τ that is independent of molecular velocity. To address this limitation, Wu, White, Scanlon, Reese, and Zhang (2015) introduced a molecular velocity-dependent relaxation time and replaced the elastic collision operator in the Rykov model with the Boltzmann collision operator for monatomic gases. The modified model can accurately predict both the density and temperature profiles for normal shock waves.

2.3 Kinetic Theory Description of Liquid-Vapour Flows

Liquid-vapour flows play a critical role in various engineering applications, including cooling systems for electronics and water desalination membranes. To accurately model fluid flows involving phase transitions, two key extensions to the Boltzmann equation are required: the incorporation of dense gas effects to account for high-density regions and the inclusion of a self-consistent force field to represent molecular attraction. The following sections will introduce the approaches developed to address these two aspects.

2.3.1 Enskog Equation

Dense gas effects are particularly relevant in liquid-vapour flows, where the density of the liquid phase and the interfacial region is high. In these scenarios, the Boltzmann equation is insufficient. Instead, Enskog equation, which accounts for dense gas effects by incorporating finite molecular size and collision dynamics, must be employed (Enskog, 1922). The Enskog equation describes the dynamics of dense fluids composed of rigid, elastic, and spherical molecules. Two key assumptions are made that differ from the Boltzmann equation approach: (Chapman & Cowling, 1952):

- The positions of colliding molecules are not at the same point, making the model suitable for moderately dense gases.
- The finite volume of molecules reduces the available free space for molecular motion, thereby increasing the collision frequency.

These assumptions lead to a modified collision term, providing a more accurate description of dense gas dynamics:

$$\Omega_E = \sigma^2 \int \left\{ \chi\left(\boldsymbol{x}+\frac{\sigma}{2}\boldsymbol{k}\right) f^{'}(\boldsymbol{x}) f_1^{'}(\boldsymbol{x}+\sigma\boldsymbol{k}) - \chi\left(\boldsymbol{x}-\frac{\sigma}{2}\boldsymbol{k}\right) f(\boldsymbol{x}) f_1(\boldsymbol{x}-\sigma\boldsymbol{k}) \right\} \boldsymbol{g}\cdot\boldsymbol{k} d\boldsymbol{k} d\boldsymbol{\xi}_1. \tag{2.13}$$

Here, the distribution functions are evaluated at different positions $\boldsymbol{x}$ and $\boldsymbol{x}+\sigma\boldsymbol{k}$ during the collision, capturing the finite volume effect of molecules. Additionally, the χ, named the pair correlation function, is used to quantify the enhanced collision frequency. The expression of χ is derived from the equation of state (EoS) of gas and is dependent on the local density. One common used form of χ comes from the Carnahan-Starling EoS (Carnahan & Starling, 1969)

$$\chi(\rho) = \frac{1-0.125b\rho}{(1-0.25b\rho)^3}, \tag{2.14}$$

where $b = 2\pi\sigma^3/3m$.

2.3.2 Enskog-Like Simplified Kinetic Models

Incorporating dense-gas effects makes the Enskog collision term, Ω_E, even more complex than the Boltzmann equation collision term. Consequently, simplifying the collision term is essential for computational efficiency. A classical approach is to expand the velocity distribution function and pair correlation function of Ω_E into a Taylor series at position x, retaining only the zeroth- and first-order terms (Chapman & Cowling, 1952), and evaluate the pair correlation function as well as the distribution functions at the same position $\boldsymbol{x}$. The distribution functions in the first order terms are then replaced by their local Maxwellian equilibrium. This substitution is justified because the first-order terms express the dense fluid effects, which become pronounced at high densities. As fluid density increases, the Knudsen number decreases, indicating that the system remains close to equilibrium (B. Shan, Su, Gibelli, & Zhang, 2023). The non-equilibrium effects at low densities are instead accounted for by the zeroth-order term, where the Knudsen number is small. Thus, the simplified Enskog collision term is expressed as

$$\Omega_E \approx \chi\Omega^{(0)} + \Omega^{(1)}, \tag{2.15a}$$

$$\Omega^{(0)} = \Omega_B, \tag{2.15b}$$

$$\Omega^{(1)} = -b\rho\chi f^{eq}\{\boldsymbol{C}\cdot[\nabla\ln(\rho^2\chi T) + \frac{3}{5}(\zeta^2-\frac{5}{2})\nabla\ln T] + \frac{2}{5}[2\boldsymbol{\zeta}\boldsymbol{\zeta}:\nabla\boldsymbol{u} + (\zeta^2-\frac{5}{2})\nabla\cdot\boldsymbol{u}]\}, \tag{2.15c}$$

where we define $\boldsymbol{\zeta} = \boldsymbol{C}/\sqrt{2RT}$. This simplified Enskog collision term is frequently employed in the development of kinetic models for dense fluids (Luo, 1998; P. Wang et al., 2020).

In the aforementioned simplification, the zeroth-order term, $\Omega^{(0)}$, corresponds to the Boltzmann collision term for dilute gases, while the first-order term, $\Omega^{(1)}$, captures dense gas effects. Consequently, this model maintains a computational cost comparable to the original Boltzmann equation. Similar with the treatments on the Boltzmann collision term, the zeroth-order term can be further simplified using BGK-type models. For instance, Luo (1998, 2000) developed a lattice Boltzmann model for isothermal dense fluid flows by replacing the zeroth-order term with the BGK collision term and simplifying the first-order term to retain only components contributing to mass and momentum conservation. For isothermal flows, the first-order term $\Omega_{iso}^{(1)}$ simplifies to:

$$\Omega_{iso}^{(1)} = -b\rho\chi f^{eq}\boldsymbol{C}\cdot\nabla\ln(\rho^2\chi). \tag{2.16}$$

This model has proven to be effective for studying dense gas flows in various channel geometries using numerical schemes based on quadrature in the velocity space (Busuioc, 2023, 2024; Busuioc & Sofonea, 2024). However, its application is limited to low-speed and near-equilibrium flows due to the restricted number of discrete velocities (Guo & Shu, 2013).

Instead of replacing the Boltzmann collision term with the BGK collision term, P. Wang et al. (2020) proposed the Shakhov-Enskog model, in which the zeroth-order term is approximated by the Shakhov collision term, while the first-order terms are retained. This model has better performance on the simulation of thermal properties on dense fluid. For instance, it effectively captures the number density, temperature, and velocity profiles during shock wave propagation while maintaining computational efficiency. Furthermore, the discrete velocity method used in the Shakhov-Enskog model allows for flexible adjustment of the number of velocity discretization points, enabling its application to non-equilibrium flows (S. Li et al., 2024).

2.3.3 Modelling of Long-Range Molecular Interaction Forces

For liquid-vapour flows, accurately modelling intermolecular forces is as critical as accounting for dense gas effects. However, the original Enskog theory is limited to hard-sphere fluids and neglects long-range molecular attractions. To overcome this limitation, the Modified Enskog Theory (MET) was developed by incorporating molecular attractions through the pair correlation function χ, which is derived from the EoS for real fluids. Although MET has been used to estimate transport coefficients in real fluids, its ability to reliably predict dynamic behaviour remains uncertain (B. Shan et al., 2023). Moreover, MET can produce unphysical negative transport coefficients when the fluid compressibility factor drops below unity (Kavokine, Netz, & Bocquet, 2021). In contrast to MET, which modifies χ, an alternative approach focuses on the force term in the left-hand side of the Enskog equation, known as the mean-field approximation (Sobrino, 1967). It introduces long-range molecular attractions by adding a weak attractive tail as an additional force term, resulting in the Enskog-Vlasov (EV) equation. EV-type models have been successfully applied to study liquid-vapour flows, providing a

kinetic framework for applications such as phase change and phase separation (S. Li et al., 2024; Y. Zhang, Xu, Qiu, Wei, & Wei, 2020). However, the EV frameworks are unable to accurately reproduce the flow properties of Lennard-Jones fluids, indicating the need for further investigation (Benilov & Benilov, 2019a).

2.4 Numerical Methods for Kinetic Equations

Several kinetic models have been presented in previous sections. The analytical complexity of these models makes closed-form solutions impossible for problems of engineering interest, while numerical solutions are challenging due to the following factors:

- Unlike the Navier-Stokes equations, which evaluate gas flow in three spatial dimensions, kinetic models also incorporate a three-dimensional velocity space, significantly increasing computational cost.
- Accurate gas flow simulations are computationally demanding due to the inherent complexity of the collision integral in the kinetic models, even when various simplifications are applied.

Therefore, beyond simplifying the collision term, it is also essential to develop efficient computational approaches to solve these models. Broadly, these techniques can be classified into particle methods, which simulate the molecule behaviour, and deterministic methods, which solve the governing equations through numerical discretization.

2.4.1 Particle Methods

The Direct Simulation Monte Carlo (DSMC) method, developed by Bird (1994), is the most widely used particle method for solving kinetic equations. As a statistical method, DSMC approach approximates the distribution function using computational particles, with each particle representing a group of real molecules. A key approximation in DSMC is the decoupling of molecular motion from intermolecular collisions over small time steps. Particle motion is treated deterministically, while collisions are modelled statistically using probabilistic rules. In the implementation of DSMC, time is discretized into steps smaller than the mean collision time to ensure accurate resolution of molecular motion and collision processes. The spatial domain is divided into cells smaller than the mean free path to group particles for calculating local macroscopic properties and identifying potential collision pairs. Particle velocities are sampled continuously from appropriate probability distributions, ensuring accurate representation of molecular velocity distributions. These treatments allow DSMC to capture the essential physics of gas flows with computational efficiency. Although DSMC is primarily designed to solve the original Boltzmann equation, it can be adopted to solve simplified

models, such as the BGK model, with appropriate modifications (Gallis & Torczynski, 2000; J. Li, 2011; Macrossan, 2001). These modified particle schemes preserve the core algorithmic structure of DSMC while offering advantages in terms of simplicity, numerical stability, and the ability to handle complex configurations.

The standard DSMC method and its variants have been developed for dilute gases, where the mean free path is significantly larger than the molecular diameter. When it comes to the dense gas problems, such as liquid-vapour flows, these methods are invalid. To overcome this limitation, the Consistent Boltzmann Algorithm (CBA) was introduced as an extension of the DSMC method. The CBA modifies the positions of colliding atoms and increases the collision rate, enabling its application to both dilute and dense fluids (Alexander, Garcia, & Alder, 1997). Despite these advancements, the CBA prediction of the transport coefficient becomes significantly less accurate as density increases. Particle schemes have also been designed for the Enskog equation (Frezzotti, 1997; Frezzotti, Barbante, & Gibelli, 2019; Montanero & Santos, 1996). In this approach, the DSMC collision procedure is modified for dense gases by incorporating the influence of neighboring cells. A global collision queue is constructed for the entire domain, capturing non-local collision effects and accounting for the finite molecular volume, unlike the standard DSMC method, which treats each computational cell independently. This scheme has been shown to be effective in predicting flow properties for single-phase dense gas flows (Frezzotti, 1997). Furthermore, by incorporating a Vlasov term, this particle method has been extended to simulate liquid-vapour systems (Barbante et al., 2015; Frezzotti et al., 2005a).

2.4.2 Deterministic Methods

Deterministic methods provide a numerical alternative to particle approaches for solving the Boltzmann equation. Unlike particle methods, which rely on stochastic techniques to model particle motion and collisions, deterministic methods discretize all variables explicitly, including time, space, and velocity, and solve the Boltzmann equation directly. Among these methods, the Discrete Velocity Method (DVM) stands out as one of the earliest approaches. First introduced by Goldstein, Sturtevant, and Broadwell (1989), DVM approximates the continuous velocity space by dividing it into a finite set of discrete velocity points, constructing a fixed grid in which each point represents a possible molecular velocity. The distribution function is then approximated at these discrete velocity points, allowing for a numerical representation of the molecular behaviour. In DVM, the time and space domains are discretized as well. Typically, time is discretized using an explicit Euler scheme, and the spatial domain is discretized using second-order finite differences. However, this method is computationally inefficient because post-collision velocities are restricted to predefined velocity nodes, limiting the accuracy of the representation of molecular collisions. Furthermore, the method becomes increasingly

resource-intensive as the velocity grid resolution increases, leading to higher computational costs. Despite these challenges, DVM remains a valuable tool due to its ability to provide a detailed and accurate description of the kinetic behaviour of gases (S. Li, Su, & Zhang, 2023; J. Y. Yang & Huang, 1995; Q. Zhang, Zhuo, Mu, Zhong, & Liu, 2023).

The Fast Spectral Method (FSM) is another widely used deterministic approach that offers higher accuracy and lower computational cost compared to DVM. In FSM, the distribution functions are expressed using spectral expansions, transforming the collision term into interactions between these spectral components. The nonlinear term, which involves products of two distribution functions, is efficiently handled in the spectral space as a convolution-like operation, significantly reducing the computational cost compared to directly evaluating velocity-space integrals in real space (Mouhot & Pareschi, 2006; Wu, White, Scanlon, Reese, & Zhang, 2013). FSM has been proven effective in simulating normal shock waves, planar Fourier flows, Couette flows, and force-driven Poiseuille flows. Additionally, it has been successfully extended to the Enskog equation, allowing for the simulation of non-equilibrium flows in tightly confined dense fluids (Wu, Liu, Reese, & Zhang, 2016; Wu, Zhang, & Reese, 2015). However, these simulations primarily involve relatively simple geometries and single-phase flow. When applied to more complex geometries or two-phase flow problems, FSM may face challenges.

As noted above for particle schemes, the deterministic methods allow the numerical solution of the Boltzmann and Enskog equations, but remain computationally expensive for practical applications due to the complexity of the original collision terms. To overcome this challenge, these methods have been extended to simplified models, such as the BGK and Shakhov models. For instance, Mieussens (2000) introduced new discrete-velocity models for the Boltzmann-BGK and BGK-ES equations, while P. Wang et al. (2020) applied the DVM to solve the Shakhov-Enskog equation. These studies demonstrate that deterministic simplified kinetic models can accurately capture both rarefied gases and dense gases, offering a balance between computational efficiency and physical accuracy. Expanding on these developments, the following chapters will introduce deterministic simplified kinetic models and explore their applications in capturing complex gas dynamics with improved computational efficiency.

Chapter 3

Simplified Kinetic Modelling of Polyatomic Gases

N.B. This chapter has been published in : Li, S., Su, W., Zhang, Y. "Sound wave propagation in rarefied molecular gases." *Journal of Fluid Mechanics* 973 (2023): A35.

Sound wave propagation in rarefied flows of molecular gases confined in micro-channels is investigated numerically. We first validate the employed kinetic model against the experimental results and then systematically study the gas damping and surface force on the transducer as well as the resonance/anti-resonance in confined space. To quantify the impact of the finite relaxation rates of the translational and internal energies on wave propagation, we examine the roles of bulk viscosity and thermal conductivity in depth over a wide range of rarefactions and oscillation frequencies. It is found that the bulk viscosity only exerts influence on the pressure amplitude and its resonance frequency in the slip regime in high oscillations. In addition, the internal degree of freedom is frozen when the bulk viscosity of a molecular gas is large, resulting in the pressure amplitude of sound waves in the molecular gas being the same as in a monatomic gas. Meanwhile, the thermal conductivity has a limited influence on the pressure amplitude in all the simulated flows. In the case of the thermoacoustic wave, we prove that the Onsager-Casimir reciprocal relation also holds for molecular gases, i.e. the pressure deviation induced by the temperature variation is equal to the heat flux induced by the plate oscillation. Our findings enable an enhanced understanding of sound wave propagation in molecular gases, which may facilitate the design of nano- /micro-scale devices.

3.1 Literature Survey

Sound wave propagation at nano- /micro-scales plays a key role in a variety of applications, e.g., vibrating micromechanical resonators in on-chip communication devices (Clark, Hsu, Abdelmoneum, & Nguyen, 2005), acoustic transducers in micro-electro-mechanical-systems (MEMS) sensors such as gyroscopes and accelerometers, and porous acoustic absorbers for sound reduction (M. Yang & Sheng, 2017). Since the geometric size shrinks to nano- /micro-meters and the surface-to-volume ratio dramatically increases, gas rarefaction and surface

effects such as gas damping are significantly enhanced, which largely determine the devices' performance (Chigullapalli, Weaver, & Alexeenko, 2012). For instance, the Brownian noise level in a MEMS accelerometer is dominated by the gas damping in its capacitive transducers (Boom, Bertolini, Hennes, & van den Brand, 2021); the efficiency of sound absorption in an acoustic absorber is low when gas damping is weak. Therefore, gaining a better understanding of rarefied gas damping and gas-surface interaction in vibrating MEMS and porous structures is of great importance for the design and operation of these nano- /micro-devices. Moreover, as gases are contained in a confined space, resonance and anti-resonance can induce local extreme pressure amplitudes, which is another important issue to be considered carefully (Struchtrup, 2012).

In addition to miniaturisation in size, the high frequency of a sound wave will also generate rarefaction effects. Therefore, two Knudsen numbers are often introduced to quantify the degree of rarefaction, i.e. the length-based Knudsen number (Kn_l), defined as the ratio of the mean free path of gas molecules to the characteristic flow length, and the time-based Knudsen number (Kn_t), the ratio between the molecular mean free time and the process time scale. The traditional Navier-Stokes equations are adequate to describe gas flows only when both Knudsen numbers are small, say, $Kn_{l/t} < 0.001$; otherwise, similar to the flow conditions often found in nano- /micro-devices (Frangi, Frezzotti, & Lorenzani, 2007; Park, Bahukudumbi, & Beskok, 2004; P. Wang, Zhu, Su, Wu, & Zhang, 2018), gas kinetic theory needs to be adopted to predict flow properties (Kalempa & Sharipov, 2009; Sharipov & Kalempa, 2008).

The kinetic theory has been exploited to investigate sound wave propagation in rarefied gases confined in nano- /micro-channels. Through the solution of the Boltzmann equation or its simplified kinetic model equations, gas damping properties including the spatial variations of pressure amplitude, temperature and heat flux have been reported under different oscillation frequencies and amplitudes (Garcia & Siewert, 2005; R. J. Wang & Xu, 2012). Resonance induced by the superposition of waves has also been investigated (Desvillettes & Lorenzani, 2012; Wu, Reese, & Zhang, 2014). In the high-frequency limit where molecular collisions during the characteristic flow time scale can be ignored, analytical solutions of the resonance and anti-resonance frequencies have been obtained for one-dimensional and two-dimensional channel flows. Most of the aforementioned studies focused on monatomic gases (Bisi & Lorenzani, 2016); however, the most common working gas is air, mainly composed of nitrogen and oxygen. Modelling sound wave propagation in molecular (diatomic and polyatomic) gases is more difficult since the kinetic equation describing the dynamics of rarefied flows of molecular gases is much more complex than the Boltzmann equation.

Compared with monatomic gases, the molecules of a molecular gas possess internal degrees of freedom due to the excitation of rotational and vibrational modes. The finite rates of the relaxation processes associated with translational and internal modes lead to more complex non-equilibrium phenomena. For instance, a new transport coefficient, i.e. the bulk viscosity,

emerges (Mandelshtam & Leontovich, 1937; Tisza, 1942b); meanwhile, the thermal conductivity contains not only the translational contribution but also internal components (Eucken, 1913). Previous studies showed that the bulk viscosity is determined by the relaxation rate between the translational and internal energies, and the translational and internal thermal conductivities are respectively determined by the relaxation rates of the translational and internal heat fluxes. These additional transport mechanisms, however, can significantly affect the flow properties of rarefied molecular gases such as the shock-wave structure (Kosuge & Aoki, 2018), the line shape of the Rayleigh-Brillouin scattering (Wu, Li, Liu, & Ubachs, 2020) and the flow velocity of the thermal transpiration in micro-channels (Q. Li, Zeng, Su, & Wu, 2021; Su, Zhang, & Wu, 2021). Some studies have been done to assess the properties of sound wave propagation in molecular gases with single or multiple components, where the influence of the energy exchange between different modes on the attenuation and phase velocity was addressed (Arima, Ruggeri, & Sugiyama, 2017; Dain & Lueptow, 2001a, 2001b; Ejakov, Phillips, Dain, Lueptow, & Visser, 2003; Kremer, Kunova, Kustova, & Oblapenko, 2018; Kustova, Mekhonoshina, Bechina, Lagutin, & Voroshilova, 2023; Rahimi & Struchtrup, 2014). These investigations were mainly based on continuum equations, including the Euler, Navier–Stokes, Grad's moment and rational extended thermodynamic equations. The non-equilibrium dynamics of the relaxation of internal energies were modelled by additional relaxation equations according to the multi-temperature method or state-specific description. The acoustic behaviour of the attenuation coefficient with respect to the energy relaxation rate, gas species and sound frequency was obtained and compared with experimental measurements. The acoustic properties of the wave propagation were considered in homogeneous flows, so gas damping due to the gas-surface interaction and resonance in confined space are not included. Note that if the Euler/Navier-Stokes or moment equations are applied, it is implied that the flow characteristic time scale is much larger than the mean free time of gas molecules (or translation relaxation time); that is, Kn_t should be small enough (Rahimi & Struchtrup, 2014). Therefore, continuum models are not well-suited for investigating high-frequency oscillation problems.

To the best of the authors' knowledge, a systematic study has yet to be conducted that focuses on the effects of bulk viscosity (i.e. finite relaxation rate of translational and internal energies) and thermal conductivity (i.e. finite relaxation rate of translational and internal heat fluxes) on sound wave propagation in confined channels, particularly under a wide range of Knudsen numbers and sound frequencies. In this work, we fill this knowledge gap and reveal some unique propagation properties in rarefied molecular gases. In addition to sound wave propagation, propagation of thermoacoustic waves induced by periodic variation of temperature is also important to many engineering applications, e.g. Pirani gauges, used to measure pressure in vacuum systems (Kalempa & Sharipov, 2014). The Onsager-Casimir reciprocal relation (OCRR), an important principle that links thermodynamics fluxes driven by different forces (Casimir, 1945; Onsager, 1931a, 1931b), becomes a powerful tool to validate

simulation and measurement results and to reduce the computational cost and the number of required experimental measurements. Previously, a general approach has been proposed to demonstrate OCRR for the rarefied flow of monatomic gases (Kalempa & Sharipov, 2012; Sharipov, 2006). In this work, we will examine whether OCRR holds for molecular gases.

The remainder of this chapter is organised as follows: the kinetic model and boundary conditions are described in Section 3.2.1; the formulation of wave propagation is presented in Section 3.2.2; in Section 3.3, we first validate the model against the experimental data and then investigate the influence of the unique transport coefficients of molecular gases on gas damping, surface force and resonance. Before concluding the work in Section 3.4, we numerically prove that the OCRR also holds for sound and thermal-acoustic wave propagation in molecular gases.

3.2 Methodology

3.2.1 Kinetic Model

The Boltzmann equation was extended for molecular gases by Wang-Chang and Uhlenbeck (1951) considering quantum mechanics where each internal energy level is assigned with an individual velocity distribution function; this yields a complicated operator for particle collisions that is prohibitively expensive for numerical simulations. Several simplified models using the relaxation-time approach have been developed (Gorji & Jenny, 2013; Holway, 1966; Morse, 1964; Rykov, 1975; Z. Wang, Yan, Li, & Xu, 2017; Wu, White, et al., 2015).

Generally, rarefied gas damping and resonance problems can be investigated by seeking solutions of kinetic equations via the direct simulation Monte Carlo (DSMC) (Emerson, Gu, Stefanov, Sun, & Barber, 2007; Hadjiconstantinou, 2002) method or the discrete velocity method (DVM) (Kalempa & Sharipov, 2009; Wu et al., 2014). The DSMC method uses a collection of particles to mimic the behaviour of gas molecules: particles move through the spatial space in a realistic manner, while intermolecular collisions and gas interactions are calculated stochastically according to some collision models and pair-selection schemes (Bird, 1994; Ivanov & Rogasinskii, 1991; Roohi, Stefanov, Shoja-Sani, & Ejraei, 2018). It was rigorously proved that DSMC and the Boltzmann equation are equivalent for monatomic gases in the dilute limit (W. Wagner, 1992). For rarefied molecular gases, the Borgnakke and Larsen (1975) phenomenological collision model was developed to reproduce the energy exchange rate, where one continuous variable was introduced to represent the internal energies of a molecular gas. Although DSMC is widely used for rarefied gas flows, it is very time-consuming for oscillating problems (Park et al., 2004). The time step has to be significantly small (compared

with both the molecular mean free time and the time period of oscillations) and the total simulation time should be sufficiently long to ensure that the time-periodic state is achieved. In addition, in an unsteady DSMC algorithm, ensemble averaging over thousands of different simulations for each time step is necessary to yield noise-reduced solutions.

The DVM, on the other hand, falls into the category of deterministic approaches. It relies on direct discretisation of the governing equation over computational grids and so can produce noise-free solutions. Furthermore, by assuming small variations in flow properties, the time-periodic flow can be converted into a quasi-steady-state problem and the computational cost will be greatly reduced (see Section 3.2.2). Therefore, in this work, we use the DVM and a deterministic-based model (Q. Li et al., 2021; Su, Li, Zhang, & Wu, 2022) to investigate wave propagation in rarefied molecular gases, which is modified from the Rykov model (Rykov, 1975). The model is able to recover the general temperature and thermal relaxation rates that are predicted by the Wang-Chang–Uhlenbeck equation and can freely adjust the relevant relaxation rates. Therefore, it can simultaneously obtain experimentally measured values of the bulk viscosity and thermal conductivity for a given molecular gas (Q. Li et al., 2021; Su et al., 2022; Wu et al., 2020), and their effects on the wave propagation can be separately investigated. To avoid having too many parameters in the analysis, we assume that vibrations of gas molecules are not activated. This assumption has limitations for some polyatomic gases such as carbon dioxide and methane, where vibrational relaxation plays a crucial role in wave attenuation (Ejakov et al., 2003; Kustova et al., 2023). In such cases, a model taking into account both rotational and vibrational relaxations (Q. Li, Zeng, Huang, & Wu, 2023) is necessary, where additional relaxation rates are required. The rotational mode is considered through the classical mechanics approach, with a continuous variable representing the rotational energy. A brief description of the present kinetic model is given in the following.

In the gas kinetic theory, the state of a molecular gas with the excited rotational mode is described by a one-particle velocity-energy distribution function $f(t,\boldsymbol{x},\boldsymbol{v},I)$, which is a function of time t, spatial coordinate $\boldsymbol{x}=(x,y,z)$, molecular translational velocity $\boldsymbol{v}=(v_x,v_y,v_z)$, and rotational energy I. In the absence of external force, the evolution of f is governed by (Rykov, 1975; Su et al., 2022)

$$\frac{\partial f}{\partial t}+\boldsymbol{v}\cdot\frac{\partial f}{\partial \boldsymbol{x}}=\underbrace{\frac{p_t\delta_0}{\mu}\left(g_t-f\right)}_{\text{elastic}}+\underbrace{\frac{p_t\delta_0}{\mu Z}\left(g_r-g_t\right)}_{\text{inelastic}}. \tag{3.1}$$

It can be seen that the collision operator (the term on the right-hand side) that describes the change of f due to particle collisions is split into two parts: elastic collisions that preserve translational energy and inelastic ones that exchange translational and rotational energies. Both elastic and inelastic parts are expressed as a simple Shakhov relaxation term, which effectively retains accuracy up to third-order velocity moments, such as momentum and energy transport, but cannot capture higher-order non-equilibrium effects accurately. Thus, the

model is suitable in near-equilibrium regimes or in moderately rarefied flows, where higher-order moments are small. It becomes increasingly inaccurate in highly rarefied or far-from-equilibrium flows, such as strong shock structures. The relaxation time related to elastic collisions is $\mu/(p_t\delta_0)$ with μ, p_t and δ_0 being gas shear viscosity, pressure related to translational motions, and a constant rarefaction parameter, respectively. Here, Z is the rotational collision number such that a gas molecule would roughly experience one inelastic collision in every Z collisions, and g_t and g_r are the translational and rotational reference distribution functions, respectively. The reference distributions are a series of orthogonal polynomials, expanding at the local equilibrium distribution function $E = E_t(T) \times E_r(T)$, and can be expressed as

$$g_t = E_t(T_t) \times E_r(T_r) \left[1 + \frac{4\boldsymbol{q}_t \cdot \boldsymbol{c}}{15T_t p_t}\left(\frac{|\boldsymbol{c}|^2}{T_t} - \frac{5}{2}\right) + \frac{4\boldsymbol{q}_r \cdot \boldsymbol{c}}{dT_t p_r}\left(\frac{I}{T_r} - \frac{d}{2}\right)\right], \tag{3.2}$$

$$g_r = E_t(T) \times E_r(T) \left[1 + \frac{4\boldsymbol{q}' \cdot \boldsymbol{c}}{15Tp}\left(\frac{|\boldsymbol{c}|^2}{T} - \frac{5}{2}\right) + \frac{4\boldsymbol{q}'' \cdot \boldsymbol{c}}{dTp}\left(\frac{I}{T} - \frac{d}{2}\right)\right], \tag{3.3}$$

with E_t and E_r being the local Maxwellian distributions

$$E_t(T) = \frac{n}{(\pi T)^{3/2}} \exp\left(-\frac{|\boldsymbol{c}|^2}{T}\right), \tag{3.4}$$

$$E_r(T) = \frac{I^{d/2-1}}{\Gamma(d/2)T^{d/2}} \exp\left(-\frac{I}{T}\right). \tag{3.5}$$

In the above formula, d is the number of rotational degrees of freedom; $\Gamma(\cdot)$ is the gamma function; T_t, T_r, $\boldsymbol{q}_t = \left(q_t^x, q_t^y, q_t^z\right)$, and $\boldsymbol{q}_r = \left(q_r^x, q_r^y, q_r^z\right)$ are the translational and rotational temperatures, and the related heat fluxes, respectively; and $\boldsymbol{c} = \boldsymbol{v} - \boldsymbol{u}$ is the peculiar velocity with $\boldsymbol{u} = (u_x, u_y, u_z)$ being the gas bulk velocity. The overall temperature T is a weighted sum of the translational and rotational temperatures: $T = (3T_t + dT_r)/(3+d)$. The pressures are defined as $p_t = nT_t$, and $p = nT$ in terms of the translational and overall temperatures, respectively, where n is gas number density. Here $\boldsymbol{q}'$ and $\boldsymbol{q}''$ are two auxiliary heat fluxes, defined as the linear combinations of the translational and rotational heat fluxes (Q. Li et al., 2021)

$$\begin{bmatrix} \boldsymbol{q}' \\ \boldsymbol{q}'' \end{bmatrix} = \begin{bmatrix} (2-3A_{tt})Z+1 & -3A_{tr}Z \\ -A_{rt}Z & 1-A_{rr}Z \end{bmatrix} \begin{bmatrix} \boldsymbol{q}_t \\ \boldsymbol{q}_r \end{bmatrix}, \tag{3.6}$$

where A_{ij} ($i, j = t$ or r) are the thermal relaxation rates.

Here, density and temperatures are normalized by the reference density n_0 and temperature T_0, respectively; the shear viscosity by its value at the reference temperature μ_0; velocities by the most probable speed $v_m = \sqrt{2k_BT_0/m}$, where k_B is the Boltzmann constant and m is the molecular mass; spatial coordinates by the characteristic flow length H; time by H/v_m; the internal energy by k_BT_0; heat fluxes by $n_0k_BT_0v_m$; pressures by $n_0k_BT_0$; and the distribution

functions by $n_0 v_m^{-3}(k_B T_0)^{-1}$. The rarefaction parameter is therefore defined as

$$\delta_0 = \frac{p_0 H}{\mu_0 v_m}, \tag{3.7}$$

where $p_0 = n_0 k_B T_0$. It is inversely proportional to the unconfined length-based Knudsen number:

$$\mathrm{Kn}_l = \frac{\sqrt{\pi}}{2}\frac{1}{\delta_0}. \tag{3.8}$$

Considering a homogeneous infinite fluid, the kinetic model recovers the Jeans-Landau temperature relaxation model, i.e.,

$$\frac{\partial T_r}{\partial t} = \frac{p_t \delta_0}{\mu Z}(T - T_r). \tag{3.9}$$

In addition, the heat flux relaxation of the present model is consistent with that derived from the Wang-Chang–Uhlenbeck equation by Mason and Monchick (1962). The heat flux relaxation directly determines the thermal conductivity, as well as the translational and rotational contributions (Mason & Monchick, 1962; McCormack, 1968), i.e.,

$$\begin{bmatrix} \partial \boldsymbol{q}_t/\partial t \\ \partial \boldsymbol{q}_r/\partial t \end{bmatrix} = -\frac{p_t \delta_0}{\mu} \begin{bmatrix} A_{tt} & A_{tr} \\ A_{rt} & A_{rr} \end{bmatrix} \begin{bmatrix} \boldsymbol{q}_t \\ \boldsymbol{q}_r \end{bmatrix}. \tag{3.10}$$

Applying the Chapman-Enskog multiscale expansion to the kinetic model equation and retaining the terms up to the order of $O(1/\delta)$, the Navier-Stokes-Fourier equations can be derived, and the transport coefficients are obtained immediately. The dimensionless bulk viscosity μ_b (normalised by μ_0) is given by

$$\mu_b = \frac{2dZ}{3(d+3)}\mu, \tag{3.11}$$

while the dimensionless translational conductivity κ_t and rotational conductivity κ_r (normalised by $2k_B\mu_0/m$) are determined as

$$\begin{bmatrix} \kappa_t \\ \kappa_r \end{bmatrix} = \frac{\mu}{4} \begin{bmatrix} A_{tt} & A_{tr} \\ A_{rt} & A_{rr} \end{bmatrix}^{-1} \begin{bmatrix} 5 \\ d \end{bmatrix}. \tag{3.12}$$

In practice, it is more convenient to express the thermal conductivity by the Eucken factors (Eucken, 1913) ,

$$\frac{2\kappa_t}{\mu} = \frac{3}{2} f_t, \quad \frac{2\kappa_r}{\mu} = \frac{d}{2} f_r, \quad \frac{2\kappa}{\mu} = \frac{2(\kappa_t + \kappa_r)}{\mu} = \frac{3+d}{2} f_{eu}, \tag{3.13}$$

where $\kappa = \kappa_t + \kappa_r$ is the overall thermal conductivity and f_{eu}, f_t and f_r are the total, translational and rotational Eucken factors, respectively.

For the numerical solution of our kinetic equation, a boundary condition is required to determine the value of f at the boundary of a computational domain. Considering a non-absorbing wall with velocity $\boldsymbol{u}_w$ at the temperature T_w, all the gas molecules $(\boldsymbol{v}', \boldsymbol{I}')$ hitting the wall will return to the flow field with a new state $(\boldsymbol{v}, I)$. Given the unit normal vector, $\boldsymbol{n}$, of the wall pointing towards the gas, the velocity-energy distribution function of the molecules in the vicinity of the wall is

$$f_w = \begin{cases} f^-, & (\boldsymbol{v}' - \boldsymbol{u}_w) \cdot \boldsymbol{n} \leq 0, \\ f^+, & (\boldsymbol{v}' - \boldsymbol{u}_w) \cdot \boldsymbol{n} > 0, \end{cases} \tag{3.14}$$

where f^- and f^+ are the distributions of the incident and reflected molecules, respectively. The correlation between the incident and reflected distribution functions is defined through the reflection kernel $R(\boldsymbol{v}' \to \boldsymbol{v}, I' \to I)$ as

$$\begin{aligned} &(\boldsymbol{v} - \boldsymbol{u}_w) \cdot \boldsymbol{n} f^+(\boldsymbol{v}, I) \\ &\qquad = -\iint_{(\boldsymbol{v}' - \boldsymbol{u}_w) \cdot \boldsymbol{n} \leq 0} (\boldsymbol{v}' - \boldsymbol{u}_w) \cdot \boldsymbol{n} f^-(\boldsymbol{v}', I') R(\boldsymbol{v}' \to \boldsymbol{v}, I' \to I) \mathrm{d}\boldsymbol{v}' \mathrm{d}I', \end{aligned} \tag{3.15}$$

for all $(\boldsymbol{v}' - \boldsymbol{u}_w) \cdot \boldsymbol{n} > 0$. For a fully diffuse wall, the reflection kernel is

$$R(\boldsymbol{v}' \to \boldsymbol{v}, I' \to I) = \frac{2(\boldsymbol{v} - \boldsymbol{u}_w) \cdot \boldsymbol{n} I^{d/2-1}}{\pi \Gamma(d/2) T_w^{2+d/2}} \times \exp\left(-\frac{(\boldsymbol{v} - \boldsymbol{u}_w)^2}{T_w} - \frac{I}{T_w} \right). \tag{3.16}$$

Including rotational energy in the reflection kernel is justified, as gas–surface interactions are commonly assumed to cause complete randomization of the molecular state upon reflection. This randomization affects not only translational velocities but also rotational degrees of freedom. Physically, collisions between gas molecules and solid surfaces typically lead to efficient equilibration of rotational modes with the wall temperature. As a result, the assumption of full accommodation for rotational energy is appropriate in many practical applications.

3.2.2 Formulation of Wave Propagation

The schematic diagram of the simulation set-up is shown in Figure 3.1. Here, we specify the formulation of wave propagation in rarefied molecular gases confined between two infinite, parallel and impermeable plates located at $x = 0$ and $x = 1$, which can be treated as a simple prototype of wave propagation in confined space. The plate at $x = 0$ may oscillate harmonically at a constant frequency ω in its normal direction so that the velocity varies as

$$u_w(t) = U_m \mathrm{Re}\{\exp(\mathrm{i}\mathrm{St}t)\}, \tag{3.17}$$

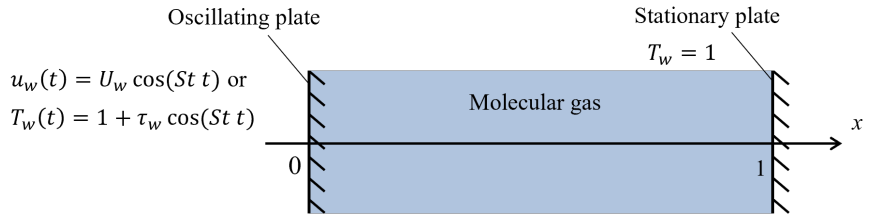

Figure 3.1: Schematic diagram of sound and thermal-acoustic wave propagation in rarefied molecular gases between two infinite, parallel and impermeable plates. The oscillating plate is positioned at $x = 0$ with harmonically varying velocity (along the x direction) or temperature, and the stationary plate is at $x = 1$. The stationary plate has a fixed temperature of $T_w = 1$. Both plates are fully diffuse walls.

and a sound wave is induced in the gas. This plate is also imposed unsteady heating, so that its temperature varies as

$$T_w(t) = 1 + \tau_m \mathrm{Re}\{\exp(\mathtt{i}\mathrm{St}t)\}, \tag{3.18}$$

and a thermal-acoustic wave is consequently induced. In Eq. 3.17 and Eq. 3.18, $\mathtt{i}$ is the imaginary unit, $\mathrm{Re}\{\cdot\}$ denotes the real part of a complex expression, and U_m and τ_m are the maximum speed and perturbed temperature of the plate, respectively. The constant St is the normalized oscillation frequency, defined as the Strouhal number:

$$\mathrm{St} = \frac{\omega H}{v_m}. \tag{3.19}$$

Note that the two driving forces have the same frequency. The time-based Knudsen number correlates with Kn_l and St through

$$\mathrm{Kn}_t = \frac{\mu_0 \omega}{p_0} = \frac{2Kn_l St}{\sqrt{\pi}}, \tag{3.20}$$

where p_0/μ_0 is the reference collision frequency of gas molecules.

We are interested in the flow state when the oscillation has been fully established. As a consequence, the time-dependent behaviour of the gas is periodic with the same frequency as the oscillation stimuli. We further assume that the velocity and perturbed temperature of the plate are sufficiently small quantities, i.e., $u_m \ll 1$ and $\tau_m \ll 1$, hence, the gas system deviates slightly from its reference equilibrium state, which is described by the global Maxwellian

$$E_0 = \frac{I^{d/2-1}}{\pi^{3/2}\Gamma(d/2)} \exp\left(-|\boldsymbol{v}|^2 - I\right), \tag{3.21}$$

and the kinetic equations can be linearized by representing the distribution function as

$$f(t,x,\boldsymbol{v},I) = E_0\left[1 + \mathrm{Re}\left\{h(x,\boldsymbol{v},I)\exp(\mathtt{i}\mathrm{St}t)\right\}\right], \tag{3.22}$$

where $|h| \ll 1$ is the amplitude of the perturbed distribution function. The macroscopic flow properties of interest are also expressed by the following complex functions

$$\begin{aligned} n(t,x) &= 1 + \mathrm{Re}\left\{\rho(x)\exp(\mathtt{i}\mathrm{St}t)\right\}, \\ u_x(t,x) &= \mathrm{Re}\left\{U(x)\exp(\mathtt{i}\mathrm{St}t)\right\}, \\ T_t(t,x) &= 1 + \mathrm{Re}\left\{\tau_t(x)\exp(\mathtt{i}\mathrm{St}t)\right\}, \\ T_r(t,x) &= 1 + \mathrm{Re}\left\{\tau_r(x)\exp(\mathtt{i}\mathrm{St}t)\right\}, \\ q_t^x(t,x) &= \mathrm{Re}\left\{Q_t(x)\exp(\mathtt{i}\mathrm{St}t)\right\}, \\ q_r^x(t,x) &= \mathrm{Re}\left\{Q_r(x)\exp(\mathtt{i}\mathrm{St}t)\right\}, \\ p_{xx}(t,x) &= 1 + \mathrm{Re}\left\{P(x)\exp(\mathtt{i}\mathrm{St}t)\right\}, \end{aligned} \tag{3.23}$$

where p_{xx} is the gas pressure in the direction of wave propagation. Here $[\rho, U, \tau_t, \tau_t, Q_t, Q_r, P]$ are complex functions, which can be represented in the exponential form as

$$M(x) = M_{am}(x)\exp\left[\mathtt{i}\phi_M(x)\right], \quad M = \rho, U, \tau_t, \tau_r, Q_t, Q_r, P, \tag{3.24}$$

where M_{am} and ϕ are the real functions corresponding to the amplitude and phase of a periodic function. Note that for the spatial coordinates, all the variables depend only on x, since the propagation of wave is restricted in this direction.

Substituting Eq. 3.22 and Eq. 3.23 into the kinetic equation Eq. 3.1 and neglecting all the nonlinear terms, we obtain the equation for h, written as

$$\begin{aligned} i\mathrm{St}h + v_x\frac{\partial h}{\partial x} =& \delta_0\left[\rho + 2Uv_x + \tau_t\left(|\boldsymbol{v}|^2 - \frac{3}{2}\right) + \tau_r\left(I - \frac{d}{2}\right)\right. \\ &\left. + \frac{4}{15}Q_t v_x\left(|\boldsymbol{v}|^2 - \frac{5}{2}\right) + \frac{4}{d}Q_r v_x\left(I - \frac{d}{2}\right) - h\right] \\ &+ \frac{\delta}{Z}\left[(\tau - \tau_t)\left(|\boldsymbol{v}|^2 - \frac{3}{2}\right) + (\tau - \tau_r)\left(I - \frac{d}{2}\right)\right. \\ &\left. + \frac{4(Q' - Q_t)\boldsymbol{v}}{15}\left(|\boldsymbol{v}|^2 - \frac{5}{2}\right) + \frac{4(Q'' - Q_r)\boldsymbol{v}}{d}\left(I - \frac{d}{2}\right)\right], \end{aligned} \tag{3.25}$$

where $\tau = (3\tau_t + d\tau_r)/(3+d)$, and Q' and Q'' are related to Q_t and Q_r according to Eq. 3.6. The boundary condition for h is

$$\begin{aligned} h^+ =& \sqrt{\pi}U_m - 2\sqrt{\pi}\iint_{v_x' \le 0} v_x' E_0 h^- \mathrm{d}\boldsymbol{v}'\mathrm{d}I' \\ &+ 2U_m v_x + \tau_m\left(|\boldsymbol{v}|^2 - \frac{5}{2}\right) + \tau_m\left(I - \frac{d}{2}\right), \quad \text{at } x = 0, \\ h^+ =& 2\sqrt{\pi}\iint_{v_x' > 0} v_x' E_0 h^- \mathrm{d}\boldsymbol{v}'\mathrm{d}I', \quad \text{at } x = 1, \end{aligned} \tag{3.26}$$

where h^+ and h^- denote the reflected and incident perturbed distribution functions. Once h is known, the macro-quantities are calculated from the velocity moments as

$$\begin{aligned}&[\rho, U, \tau_t,\ \tau_r, Q_t, Q_r, P] \\ &\quad = \iint \left[1, v_x, \frac{2}{3}|\boldsymbol{v}|^2 - 1, \frac{2}{d}I - 1, v_x\left(|\boldsymbol{v}|^2 - \frac{5}{2}\right), v_x\left(I - \frac{d}{2}\right), v_x^2\right] E_0 h \mathrm{d}\boldsymbol{v}\mathrm{d}I.\end{aligned} \tag{3.27}$$

By introducing complex expressions, the time variable in the governing equation system is eliminated. The technique of computational fluid dynamics for time-independent problems is adopted to find deterministic solutions, which can greatly reduce the computational cost. The details about the computational issues are given in the following section and Appendix A. Note that this method cannot be used to simulate the propagation of a strong wave with large amplitude. In such a circumstance, the assumption that variant flow properties have the same oscillating frequency as the external stimuli may break down, and a weak shock wave may be generated and propagate in space (Cox, Mortell, & Reck, 2002; Tang, Cheng, & Xu, 2001). Then, time-dependent nonlinear kinetic equations should be applied to investigate such flows. Numerical methods with efficient shock-capture schemes, e.g. the unified gas kinetic schemes, should be used (P. Wang et al., 2018; R. J. Wang & Xu, 2012).

3.3 Results and Discussion

In this section, we investigate sound and thermoacoustic wave propagation in rarefied molecular gases. A wide range of rarefactions and oscillation frequencies will be considered. The influence of non-equilibrium relaxations between the translational and rotational modes, in particular the bulk viscosity μ_b and the Eucken factors f_t and f_r, will be examined.

3.3.1 Validation of Kinetic Model and Numerical Scheme

As the disturbance in the gas is restrained to the x direction, the dependence of the governing equation system on v_y, v_z and I can be eliminated by introducing auxiliary distribution functions that have independent variables x and v_x. The details of the reduced system, which is to reduce computational cost, are explained in Appendix A. The kinetic equations are solved by the DVM, where v_x is truncated to the range of $[-6, 6]$ and partitioned by N_v non-uniformly distributed points according to

$$v_x = \frac{6}{(N_v - 1)^3}(-N_v + 1, -N_v + 3, ..., N_v - 1)^3. \tag{3.28}$$

In this partition, the majority of the discrete velocities are located around $v_x = 0$; consequently, it is able to capture the discontinuity and rapid oscillation in the perturbed velocity distribution function near $v_x = 0$ at the plate positioned at $x = 0$ (Kalempa & Sharipov, 2009; Wu, 2016). We set $N_v = 80$, 300 and 300 for $Kn = 0.01, 0.1$ and 10 respectively to obtain smooth solutions. The spatial domain $x \in [0,1]$ is divided into N_x elements, with the element boundary nodes determined using a cubic smoothstep-based mesh transformation function:

$$x = s^3(10 - 15s + 6s^2), \quad s = \frac{(0,1,...,N_x)}{N_x}. \tag{3.29}$$

This transformation clusters grid points near the boundaries (i.e., the vicinity of the two plates), while ensuring a smooth variation in cell size across the entire domain (Wu, 2016). We set $N_x = 64$ for all the cases. The spatial derivatives are approximated using a fourth-order Discontinuous Galerkin (DG) method. This method divides the domain into non-overlapping elements, within which the solution is represented by local polynomials of degree three, achieving fourth-order accuracy in space. Unlike continuous Galerkin methods, the DG formulation allows for discontinuities at element interfaces, which are handled using numerical flux functions to ensure stability and conservation. This approach provides both high-order accuracy and geometric flexibility, making it well-suited for capturing complex solution features such as sharp gradients or wave propagation with high resolution. To seek stable solutions, a semi-implicit time iterative scheme is applied, in which the convection term is treated implicitly at the $(t+1)th$ iteration step, while the collision operator is evaluated explicitly at the $(t)th$ step. The iteration stops when the residuals of density, velocity and temperatures are less than 10^{-7}. The details of the numerical scheme can be found in Su, Wang, Zhang, and Wu (2020). The independence of the obtained results with respect to the velocity and spatial grids has been verified. When the number of discrete velocities and spatial elements is further doubled, the maximum difference in macroscopic quantities continues to decrease. Specifically, the difference remains below 1% for key macroscopic quantities, including the pressure amplitude, which is used as a criterion for convergence.

We validate our numerical solutions by comparing them with the experimental measurements of Greenspan (1959). In the experiment, the working gas was nitrogen, and all measurements were conducted in a two-crystal interferometer. The emitting crystal was fixed and energised at a constant voltage by a crystal-controlled electron-coupled oscillator, generating a sound frequency of approximately 1 MHz. The receiving crystal was connected to a movable slider while the displacement of the crystal receiver was measured. Processed through the filter and amplifier, the change in gas pressure was finally obtained.

The rotational degree of freedom for nitrogen is $d = 2$. For numerical solutions, we consider the velocity wave and set the rotational collision number to $Z = 2.67$ and the thermal relaxation rates to $A_{tt} = 0.786$, $A_{tr} = -0.201$, $A_{rt} = -0.059$, and $A_{rr} = 0.842$, thus $f_{eu} = 1.993$, $f_t = 2.365$ and $f_r = 1.435$. These parameters are measured from the DSMC simulation in order

to match the total thermal conductivity of nitrogen at $T_0 = 300$ K obtained from the Rayleigh-Brillouin scattering (Q. Li et al., 2021; Wu et al., 2020). The numerical and experimental results are compared in terms of the variations of the dimensionless attenuation coefficient α and sound speed v_{ph} against Kn_t. These acoustic parameters can be expressed in terms of the amplitude P_{am} and ϕ_P of the perturbed gas pressure at $x = 1$ as

$$\alpha = -\sqrt{\frac{\gamma}{2}}\frac{\mathrm{d}\ln P_{am}}{\mathrm{d}St}, \quad v_{ph} = \frac{c_0}{\beta}, \tag{3.30}$$

where $\gamma = 7/5$ is the ratio of specific heats for linear molecules, c_0 is the adiabatic sound speed and β is the dimensionless phase parameter defined as

$$\beta = \sqrt{\frac{\gamma}{2}}\frac{\mathrm{d}\phi_P}{\mathrm{d}St}. \tag{3.31}$$

Numerical solutions of α and β are obtained by the pointwise method (Garcia & Siewert, 2005; Sharipov, Marques Jr, & Kremer, 2002; R. J. Wang & Xu, 2012). The P_{am} and ϕ_P can be obtained using Eq. 3.24.

In the experiment, the Strouhal number St was controlled by adjusting the distance between the sound source and the receptor since the oscillation frequency was fixed. In addition, P_{am} and ϕ_P depend strongly on St (Sharipov et al., 2002; Struchtrup, 2012); see Figures 3.2(a) and (b). When St is small, i.e., the source and the receptor are close to each other, distinctive peaks and valleys appear in P_{am} due to resonance. As the distance between the plates grows, no resonance is observed because of the strong damping in a rarefied gas, resulting in very weak reflected wave. Note that the phase ϕ_P also exhibits a non-monotonous variation when St is small. Since no data were provided for the geometrical set-up of the sound source and receptor in the experiment, in order to eliminate the influence of resonance, $\mathrm{d}(\ln P_{am})/\mathrm{d}St$ and $\mathrm{d}\Phi_P/\mathrm{d}St$ in Eq.3.30 and Eq. 3.31 are determined by the linear tails of the curves in Figure 3.2(a) and (b). Figure 3.2(c) shows the comparison between the simulated and measured results, from which we found that our simulations can capture the essential acoustic properties of sound wave propagation in rarefied molecular gases.

3.3.2 Investigation of Gas Damping

Because of energy dissipation, gas damping occurs in sound wave propagation. In this section, the change of pressure amplitude is used to describe the property of gas damping in the flow channel. The gas is nitrogen, and the free parameters d, Z, and A_{ij} are the same as those used in the previous section. Figure 3.3 shows the profile of pressure amplitude under different Kn_l and St.

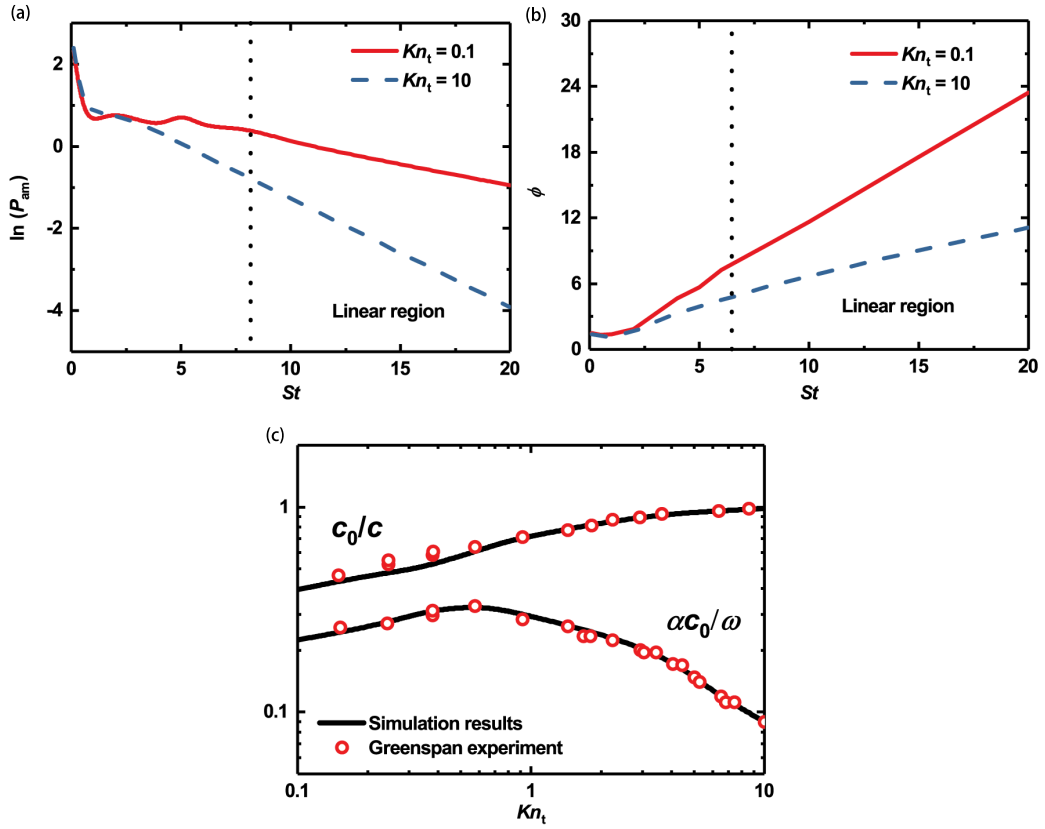

Figure 3.2: Model validation: (a) variation of the pressure amplitude on the receptor with the Strouhal number St; (b) variation of the phase on the receptor with St; (c) comparison of dimensionless sound speed and attenuation coefficient between the simulation results and the experimental data (Greenspan, 1959).

In a confined flow, resonance and anti-resonance will appear due to the superposition of incident and reflected waves. The intensity of resonance is determined by the reflected wave as the input energy is constant. In Figure 3.3(a), the collisions between particles are more frequent with smaller St and Kn_l, which means more energy can be transferred to the receptor, resulting in the stronger reflected wave. Consequently, the resonance is stronger as well. It can be seen that the pressure amplitude at the entrance is smaller than that at the receptor because of anti-resonance. With increasing Strouhal number, e.g., $St = 4$ in Figure 3.3(b), the reflected wave is weaker and the pressure amplitude at the entrance is larger than that at the receptor when $Kn_l \geq 0.1$. In Figure 3.3(c), the collisions between particles are infrequent as St is large. The resonance becomes obvious when Kn is large.

Now we investigate the influence of bulk viscosity on gas damping. In addition to nitrogen, we consider two more pseudo-gases with the rotational collision number Z being 113 and 14250; the other parameters d and A_{ij} remain the same as those for nitrogen. Note that the choice of high Z values was made to investigate the impact of extremely slow relaxation. Previous

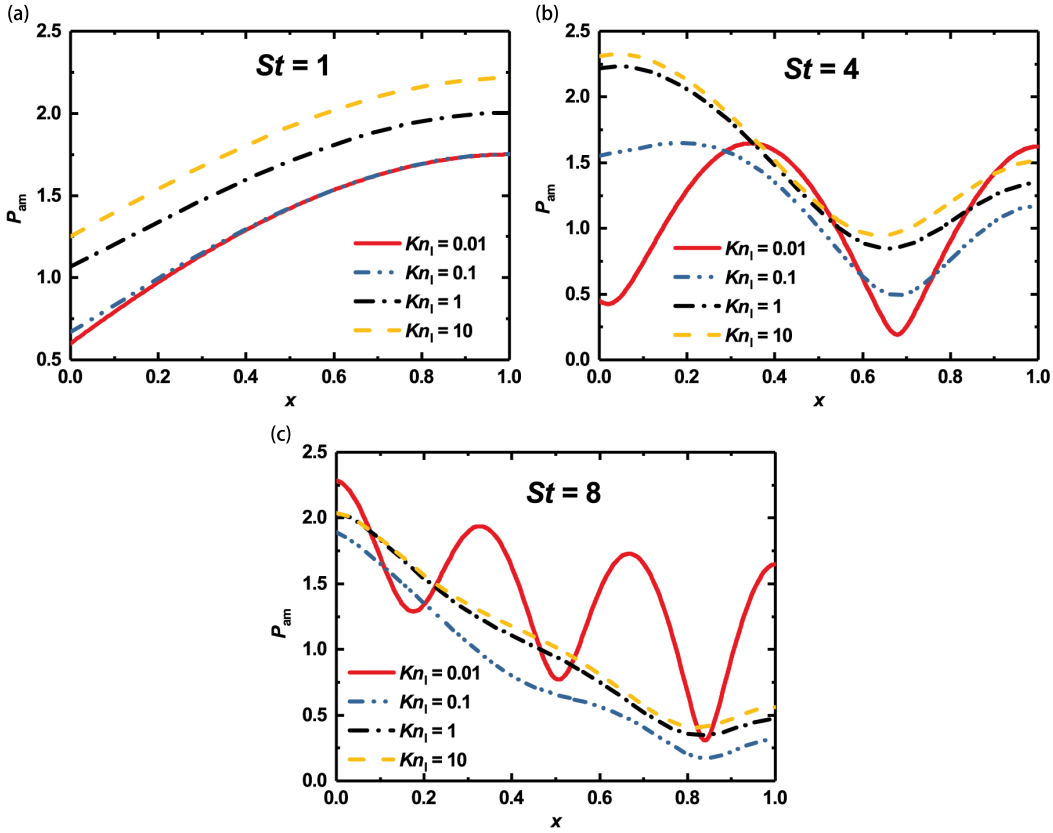

Figure 3.3: The change of pressure amplitude in the x direction: (a) $St = 1$; (b) $St = 4$; (c) $St = 8$. Here Kn_l is set to be 0.01, 0.1, 1 and 10.

estimations based on sound attenuation coefficients showed that certain real gases, such as CO_2, may exhibit large rotational collision numbers and bulk viscosity at low temperature (Cramer, 2012). However, recent experimental evidence has indicated that the ratio of the bulk to shear viscosity is approximately 3-5 for CO_2 at low temperature (Y. Wang, Ubachs, & Van De Water, 2019). Therefore, the high rotational collision number is a result of incorrect splitting of rotational and vibrational modes, and the slow vibrational relaxation should be taken into account when predicting the high attenuation coefficient in CO_2 (Kustova et al., 2023). For comparison, we also simulate the sound wave propagation in a monatomic gas, which is described by the Shakhov equation (Kalempa & Sharipov, 2009). The profiles of pressure amplitude along the flow channel are shown in Figure 3.4. When Kn_l and/or St are relatively large, e.g., $Kn_l = 0.1$, $St = 8$, or $Kn_l = 10$ regardless of St, there is no difference between the simulated gases. This is because the bulk viscosity exerts influence through inelastic collisions; when the degree of rarefaction is high, the molecular collisions are infrequent, so the pressure profiles are not affected by bulk viscosities as they rely on translational energy and there is negligible energy transfer between translational and rotational energies. When Kn_l and St decrease, the particle collisions become more frequent, so the bulk viscosity

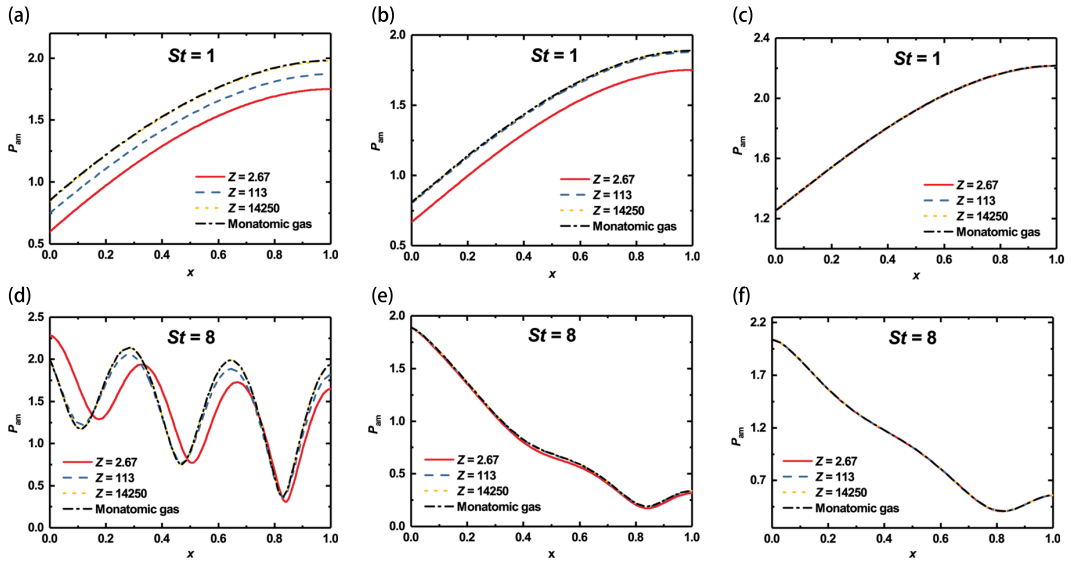

Figure 3.4: The change of pressure amplitude in the x direction under various rotational collision numbers. A wide range of rarefaction and oscillation frequencies are simulated: (a) $St = 1$, $Kn_l = 0.01$; (b) $St = 1$, $Kn_l = 0.1$; (c) $St = 1$, $Kn_l = 10$; (d) $St = 8$, $Kn_l = 0.01$; (e) $St = 8$, $Kn_l = 0.1$; (f) $St = 8$, $Kn_l = 10$.

plays an important role in determining the pressure amplitude. Interestingly, the pressure amplitude of a molecular gas with large bulk viscosity is very close to that of a monatomic gas under all the considered Knudsen and Strouhal numbers. This is because the internal degrees of freedom are frozen when Z is large, i.e., inelastic collisions are rare. The underlying mechanism will be further discussed in Section 3.3.3.

Now we investigate the influence of thermal conductivity on gas damping by changing the values of the translational and rotational Eucken factors. We keep the rotational collision number $Z = 2.67$, the total Eucken factor $f_{eu} = 1.993$, $A_{tr} = -0.201$ and $A_{rt} = -0.059$ the same as the experimental value of nitrogen. Figure 3.5 shows the pressure amplitude under translational Eucken factors of $1.5, 2.0$ and 2.5. The corresponding rotational Eucken factor and the two diagonal elements A_{tt} and A_{rr} can be obtained through Eq. 3.12 and Eq. 3.13. In contrast to the bulk viscosity, the thermal conductivity exerts limited influence on gas damping over a wide range of Kn_l and St.

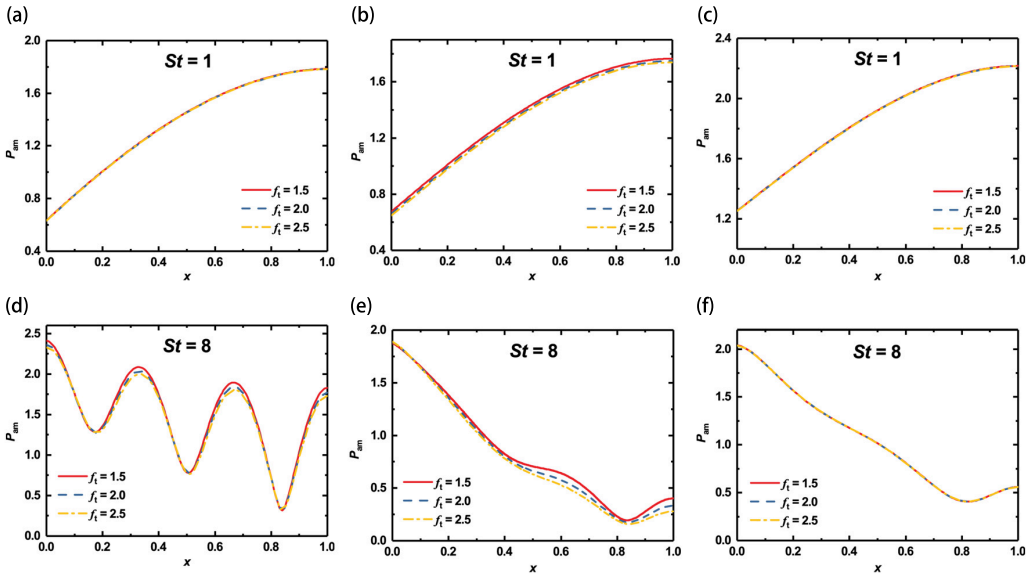

Figure 3.5: The change of pressure amplitude in the x direction under different translational Eucken factors. The gas is nitrogen. A wide range of rarefaction and oscillation frequencies are simulated: (a) $St = 1$, $Kn_l = 0.01$; (b) $St = 1$, $Kn_l = 0.1$; (c) $St = 1$, $Kn_l = 10$; (d) $St = 8$, $Kn_l = 0.01$; (e) $St = 8$, $Kn_l = 0.1$; (f) $St = 8$, $Kn_l = 10$.

3.3.3 Surface Force on Transducer

We now evaluate the surface force on the transducer in molecular gases, which can be obtained from the gas pressure at the plate. Therefore, we focus on the change of gas pressure amplitude at $x = 0$ under different transport coefficients and flow conditions.

The relationship between the pressure amplitude P_{am} and the Strouhal number St under different rotational collision number Z and Knudsen number Kn_l are shown in Figure 3.6. It is found that when Kn_l is not small, say equal to or larger than 1, the effect of particle collisions can be neglected and the profiles of P_{am} remain nearly unchanged regardless of Z. Therefore, we focus on examining the flow properties in three distinct flow regimes: $Kn_l = 0.01$, $Kn_l = 0.1$ and $Kn_l = 10$. In all the flow regimes, as St increases, P_{am} decreases until the first anti-resonance frequency and then increases to a peak value, which is referred to as the resonance frequency. After exceeding the first resonance frequency, P_{am} changes slightly and tends to be constant when St becomes large. In order to analyze P_{am} quantitatively, we first consider the case where the oscillation frequency is much larger than the mean molecular collision frequency, i.e., when $Kn_l St \gg 1$. In this case, the collision term in Eq. 3.25 can be neglected (Kalempa & Sharipov, 2009; Wu, 2016). Therefore, we obtain the reduced equation

$$i\mathrm{St}h + v_x \frac{\partial h}{\partial x} = 0. \tag{3.32}$$

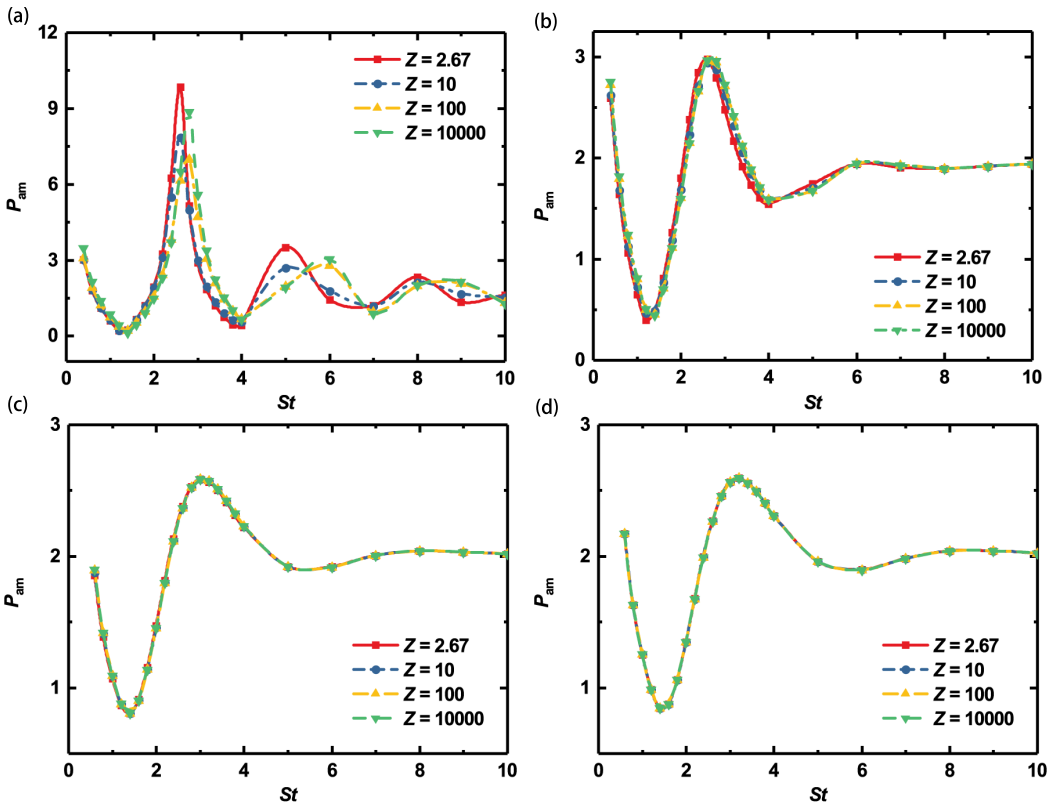

Figure 3.6: The relationship between the pressure amplitude and St under different rotational collision numbers. The results of four flow regimes are shown here: (a) $Kn_l = 0.01$, (b) $Kn_l = 0.1$, (c) $Kn_l = 1$ and (d) $Kn_l = 10$. The rotational collision number Z is set to 2.67, 10, 100, 10000, respectively.

Combining with the boundary condition on the left plate, we can finally obtain the value of pressure amplitude on the transducer $(x = 0)$ at the high-frequency limit as

$$P_{am}(x = 0) \to \frac{2}{\sqrt{\pi}} + \frac{\sqrt{\pi}}{2} \approx 2. \tag{3.33}$$

In Figure 3.6(b) and (d), when the frequency is large, e.g., St is larger than 6, P_{am} approaches 2. However, when Kn_l is 0.01 (see Figure 3.6(a)), P_{am} is slightly less than 2 at large Strouhal numbers owing to the fact that the particle collisions are frequent and cannot be neglected.

Now, we examine the anti-resonance and resonance frequencies. Through the confined flow channel, the molecules leave the left plate with velocity v_p, are reflected by the right plate, and finally return to the left plate. Without collision, the total travel distance for a molecule in the x direction is $2H$. Thus, we obtain the following equation:

$$2H \approx v_p \delta t, \tag{3.34}$$

where δt is the travel time of each molecule. When the travel time satisfies

$$\delta t = \frac{2n\pi}{\omega}, \quad \text{or } \frac{(2n-1)\pi}{\omega}, \quad n \in N_+, \tag{3.35}$$

the molecules leaving and coming back to the left plate have the same or opposite phase, corresponding to the resonance or anti-resonance point. Replacing ω by St, we finally obtain the resonance frequency St_r and anti-resonance frequency St_a as

$$St_r \approx \frac{v_p}{v_m} n\pi, \quad n \in N_+, \tag{3.36}$$

$$St_a \approx \frac{v_p}{v_m} \frac{(2n-1)\pi}{2}, \quad n \in N_+. \tag{3.37}$$

For free molecular flow ($Kn_l = 10$), the collisions between particles can be neglected and the travel distance of molecules in the x direction is $2H$. In addition, the gas flow slightly deviates from the global equilibrium state, thus $v_p \approx v_m$. Then, we obtain the first resonance frequency $St_r \approx \pi \approx 3.14$ and the first anti-resonance frequency $St_a \approx \pi/2 \approx 1.57$ through Eq. 3.36 and Eq. 3.37 which are consistent with the results shown in Figure 3.6(d). When $Kn_l = 0.1$ and $Kn_l = 0.01$, the increased frequency of collisions makes the free movement of molecules more difficult. Thus, the real travel time of particles is larger than $2H/v_p$. Therefore, the first resonance frequency and anti-resonance frequency are smaller than the respective theoretical values.

The influence of the bulk viscosity on the pressure amplitude at $x = 0$ is also investigated. As shown in Figure 3.6, the bulk viscosity only affects the pressure amplitude in the slip regime ($Kn_l = 0.01$). In the transition and free molecular flow regimes ($Kn_l = 0.1$ and $Kn_l = 10$), because of infrequent particle collisions, the bulk viscosity exerts limited influence on P_{am}. Therefore, we will focus only on the slip flow regime. From Figure 3.6(a), it is found that the value of P_{am} varies at a fixed St for different bulk viscosities. To reveal the underlying physics, we further plot the profile of P_{am} under different rotational collision numbers with different St numbers, see Figure 3.7(a). It can be seen that, with increasing Z, P_{am} is first found to monotonically converge to the constant value of a corresponding monatomic gas (i.e. the dotted line in Figure 3.7(a)). The result indicates that the internal degrees of freedom will be frozen for large bulk viscosities because of negligible inelastic collisions, as we have discussed in Section 3.3.2. We now further explain this phenomenon here. There is only one inelastic collision in a total of Z collisions, which transfers the energy between translational and internal energies. When Z is large, the inelastic collision frequency is low and then internal energy transfer can be ignored within the characteristic time of the flow field, so the pressure amplitude of molecular gases is equal to that of the corresponding monatomic gases. This is called the frozen state or the local thermodynamic equilibrium (Jaeger, Matar, & Müller, 2018).

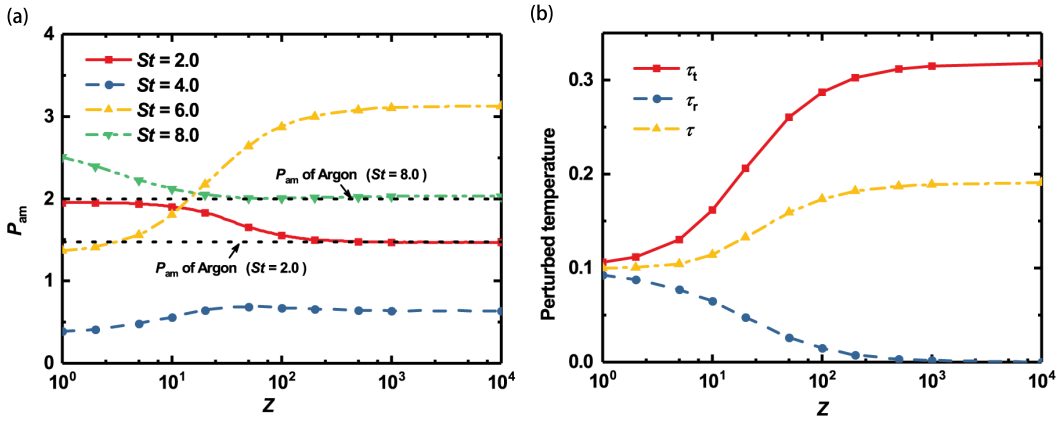

Figure 3.7: (a) The change of pressure amplitude under different rotational collision numbers with $St = 2.0, 4.0, 6.0$ and 8.0, where two dotted lines denote argon at $St = 2.0$ and $St = 8.0$; (b) amplitude of the translational, rotational and total temperatures for different rotational collision numbers with $St = 6.0$.

In order to provide more evidence, we plot the change of perturbed temperature under different Z with $St = 6.0$. As shown in Figure 3.7(b), the perturbed rotational temperature τ_r decreases continuously with the increase of Z due to the decrease of inelastic collision. When the rotational collision number is large, e.g., more than 1000, the perturbed rotational temperature is close to zero. Consequently, the perturbed overall temperature is reduced to $\tau \approx 0.6\tau_t$ for molecular gases ($d = 2$) as expected theoretically.

Figure 3.6(a) shows that the bulk viscosity also influences the resonance frequency. Specifically, the emergence of the resonance frequency will be delayed under large bulk viscosities, and this trend is more obvious when St is large. As mentioned previously, when the value of Z is reduced, inelastic collisions become more frequent. Such collisions result in higher rotational energy and lower translational energy of the gas molecules in sound wave propagation. This causes an increase in travel time. Consequently, the resonance frequencies decrease when the bulk viscosity decreases. For instance, when $Z = 2.67$ and 10, the first resonance frequencies are slightly smaller than those of $Z = 100$ and 10000. In addition, since the resonance state varies with bulk viscosity, the initial variation of P_{am} depends on St as shown in Figure 3.7(a).

The influence of thermal conductivity on the surface force is also investigated. The total Eucken factor is fixed as $f_{eu} = 1.993$ while the value of f_t is varied. As shown in Figure 3.8, the Eucken factor has little influence on the pressure amplitude and the resonance frequency.

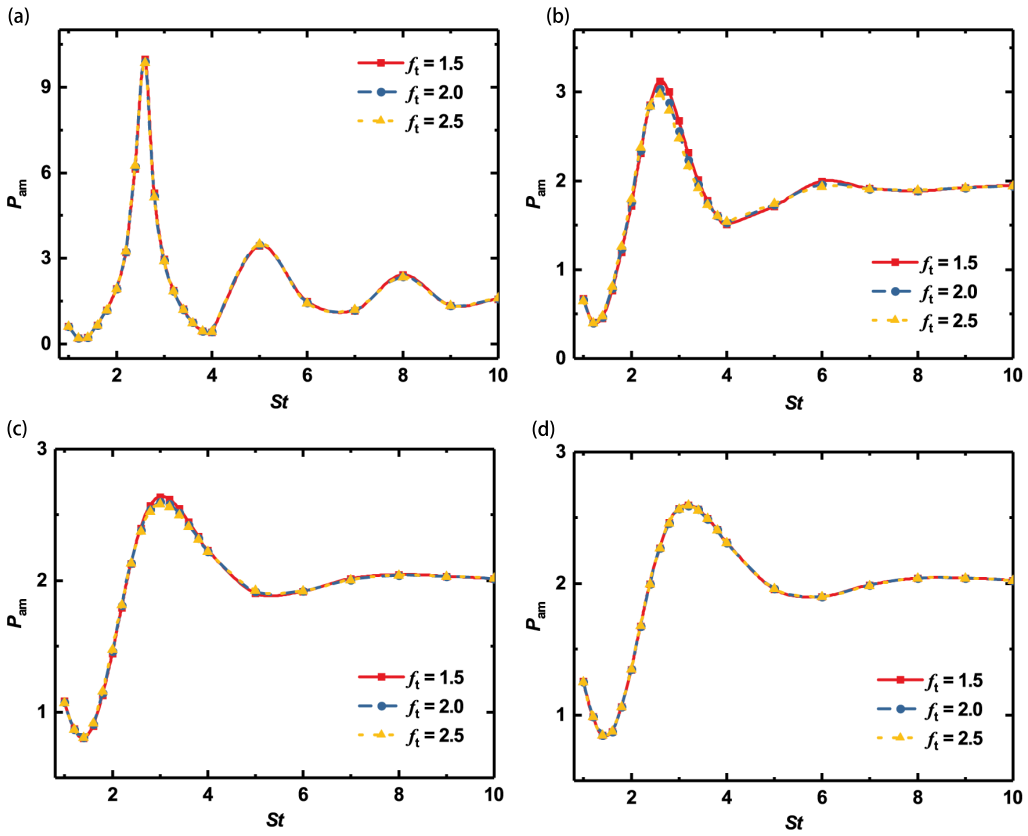

Figure 3.8: The relationship between the pressure amplitude and St number under different translational Eucken factors. Four flow regimes are investigated: (a) $Kn_l = 0.01$; (b) $Kn_l = 0.1$; (c) $Kn_l = 1$ and (d) $Kn_l = 10$. The translational Eucken factor f_t is set to 1.5, 2 and 2.5.

3.3.4 Onsager-Casimir Reciprocal Relationship

In this section, we examine whether the OCRR also holds for molecular gases. If we consider a weakly non-equilibrium system where some irreversible processes occur, then the corresponding physical law can be described in a general linear form as

$$J_k = \sum_n \Lambda_{kn} X_n, \tag{3.38}$$

where X_n are driven forces, J_k are conjugated thermodynamic fluxes and Λ_{kn} is the matrix of kinetic coefficients. The non-diagonal elements Λ_{kn} $(k \neq n)$ contain solutions corresponding to the forces X_k and X_n. If the form of the thermodynamic flow J_k is chosen so that the entropy production s in the statistical system is expressed as

$$s = \sum_k J_k X_k, \tag{3.39}$$

then the kinetic coefficients satisfy

$$\Lambda_{kn}^{t} = \Lambda_{nk}^{t}, \tag{3.40}$$

where the superscript t means that each coefficient Λ_{kn}, composed of two solutions k and n, is calculated from the time-reverted molecular state of one of these solutions.

From the Boltzmann equation, the thermodynamic fluxes and forces can be identified for gas flows, and the kinetic coefficients are derived as (Sharipov, 2006)

$$\Lambda_{kn} = \int_{\Sigma} \left(\boldsymbol{v} \cdot \boldsymbol{n} h_w^{(k)}, h^{(n)} - \frac{1}{2} h_w^{(n)} \right) \mathrm{d}\Sigma - i\mathrm{St} \left(\left(h^{(k)}, h^{(n)} \right) \right), \tag{3.41}$$

$$\Lambda_{kn}^{t} = \int_{\Sigma} \left(\mathscr{T} \boldsymbol{v} \cdot \boldsymbol{n} h_w^{(k)}, h^{(n)} - \frac{1}{2} h_w^{(n)} \right) \mathrm{d}\Sigma - i\mathrm{St} \left(\left(\mathscr{T} h^{(k)}, h^{(n)} \right) \right), \tag{3.42}$$

where Σ represents solid walls that enclose the flow field Ω; h_w is given by the wall velocity and temperature as

$$h_w = 2\boldsymbol{v} \cdot \boldsymbol{u}_w + \tau_w \left(|\boldsymbol{v}|^2 - \frac{5}{2} \right) + \tau_w \left(I - \frac{d}{2} \right), \tag{3.43}$$

and the binary operations $(\cdot, \cdot)$ and $((\cdot, \cdot))$ are defined for the two arbitrary functions as

$$(\phi, \psi) = \iint E_0 \phi(\boldsymbol{x}, \boldsymbol{v}, I) \psi(\boldsymbol{x}, \boldsymbol{v}, I) \mathrm{d}\boldsymbol{v} \mathrm{d}I, \tag{3.44}$$

$$((\phi, \psi)) = \int_{\Omega} (\phi, \psi) \, \mathrm{d}\boldsymbol{x}. \tag{3.45}$$

Finally, $\mathscr{T}$ is the operator reversing the state of molecules in time

$$\mathscr{T} \phi(\boldsymbol{x}, \boldsymbol{v}, I) = \phi(\boldsymbol{x}, \boldsymbol{v}^t, I^t), \tag{3.46}$$

which is self-conjugated, i.e.,

$$(\mathscr{T} \phi, \psi) = (\mathscr{T} \psi, \phi). \tag{3.47}$$

For the sound wave stimulated by oscillation of the transducer and the thermoacoustic wave induced by a temperature oscillation, the thermodynamic forces are defined as

$$X_U = u_m, \quad X_T = \tau_m, \tag{3.48}$$

and then the perturbed distribution can be expressed as

$$h(x, \boldsymbol{v}, I) = h^{(U)}(x, \boldsymbol{v}, I) X_U + h^{(T)}(x, \boldsymbol{v}, I) X_T. \tag{3.49}$$

In addition, h_w that defines the boundary condition can also be decomposed as

$$h_w(x,\boldsymbol{v},I) = h_w^{(U)}(x,\boldsymbol{v},I)X_U + h_w^{(T)}(x,\boldsymbol{v},I)X_T, \tag{3.50}$$

where

$$h_w^{(U)} = \begin{cases} 2v_x, & x=0, \\ 0, & x=1, \end{cases} \tag{3.51}$$

$$h_w^{(T)} = \begin{cases} \left(|\boldsymbol{v}|^2 - \frac{5}{2}\right) + \left(I - \frac{d}{2}\right), & x=0, \\ 0, & x=1. \end{cases} \tag{3.52}$$

Using the reciprocal relation, i.e., Eq. 3.38, the kinetic coefficients given by Eq. 3.41 and Eq. 3.42, and the self-conjugated property described by Eq. 3.47, we obtain

$$\begin{aligned} \left(\mathscr{T} v_x h_w^{(U)}, h^{(T)}\right)_{x=0} - \left(\mathscr{T} v_x h_w^{(U)}, h^{(T)}\right)_{x=1} &= \left(\mathscr{T} v_x h_w^{(T)}, h^{(U)}\right)_{x=0} - \left(\mathscr{T} v_x h_w^{(T)}, h^{(U)}\right)_{x=1} \\ &+ \left(\mathscr{T} v_x h_w^{(U)}, h_w^{(T)}\right)_{x=0} - \left(\mathscr{T} v_x h_w^{(U)}, h_w^{(T)}\right)_{x=1}. \end{aligned} \tag{3.53}$$

Inserting $h_w^{(U)}$ and h_w^T, we have

$$\begin{aligned} \left(\mathscr{T} 2|\boldsymbol{v}|^2, h^{(T)}\right)_{x=0} &= \left(\mathscr{T} v_x(|\boldsymbol{v}|^2 - \frac{5}{2}), h^{(U)}\right)_{x=0} + \left(\mathscr{T} v_x(I - \frac{d}{2}), h^{(U)}\right)_{x=0} \\ &+ \left(\mathscr{T} 2|\boldsymbol{v}|^2, (|\boldsymbol{v}|^2 - \frac{5}{2})\right)_{x=0} + \left(\mathscr{T} 2|\boldsymbol{v}|^2, (I - \frac{d}{2})\right)_{x=0}, \end{aligned} \tag{3.54}$$

thus

$$P^{(T)} = -Q_t^{(U)} - Q_r^{(U)} = -Q^{(U)}, \quad x=0. \tag{3.55}$$

If we use $h^{(T)}(1-x,\boldsymbol{v},I)$ instead of $h^{(T)}(x,\boldsymbol{v},I)$, the boundary condition is then transformed as

$$h_w^{(T)}(1-x) = \begin{cases} 0, & x=0, \\ \left(|\boldsymbol{v}|^2 - \frac{5}{2}\right) + \left(I - \frac{d}{2}\right), & x=1. \end{cases} \tag{3.56}$$

The reciprocal relation gives

$$\begin{aligned} \left(\mathscr{T} 2|\boldsymbol{v}|^2, h^{(T)}(1-x)\right)_{x=0} &= -\left(\mathscr{T} v_X(|\boldsymbol{v}|^2 - \frac{5}{2}), h^{(U)}(x)\right)_{x=1} \\ &- \left(\mathscr{T} v_X(I - \frac{d}{2}), h^{(U)}(x)\right)_{x=1}, \end{aligned} \tag{3.57}$$

and thus

$$P^{(T)} = Q_t^{(U)} + Q_r^{(U)} = Q^{(U)}, \quad x=1. \tag{3.58}$$

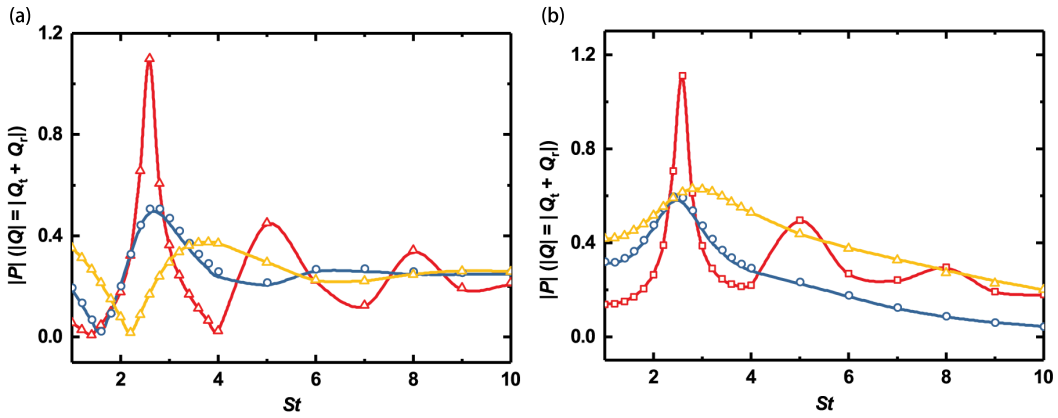

Figure 3.9: The variation of pressure amplitude and heat flux under different St: (a) $x = 0$ and (b) $x = 1$. The solid lines denote the pressure amplitude while the hollow points represent the heat flux. Three colors denote different flow regimes: red represents the slip regime ($Kn_l = 0.01$), blue represents the transition regime ($Kn_l = 0.1$), and yellow represents the free molecular flow regime ($Kn_l = 10$).

Therefore, OCRR for the wave propagation in molecular gases is confirmed by Eq. 3.55 and Eq. 3.58, which show that the magnitude of the deviation of gas pressure at the walls induced by the thermoacoustic wave is equal to the magnitude of the total heat flux (sum of the translational and internal heat fluxes) induced by the sound wave.

We further show the numerical results of the pressure amplitude and the total heat flux under a wide range of St and Kn_l. The results on the transducer and receptor are shown in Figure 3.9. In all the flow regimes, the pressure amplitude in the thermoacoustic wave agrees with the heat flux in the sound wave, suggesting that OCRR also holds for molecular gases.

The comparison between the pressure amplitude of the thermoacoustic wave and the total heat flux of the sound wave under different values of the bulk viscosity and thermal conductivity is shown in Figure 3.10. The simulation is conducted in the slip regime with $Kn_l = 0.01$. It is evident that OCRR is valid under different values of bulk viscosity and thermal conductivity. From the left column of Figure 3.10, we can see the influence of bulk viscosity and thermal conductivity on the thermoacoustic wave. In Figure 3.10(a), the resonance frequency is shifted when the bulk viscosity is altered, which is similar to the behaviour of the sound wave. The only difference lies in the value of P_{am}. In the case of the thermoacoustic wave, the pressure variation is generated by the oscillation of temperature, resulting in a significantly lower pressure amplitude than that in the sound wave. Figures 3.10(c) and (d) show that thermal conductivity has little influence on the pressure amplitude of the thermoacoustic wave and the heat flux amplitude of the sound wave.

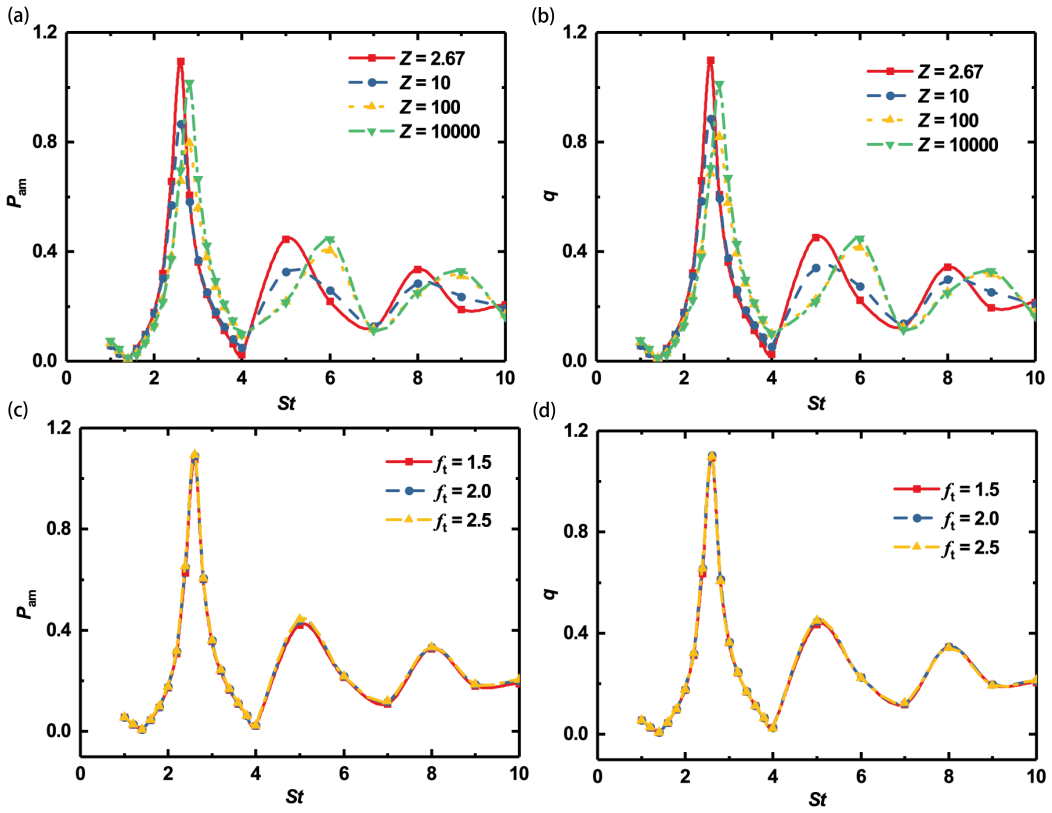

Figure 3.10: Comparison between the pressure amplitude of the thermoacoustic wave and the total heat flux of the sound wave under different values of the bulk viscosity and thermal conductivity. The pressure amplitude of the thermoacoustic wave is shown in (a,c) while the total heat flux of the sound wave is shown in (b,d).

3.4 Conclusions

We have investigated sound wave propagation in rarefied molecular gases over a wide range of rarefactions and oscillation frequencies. We first evaluate the influence of the transport coefficients on gas damping, and find that both rarefaction and oscillation frequency affect the pressure amplitude and resonance/anti-resonance of the sound wave. As for the transport coefficients, the bulk viscosity only exerts influence on the pressure amplitude at small Kn_l and St. At larger Kn_l and St, the pressure amplitude is not affected by the bulk viscosity. The pressure amplitude converges to the value of the corresponding monatomic gas as the bulk viscosity increases. Our results show that the internal degrees of freedom are frozen at large bulk viscosity, so the rotational mode has little influence and the results are similar to those for a monatomic gas. Meanwhile, thermal conductivity has a limited effect on the pressure amplitude and the total heat flux of the sound wave.

The propagation of thermoacoustic waves has also been investigated. We have proved, both analytically and numerically, that the OCRR holds for molecular gases.

Chapter 4

Simplified Kinetic Modelling of One-Dimensional Liquid-Vapour Flows: Evaporation Dynamics

N.B. This chapter has been published in: Li, S., Su, W., Shan, B., Li, Z., Gibelli, L., Zhang, Y. "Molecular kinetic modelling of non-equilibrium evaporative flows." *Journal of Fluid Mechanics* 994 (2024): A16.

Recent years have seen the emergence of new technologies that exploit nanoscale evaporation, ranging from nanoporous membranes for distillation to evaporative cooling in electronics. Despite the increasing depth of fundamental knowledge, there is still a lack of simulation tools capable of capturing the underlying non-equilibrium liquid-vapour phase changes that are critical to these and other such technologies. This work presents a molecular kinetic theory model capable of describing the entire flow field, i.e. the liquid and vapour phases and their interface, while striking a balance between accuracy and computational efficiency. In particular, unlike previous kinetic models based on the isothermal assumption, the proposed model can capture the temperature variations that occur during the evaporation process, yet does not require the computational resources of more complicated mean-field kinetic approaches. We assess the present kinetic model in three test cases: liquid-vapour equilibrium, evaporation into near-vacuum condition, and evaporation into vapour. The results agree well with benchmark solutions, while reducing the simulation time by almost two orders of magnitude on average in the cases studied. The results, therefore, suggest that this work is a stepping stone towards the development of an accurate and efficient computational approach to optimising the next generation of nanotechnologies based on nanoscale evaporation.

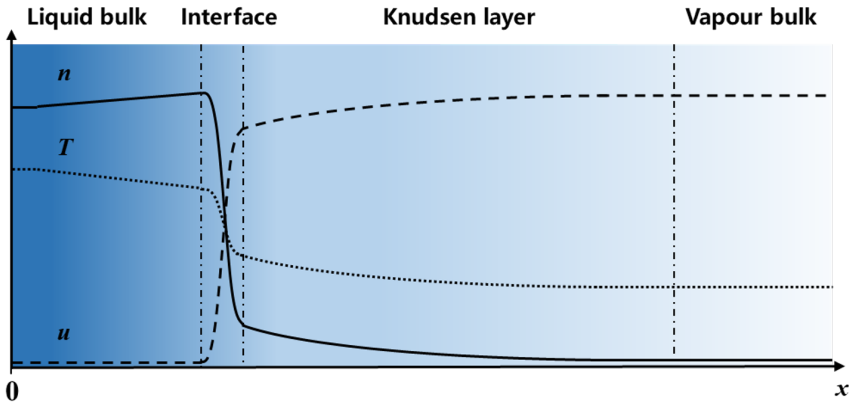

Figure 4.1: In evaporation, a bulk liquid region and a bulk vapour region are separated by a molecular scale interface. Adjacent to the interface on the vapour side is the non-equilibrium region Knudsen layer of the order of the mean free path. Across the interface and Knudsen layer, macroscopic quantities such as density n, velocity u, and temperature T undergo sharp transitions that appear discontinuous on the macroscale.

4.1 Literature Review

Evaporation is a ubiquitous phenomenon in nature and has many practical applications, such as evaporative cooling, material coating, and disease diagnosis (Brutin, Sobac, Loquet, & Sampol, 2011; Pinto, Silva, Porteiro, Míguez, & Baptista, 2018; Y. Yang, Cui, & Lan, 2019). With the emergence of nanotechnologies, these applications have now ventured into the realm of the nanoscale. One example is evaporative distillation using nanoporous membranes with pore diameters on the order of nanometres $(\sim 100\mathrm{nm})$, which allows unprecedented efficiency in the separation of substances (Dong, Poredoš, Ma, & Wang, 2022; Khayet, 2011). In addition, nanoscale evaporation processes are being exploited in electronic components to enable highly efficient heat dissipation (Khodabandeh & Furberg, 2010; Vaartstra et al., 2020). It is clear, therefore, that computational tools capable of accurately simulating nanoscale evaporative flow are paramount to the effective design and operation of these nanoscale devices. The accurate modelling of nanoscale evaporation processes poses, however, significant physical challenges due to the involvement of distinct spatial domains spanning multiple lengths and time scales.

As depicted in Figure 4.1, four regions can typically be distinguished in the flow field of an evaporating liquid: the liquid bulk, the interface, the Knudsen layer (which marks the initial region of the vapour phase) and the vapour bulk (Aursand & Ytrehus, 2019; Frezzotti, 2011; Frezzotti & Barbante, 2017). The interface (with a size of the order of a molecular diameter) and the Knudsen layer (with a size of the order of the mean free path) connect the liquid and vapour bulk regions. In these transitional layers, the fluid is in a non-equilibrium state, and

the macroscopic variables are subject to substantial variations, which manifest themselves as "jumps" on the macroscopic scale. Accurately representing the exchange of mass, momentum and energy between the vapour and the liquid bulk is a key problem in properly accounting for evaporation.

The vapour within the Knudsen layer is rarefied, and so extensive studies have been undertaken to investigate the flow dynamics within this region using classical gas kinetic theory (Frezzotti & Barbante, 2017; Ytrehus, 1997). About 140 years ago, Hertz and Knudsen formulated an expression for the evaporation mass flux in this region, known as the Hertz-Knudsen (H-K) formula (Hertz, 1882; Knudsen, 1915). While the H-K formula can capture some aspects of the evaporation process, its inability to account for the downstream vapour velocity hinders its accuracy in predicting flow properties (Aursand & Ytrehus, 2019; Persad & Ward, 2016). The H-K formula was later improved by Schrage (1953). While this modified equation is still widely used, it has shortcomings such as inapplicability beyond weak evaporation conditions (Vaartstra, Lu, Lienhard, & Wang, 2022). This gap in knowledge has been filled by subsequent contributions that incorporate the conservation of mass, momentum and energy. For evaporation from a planar liquid surface, the structure of the Knudsen layer and the jump relationships along this region have been well described using moment methods (Labuntsov & Kryukov, 1979; Meland & Ytrehus, 2003; Ytrehus, 1997). In parallel with the theoretical investigation, numerical simulations have been developed to address this problem under different flow conditions based on the Boltzmann equation or related kinetic models. For example, the evaporation of monatomic liquids has been simulated using the Bhatnagar-Gross-Krook (BGK) model and the Shahkov model (Aoki, Sone, & Yamada, 1990; Graur, Gatapova, Wolf, & Batueva, 2021; Sone, 1988). Evaporation flow properties in two-dimensional geometries, such as nanoporous membranes, have also been studied using the Direct Simulation Monte Carlo (DSMC) method (John et al., 2019, 2021; R. Li, Wang, & Xia, 2021; R. Li, Yan, & Xia, 2023; J. Wang, Xia, & Li, 2022). Although the above theoretical and numerical methods are well established, their treatment of evaporation is limited by the lack of resolution of the structure and dynamics of the liquid-vapour interface. As a result, the molecular exchange process with the liquid phase relies on a phenomenological boundary condition, which requires an evaporation coefficient parameter as an input. However, reported values for this coefficient in the literature span three orders of magnitude (Persad & Ward, 2016), introducing significant uncertainty.

In an attempt to determine the evaporation coefficient, the Enskog-Vlasov (EV) equation (Frezzotti et al., 2005a) was used as it allows one to describe both the liquid and vapour phases, including the interfacial region. The EV equation builds on the Boltzmann equation for dilute gases by incorporating two important extensions (Grmela, 1971; Karkheck & Stell, 1981; Sobrino, 1967). Firstly, the Enskog collision term is used to account for the dense fluid effects of increased molecular collision frequency and non-local interactions due to finite molecular volume, which are crucial for the description of the liquid phase and the interfacial region.

Secondly, a Vlasov self-consistent force term is included to account for long-range molecular attractive forces, which are crucial for capturing liquid-vapour phase transitions. Interestingly, a similar treatment of long-range interactions has been used in lattice Boltzmann models for multiphase fluid flows (He & Doolen, 2002; Huang, Wu, & Adams, 2021; Luo, 1998, 2000). The EV equation has been solved mainly by a particle method, which is an extension of the Direct Simulation Monte Carlo (DSMC) method to dense fluids (Frezzotti et al., 2019, 2005a). Numerical studies have provided many interesting insights into the evaporation of monatomic and polyatomic fluids (Busuioc & Gibelli, 2020; Frezzotti et al., 2019, 2005a; Ohashi, Kobayashi, Fujii, & Watanabe, 2020).

The EV equation has two main limitations that have prevented its widespread practical application in engineering flows. Firstly, it treats molecules as hard spheres, resulting in transport coefficients of a hard sphere fluid. However, the model can be extended to emulate real fluids by including a state-dependent hard sphere diameter, where higher temperatures correspond to smaller molecular diameters (Karkheck & Stell, 1981), and by considering attractive contributions from the intermolecular potential (B. Shan et al., 2023). Secondly, the numerical solution of the EV equation proves to be computationally demanding, largely due to the complexity of the Enskog collision term. Consequently, there is a growing interest in developing kinetic models for liquid-vapour flows based on simpler collision terms (T. Chen, Wu, Wang, & Chen, 2023; Takata & Noguchi, 2018; Y. Zhang et al., 2020). However, existing models rely on the assumption of constant temperature, which limits their usefulness in scenarios with minimal temperature variations. While Takata, Matsumoto, and Hattori (2021) has proposed a kinetic model that removes this isothermal constraint, further studies are needed to validate its effectiveness in handling evaporation processes.

In this work, we develop a kinetic model that can be easily extended to account for real fluid effects on the transport coefficients, and that is simpler than the EV equation, both in its mathematical formulation and in its numerical solution, but with a similar level of accuracy. Building on our previous work (B. Shan et al., 2023; Su, Gibelli, Li, Borg, & Zhang, 2023; P. Wang et al., 2020), we simplify the Enskog collision term by approximating its terms non-local in space by a Taylor series expansion truncated to the first-order derivatives in the molecular diameter, replacing the zero-order term by the Shakhov model. The proposed kinetic model is tested on three different scenarios to assess its ability to capture the essential physics and its accuracy: liquid-vapour equilibrium, evaporation into near-vacuum condition, and evaporation into vapour. The simulation results are compared with those obtained from the EV equation and analytical solutions. The very good agreement shows that our approximate kinetic model can provide a realistic description of liquid-vapour flows.

The rest of the chapter is organized as follows. Section 4.2.1 presents the kinetic model. Section 4.2.2 outlines the simulation setup while Section 4.3 addresses several aspects of the evaporation processes, namely the liquid-vapour equilibrium, evaporation into near-vacuum condition, and the structure of the Knudsen layer during evaporation into vapour. Finally, Section 4.4 concludes with a summary of our work and future research directions.

4.2 Methodology

4.2.1 Kinetic Model

We consider a fluid consisting of identical spherical atoms with mass m and diameter σ interacting via the Sutherland potential $\phi(r)$ defined by the superposition of the repulsive hard sphere core and an attractive smooth tail, i.e.,

$$\phi(r) = \begin{cases} +\infty, & r < \sigma, \\ -\phi_\sigma \left(\frac{r}{\sigma}\right)^{-\gamma}, & r \geq \sigma, \end{cases} \tag{4.1}$$

where ϕ_σ and γ are two positive constants related to the depth of the potential well and the extent of the soft interaction, respectively, and $r = ||\boldsymbol{x}_1 - \boldsymbol{x}||$ is the distance between the interacting atoms at $\boldsymbol{x}_1$ and $\boldsymbol{x}$. Compared to more realistic potentials, such as the Lennard-Jones, the Sutherland potential strikes a good balance between accuracy and simplicity in representing intermolecular interactions. On the one hand, the hard sphere component accounts for finite intermolecular repulsion at short distances, preventing unrealistic molecular overlap, which is particularly important in dense fluids; on the other hand, the attractive tail captures the forces that hold molecules together, which is essential for accurately describing the liquid-vapour phase transition.

The fluid is then described statistically by introducing the distribution function $f(\boldsymbol{x}, \boldsymbol{\xi}, t)$, which gives the number of atoms at time t in the elementary volume of the single-particle phase space around the position $\boldsymbol{x}$ and the velocity $\boldsymbol{\xi}$. A closed-form evolution equation for the distribution function can be derived, assuming that long-range particle correlations are negligible, and short-range particle correlations can be approximated by the Enskog theory of dense gases (Frezzotti et al., 2005a; Grmela, 1971; Karkheck & Stell, 1981; Sobrino, 1967). The resulting equation, called the EV equation, reads

$$\frac{\partial f}{\partial t} + \boldsymbol{\xi} \cdot \frac{\partial f}{\partial \boldsymbol{x}} + \frac{\boldsymbol{F}}{m} \cdot \frac{\partial f}{\partial \boldsymbol{\xi}} = \Omega, \tag{4.2a}$$

where $\boldsymbol{F}$ is the self-consistent force field generated by the soft attractive potential tail,

$$\boldsymbol{F}(\boldsymbol{x}, t) = \int_{||\boldsymbol{x}_1 - \boldsymbol{x}|| > \sigma} \frac{d\phi}{dr} \frac{\boldsymbol{x}_1 - \boldsymbol{x}}{||\boldsymbol{x}_1 - \boldsymbol{x}||} n(\boldsymbol{x}_1, t) d\boldsymbol{x}_1, \tag{4.2b}$$

and Ω is the hard-sphere collision integral derived within Enskog theory,

$$\Omega = \sigma^2 \int \left\{ \chi\left(\boldsymbol{x} + \frac{\sigma}{2}\boldsymbol{k}\right) f^{'}(\boldsymbol{x}) f_1^{'}(\boldsymbol{x} + \sigma\boldsymbol{k}) - \chi\left(\boldsymbol{x} - \frac{\sigma}{2}\boldsymbol{k}\right) f(\boldsymbol{x}) f_1(\boldsymbol{x} - \sigma\boldsymbol{k}) \right\} \boldsymbol{g} \cdot \boldsymbol{k} d\boldsymbol{k} d\boldsymbol{\xi}_1. \tag{4.2c}$$

Here, $\boldsymbol{g} = \boldsymbol{\xi}_1 - \boldsymbol{\xi}$ is the relative velocity of two collision molecules, and $\boldsymbol{k}$ is the unit vector, which is related to the relative position of the collision molecules. In terms of the distribution functions in Enskog collision term, $f^{'}(\boldsymbol{x}) = f(\boldsymbol{x}, \boldsymbol{\xi}^{'}, t)$, $f_1^{'}(\boldsymbol{x}) = f(\boldsymbol{x}, \boldsymbol{\xi}_1^{'}, t)$, $f(\boldsymbol{x}) = f(\boldsymbol{x}, \boldsymbol{\xi}, t)$, $f_1(\boldsymbol{x}) = f(\boldsymbol{x}, \boldsymbol{\xi}_1, t)$, where the relations between pre-collision molecular velocities $\boldsymbol{\xi}^{'}$ and $\boldsymbol{\xi}_1^{'}$ and post-collision molecular velocities $\boldsymbol{\xi}$ and $\boldsymbol{\xi}_1$ are $\boldsymbol{\xi}^{'} = \boldsymbol{\xi} + (\boldsymbol{g} \cdot \boldsymbol{k})\boldsymbol{k}$ and $\boldsymbol{\xi}_1^{'} = \boldsymbol{\xi}_1 - (\boldsymbol{g} \cdot \boldsymbol{k})\boldsymbol{k}$. Following the standard Enskog theory (SET), χ in Eq. 4.2c is the pair correlation function of a hard-sphere fluid in equilibrium valued at the contact point, which accounts for correlations between colliding particles. The pair correlation function is related to the local density $\rho(\boldsymbol{x}, t)$ and can be obtained from the Carnahan–Starling equation of state for hard-sphere fluids (Carnahan & Starling, 1969)

$$\chi(\rho) = \frac{1 - 0.125 b\rho}{(1 - 0.25 b\rho)^3}, \tag{4.3}$$

where $b = 2\pi\sigma^3/3m$, which is related to the reduced density $\eta = b\rho/4$.

Despite its ability to provide accurate results for dense gases, the EV equation suffers from high computational cost, limiting its practical application in engineering. To overcome this limitation, we have introduced a simplified Enskog collision term by approximating the non-local terms with a first-order Taylor series expansion truncated after the first derivative terms in the molecular diameter. The zero-order terms are then replaced by the Shakhov model to correctly represent the Prandtl number (Pr), and the first-order derivatives are evaluated by replacing the distribution function with a Maxwellian distribution, while a term involving the second derivative of the velocity is to recover the correct bulk viscosity (Su et al., 2023; P. Wang et al., 2020). For dense gases and liquids, the molecular distribution is typically close to the Maxwellian, making such a velocity distribution effective for capturing denseness effects. The resulting simplified Enskog collision term can be expressed mathematically as

$$\Omega = J_S + J_e, \tag{4.4a}$$

where the Shakhov model-like part J_S is

$$J_S = \frac{f^{eq} - f}{\tau} + \frac{f^{eq}}{\tau} \frac{2m(1 - Pr)\boldsymbol{q}^K \cdot \boldsymbol{C}}{5n(k_B T)^2} \left(\frac{mC^2}{2k_B T} - \frac{5}{2} \right), \tag{4.4b}$$

and the excess part J_e is

$$J_e = -\rho b\chi f^{eq}\left\{\boldsymbol{C}\cdot\left[\frac{2}{n}\frac{\partial n}{\partial \boldsymbol{x}}+\frac{1}{T}\frac{\partial T}{\partial \boldsymbol{x}}\left(\frac{3mC^2}{10k_BT}-\frac{1}{2}\right)\right]+\frac{2m}{5k_BT}\boldsymbol{CC}:\frac{\partial}{\partial \boldsymbol{x}}\boldsymbol{u}\right.$$
$$\left.-\left(1-\frac{mC^2}{5k_BT}\right)\left(\frac{\partial}{\partial \boldsymbol{x}}\cdot\boldsymbol{u}\right)\right\}-\rho b\boldsymbol{C}f^{eq}\cdot\frac{\partial\chi}{\partial \boldsymbol{x}}+\frac{\partial}{\partial \boldsymbol{x}}\cdot\left[f^{eq}\frac{\varpi}{nk_BT}\left(\frac{\partial}{\partial \boldsymbol{x}}\cdot\boldsymbol{u}\right)\boldsymbol{C}\left(\frac{mC^2}{2k_BT}-\frac{3}{2}\right)\right]. \tag{4.4c}$$

Here, ϖ is the bulk viscosity, f^{eq} is the local Maxwellian distribution function

$$f^{eq} = n\left(\frac{m}{2\pi k_BT}\right)^{3/2}\exp\left(-\frac{mC^2}{2k_BT}\right), \tag{4.5}$$

and n is the number density, T is the temperature, $\boldsymbol{u}$ is the bulk velocity, $\boldsymbol{q}^K$ is the kinetic contribution to the heat flux (see also the Appendix B). These macroscopic quantities are determined by the velocity moments:

$$\begin{aligned} n(\boldsymbol{x},t) &= \int f(\boldsymbol{x},\boldsymbol{\xi},t)d\boldsymbol{\xi},\\ \boldsymbol{u}(\boldsymbol{x},t) &= \frac{1}{n}\int \boldsymbol{\xi} f(\boldsymbol{x},\boldsymbol{\xi},t)d\boldsymbol{\xi},\\ T(\boldsymbol{x},t) &= \frac{1}{2nc_v}\int C^2 f(\boldsymbol{x},\boldsymbol{\xi},t)d\boldsymbol{\xi},\\ \boldsymbol{q}^K(\boldsymbol{x},t) &= \frac{m}{2}\int \boldsymbol{C}C^2 f(\boldsymbol{x},\boldsymbol{\xi},t)d\boldsymbol{\xi}, \end{aligned} \tag{4.6}$$

where $c_v = 3k_B/2m$ is the specific heat capacity at constant volume, k_B is the Boltzmann constant and $\boldsymbol{C} = \boldsymbol{\xi} - \boldsymbol{u}$ is the peculiar velocity. The relaxation time $\tau = \mu/nk_BT$ is calculated based on the shear viscosity of dense gas μ

$$\mu = \frac{\mu^*}{\chi}\left(1+\frac{2}{5}\rho b\chi\right)^2+\frac{3}{5}\varpi, \tag{4.7}$$

where μ^* is the gas shear viscosity at reference temperature and the bulk viscosity $\varpi = \mu^*\chi(\rho b)^2$. The thermal conductivity κ for dense gas can be calculated as

$$\kappa = \frac{\kappa^*}{\chi}\left(1+\frac{3}{5}\rho b\chi\right)^2+c_v\varpi, \tag{4.8}$$

where κ^* is the thermal conductivity at reference pressure. Thus, the Prandtl number is calculated as

$$Pr = \frac{2}{3}\frac{(1+\frac{2}{5}\rho b\chi)^2+\frac{3}{5}(\rho b\chi)^2}{(1+\frac{3}{5}\rho b\chi)^2+\frac{2}{5}(\rho b\chi)^2}. \tag{4.9}$$

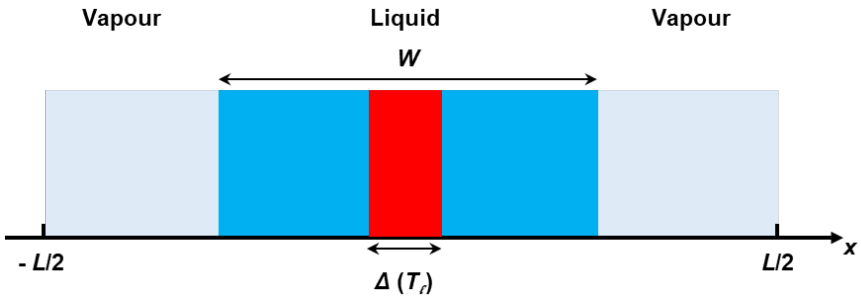

Figure 4.2: Simulation setup: A slab of liquid of width W is placed in the centre of the computational domain, surrounded by vapour. The central part of the liquid Δ (red area) is thermostatted at a fixed temperature T_ℓ.

It is worth noting that the equation of state of the fluid described by the Sutherland potential includes not only the kinetic contribution but also the collisional contribution and the influence of the force field, resulting in a generalized van der Waals form (Frezzotti et al., 2005a),

$$p = nk_BT(1+nb\chi) - \frac{2\pi\sigma^3}{3}\frac{\gamma}{\gamma-3}\phi_\sigma n^2. \tag{4.10}$$

As expected, when $b \to 0$, the shear viscosity, thermal conductivity, and Prandtl number approach the values observed in dilute hard-sphere monatomic gases, i.e. $\chi \to 1$ and $\varpi \to 0$. The detailed derivation of the kinetic model and the method for correcting the transport properties to represent real fluids can be found in our previous publications (Su et al., 2023; P. Wang et al., 2020), with the latter specifically described in B. Shan et al. (2023).

4.2.2 Simulation Setup

As depicted in Figure 4.2, the simulation setup consists of a liquid slab of width W occupying the central region of the computational domain $[-L/2, L/2]$, surrounded by the vapour phase. The liquid slab is thermostated throughout the simulations in the slab centre Δ by setting the distribution function to be a Maxwellian with the local density but fixed temperature T_ℓ.

The kinetic model is assessed by examining three simulation test cases: (a) liquid-vapour equilibrium, (b) evaporation into near vacuum, and (c) evaporation into vapour. Different boundary conditions are used in each case. Specifically:

(a) Periodic boundary conditions are applied to allow the system to reach equilibrium, where particles leaving from one side of the domain re-enter from the opposite side. This ensures mass conservation and mimics an infinite repeating system, allowing particles to circulate without loss.

$$f\left(\mp\frac{L}{2}, \xi_x\right) = f\left(\pm\frac{L}{2}, \xi_x\right), \qquad \xi_x \gtrless 0. \tag{4.11}$$

(b) Absorbing wall boundary conditions are applied to simulate a near-vacuum environment surrounding the domain. Particles that strike the boundary are not reflected but are instead deleted from the system, modelling an open domain.

$$f\left(\mp\frac{L}{2},\xi_x\right)=0, \qquad \xi_x \gtrless 0. \tag{4.12}$$

(c) Far-field boundary conditions are applied to represent the vapour region at a distance, where the distribution is a drifting Maxwellian with velocity u_∞ to mimic steady evaporation (Frezzotti, 2011).

$$f\left(\mp\frac{L}{2},\xi_x\right)=n_\infty\left(\frac{m}{2\pi k_B T_\infty}\right)^{3/2}\exp\left(-\frac{m(\xi_x-u_\infty)^2}{2k_B T_\infty}\right), \qquad \xi_x \gtrless 0. \tag{4.13}$$

In all these cases, the quantities of interest vary only along the x direction, so the analysis is simplified by introducing reduced distribution functions, which are obtained by integrating the full distribution function over the ξ_y and ξ_z velocity components (P. Wang et al., 2020). The resulting coupled system of two reduced distribution equations has been made dimensionless using the molecular diameter as the reference length ℓ_0 and the most probable molecular velocity at the reference temperature T_0 as the reference velocity $u_0=\sqrt{2k_BT_0/m}$. The corresponding reference time is then defined as $t_0=\ell_0/u_0$, the reference mean force field as u_0^2/ℓ_0, the reference distribution function as $f_0=n_0/u_0^3$ and the reference number density as $n_0=1/\ell_0^3$. The equations were solved using the Discrete Velocity Method (DVM), which discretizes the velocity space into a finite number of grid points and evaluates the distribution function at these discrete velocities (P. Wang et al., 2020). Uniform meshes are employed in both the spatial and velocity domains. Spatial and velocity derivatives are approximated using second-order central finite differences, while temporal integration is performed using an explicit Euler scheme. Consequently, the numerical scheme is second-order accurate in space and first-order accurate in time. Mesh independence studies were conducted to verify convergence with respect to both spatial and velocity discretisations. Since the mean-field force is a key quantity governing phase transition behaviour, we evaluated its relative error under different spatial and velocity mesh resolutions. The results showed decreasing differences with mesh refinement, indicating convergence. To ensure the efficiency and accuracy, the spatial domain was discretised with a grid size of $\ell_0/10$ and the velocity domain was discretised with a grid size of $u_0/20$ over the range $[-4u_0,4u_0]$ for all simulations.

This method uses uniform meshes in both spatial and velocity space, with derivatives approximated by second-order finite differences in both domains, while time integration uses an explicit Euler scheme. As a result, the scheme is second-order accurate in space and first-order accurate in time. After conducting mesh independence studies, the spatial domain was discretised with a grid size of $\ell_0/10$ and the velocity domain was discretised with a grid size of $u_0/20$ over the range $[-4u_0,4u_0]$ for all simulations.

From here on, a tilde will be used to distinguish dimensionless quantities from dimensional ones.

4.3 Results and Discussion

4.3.1 Liquid-Vapour Equilibrium

In this section, we determine the equilibrium solution for a liquid coexisting with its vapour at constant temperature. The main aim is to assess the ability of our kinetic model to capture the structure of the liquid-vapour interface.

The computational domain was set to $L = 60\sigma$, with the liquid phase confined within a slab of width $W = 30\sigma$ and the system fully thermostatted, i.e., $\Delta = L$. For the first simulation, the system temperature $\tilde{T}$ was kept constant at 0.65, the number densities of the liquid and vapour phases were set higher and lower than the theoretical equilibrium values, respectively, and the system was then allowed to evolve to a steady state. The theoretical equilibrium values of the density in the liquid and vapour bulks follow from the mechanical and chemical equilibrium conditions, which require the pressure and chemical potential of the two bulk phases to be equal at the given temperature. When using the Sutherland potential, the chemical potential ε and the pressure p have two contributions - one from the hard-sphere potential (Heyes & Santos, 2016) and the other from the soft attractive potential tail (Karkheck & Stell, 1981) - and the resulting expressions are (Frezzotti, Gibelli, Lockerby, & Sprittles, 2018):

$$\varepsilon = k_B T \left[\eta \frac{8 - 9\eta + 3\eta^2}{(1-\eta)^3} + \ln(\eta) \right] - 8\phi_\sigma \eta \frac{\gamma}{\gamma - 3}, \tag{4.14a}$$

$$p = \frac{6}{\pi} \eta \frac{1 + \eta + \eta^2 - \eta^3}{(1-\eta)^3} k_B T - \frac{24}{\pi \sigma^3} \phi_\sigma \eta^2 \frac{\gamma}{\gamma - 3}. \tag{4.14b}$$

The resulting number density profiles are shown in Figure 4.3(a) with both phases reaching their respective theoretical equilibrium number densities as indicated by the dotted lines.

A further insight into the relaxation dynamics can be gained by observing that in equilibrium, the gradient of the kinetic and collisional contributions to the xx-component of the stress tensor must balance the self-consistent force field (Frezzotti & Gibelli, 2003). The derivations of the kinetic and collisional contributions to the stress tensor and the heat flux, are given in the Appendix B. As shown in Figure 4.3(b), there is initially an imbalance between the kinetic and collisional contributions to the stress tensor and the self-consistent force field, causing a flow from the liquid to the vapour phase. This transition leads to a simultaneous decrease in the gradients of these contributions and of the force field, but the latter experiences a comparatively smaller decrease. As a result, an equilibrium is eventually reached.

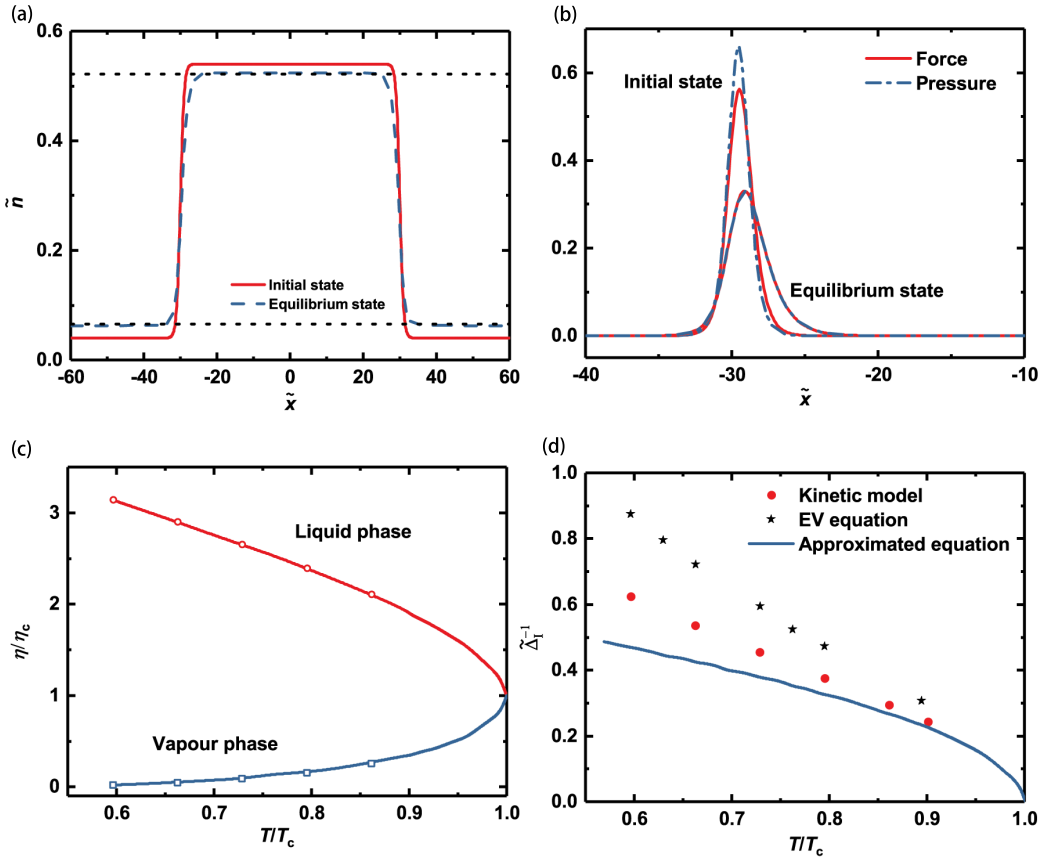

Figure 4.3: (a) Number density profile in the initial and equilibrium states, where the two dotted lines represent the theoretical equilibrium number densities in the liquid and vapour bulk at $\tilde{T} = 0.65$. (b) Force balance between the gradient of the kinetic and collisional contributions to the xx component of the stress tensor and the self-consistent force field. (c) Liquid-vapour coexistence curve, where the points are obtained from the numerical simulation, and the lines are theoretical predictions. (d) Reciprocal liquid-vapour interface thickness as a function of system temperature.

Numerical simulations similar to those discussed above were carried out at different temperatures to map the phase coexistence curve, as shown in Figure 4.3(c). Here, the number density and temperature are normalised by the critical reduced number density η_c and critical temperature T_c, respectively, which are given by (Frezzotti et al., 2005a)

$$\eta_c = \frac{\pi\sigma^3 n_c}{6} \approx 0.13, \quad T_c = 0.094\frac{4\gamma}{\gamma - 3}\frac{\phi_\sigma}{k_B}. \tag{4.15}$$

It is clear that our kinetic model accurately captures the equilibrium liquid and vapour densities across the coexistence curve, with results in perfect agreement with the theoretical values from Eq. 4.14.

The interface thickness Δ_I is also calculated for different system temperatures by fitting the equilibrium density profile to a hyperbolic tangent profile, which has been shown to accurately capture the interface structure (Frezzotti & Gibelli, 2003),

$$n(x) = n_v + \frac{n_\ell - n_v}{2}\left[1 + \tanh\left(2\frac{x - x_\ell}{\Delta_I}\right)\right], \tag{4.16}$$

where x_ℓ is the center of the liquid-vapout interface, and the subscripts v, ℓ represent the vapour and liquid bulk, respectively. The results from our kinetic model are compared in Figure 4.3(d) with those from the EV equation and a simplified equilibrium density profile equation derived from the Taylor expansion of the integral equation for the equilibrium density profile (Frezzotti et al., 2005a). While our model slightly overestimates the interfacial thickness compared to the EV equation, especially at lower temperatures, it successfully captures the qualitative trend of thickness variation with temperature. This quantitative discrepancy is to be expected, given the simplifications introduced by the approximate collision integral of our model.

4.3.2 Evaporation into Near-Vacuum

In this section, we study the evaporation of a liquid under near vacuum condition. The main aim is to estimate the evaporation coefficient using the simulation results of our kinetic model. This coefficient is a key parameter in the formulation of boundary conditions at the liquid-vapour interface required for kinetic theory modelling of vapour dynamics.

The computational domain was set to $L = 30\sigma$, with the liquid phase confined within a slab of width $W = 17\sigma$, the vapour region being deliberately kept thin to enforce the free molecular flow of the vapour (Frezzotti et al., 2005a). The thermostated region was set to $\Delta = 4\sigma$. For better illustration and comparison across different cases, a special treatment is employed to achieve a steady state of evaporation: the mass of outgoing particles is continuously monitored, and an equivalent amount is reintroduced into the thermostated region once it reaches the mass corresponding to the liquid-phase density within one computational cell. When the total mass removed and added becomes balanced over a sampling time interval, the system reaches a steady state in which the interface remains nearly stationary at its original position.

Figures 4.4(a) and (b) show the number density and temperature profiles for different liquid bulk temperatures as given by our kinetic model. For better comparison, the temperature range used in the simulated cases is the same as that in the full Enskog–Vlasov equation. In contrast to the equilibrium solution, the number density profile has a concave shape in the central region, which becomes more pronounced as T_ℓ increases. Correspondingly, the temperature is no longer uniform throughout the system, but a temperature gradient emerges from the centre towards the boundaries, with the steepest gradient occurring in the interface

region. The kinetic and collisional contributions to the heat flux and stress tensor across the system for different liquid bulk temperatures are shown in Figures 4.4(c) and (d). The heat flux is proportional to the temperature gradient and the thermal conductivity, which varies with the number density. As a result, the heat flux increases in the liquid phase, while it drops to a very small value in the vapour phase. By contrast, the behaviour of the stress tensor closely follows the variations of the number density. A detailed comparison of the macroscopic quantities, including number density, total temperature, transversal temperature $T_\perp$, longitudinal temperature $T_\parallel$, mean force field and bulk velocity, is shown in Figure 4.4(e) between the results of our kinetic model and the EV equation (Frezzotti et al., 2005a). Here, the transversal and longitudinal temperatures are defined as

$$T_\perp = \frac{k}{2nm}\int (\xi_y^2 + \xi_z^2) f(\boldsymbol{x}, \boldsymbol{\xi}, t) \mathrm{d}\boldsymbol{\xi}, \tag{4.17a}$$

$$T_\parallel = \frac{k}{nm}\int (u_x - \xi_x)^2 f(\boldsymbol{x}, \boldsymbol{\xi}, t) \mathrm{d}\boldsymbol{\xi}, \tag{4.17b}$$

being the total temperature given by $T = (T_\parallel + 2T_\perp)/3$. As shown in Figure 4.4(e), our kinetic model has an accuracy in predicting macroscopic flow properties comparable to the EV equation.

In this simulation setup, the evaporation coefficient σ_e can be calculated using the equation

$$\sigma_e n_g(T_e)\sqrt{\frac{RT_e}{2\pi}} = J_m, \tag{4.18}$$

where T_e is the temperature attributed to the liquid-vapour interface, and J_m is the outgoing mass flux that can be numerically evaluated at the boundary of the computational domain (Frezzotti et al., 2005a). The temperature T_e in Eq. 4.18 requires careful consideration, with two standard choices being the liquid bulk temperature T_ℓ and the separation temperature T_s, defined as the temperature at the point where the transversal and longitudinal temperatures separate, marking the beginning of the non-equilibrium region on the vapour side. The bulk temperature T_ℓ is often used in kinetic theory studies because it is a known parameter whereas the separation temperature T_s is not known a priori and must therefore be estimated (Frezzotti et al., 2019, 2005a).

The results for the evaporation coefficient are shown in Figure 4.4(f). When $T_e = T_\ell$, σ_e decreases as T_ℓ increases, while when $T_e = T_s$, σ_e has less variation, with the value remaining around 0.8. Although our model is in qualitative agreement with the EV equation in terms of macroscopic properties such as the temperature and density fields, it underestimates the evaporation coefficient over the temperature range studied. If $T_e = T_s$ is chosen, the difference to the EV equation, decreasing with increasing temperature, is about 15% for $T_\ell = 0.45$ and about 7% for $T_\ell = 0.55$. Additionally, the different choices of temperature in Eq. 4.18 can

lead to a significant discrepancy in the evaporation coefficient. And this discrepancy is small for weak evaporation and diminishes when the temperature gradient along the liquid phase becomes zero. Consequently, when the evaporation coefficient is used as an input parameter in kinetic or macroscopic simulations for strong evaporation, appropriate choice of liquid-vapour interface temperature is a daunting task which will inevitably lead to errors in predicting the macroscopic properties in the dilute phase.

4.3.3 Evaporation into Vapour

In this section, we study the evaporation of a liquid into its vapour. The main aim is to assess the ability of our kinetic model to capture the structure of the Knudsen layer, and in particular the jumps suffered by macroscopic quantities across this region.

Previous studies have accurately described the Knudsen layer structure in planar evaporation by solving the one-dimensional Boltzmann equation with a moment method (Labuntsov & Kryukov, 1979; Ytrehus, 1997). Assuming an evaporation condensation coefficient of unity, $\sigma_e = 1$, these studies determined the jumps in temperature and number density across the Knudsen layer as

$$\left(\frac{T_\infty}{T_s}\right)^{1/2}_{\sigma_e=1} = -\pi^{1/2}\frac{S_\infty}{8} + \left[1+\pi\left(\frac{S_\infty}{8}\right)^2\right]^{1/2}, \tag{4.19a}$$

$$\left(\frac{n_{sv}}{n_\infty}\right)_{\sigma_e=1} = \frac{2\exp(-S_\infty^2)\frac{T_\infty}{T_s}}{F^- + \left(\frac{T_\infty}{T_s}\right)^{1/2} G^-}, \tag{4.19b}$$

where $S_\infty = u_\infty(2RT_\infty)^{-1/2}$ is the dimensionless evaporation velocity, n_{sv} is the saturated vapour number density under T_s, and F^- and G^- are functions of S_∞ given by

$$F^- = -\pi^{1/2} S_\infty \mathrm{erfc}(S_\infty) + \exp(-S_\infty^2), \tag{4.20a}$$

$$G^- = (2S_\infty^2+1)\mathrm{erfc}(S_\infty) - \frac{2S_\infty}{\pi^{1/2}}\exp(-S_\infty^2), \tag{4.20b}$$

being $\mathrm{erfc}(S_\infty)$ the complementary error function,

$$\mathrm{erfc}(S_\infty) = 1 - \mathrm{erf}(S_\infty) = 2\pi^{-1/2}\int_{S_\infty}^{\infty} e^{-t^2} dt. \tag{4.21}$$

If the evaporation coefficient is different from unity, $\sigma_e \neq 1$, the temperature jump remains the same, while the jump in the number density changes to

$$\left(\frac{n_{sv}}{n_\infty}\right)_{\sigma_e\neq 1} = \left(\frac{n_{sv}}{n_\infty}\right)_{\sigma_e=1} + \frac{1-\sigma_e}{\sigma_e} 2\pi^{1/2}\left(\frac{T_\infty}{T_s}\right)^{1/2} S_\infty. \tag{4.22}$$

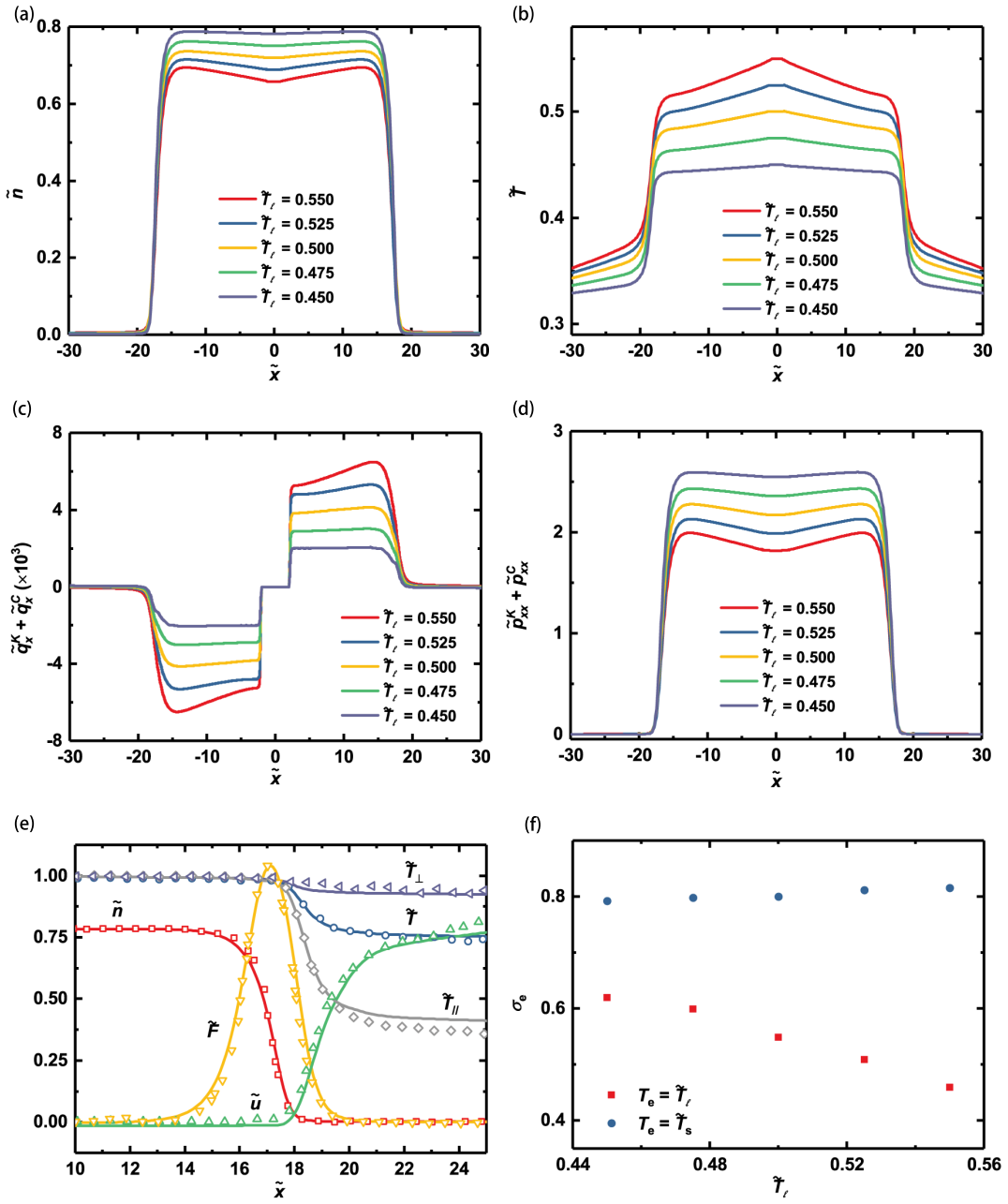

Figure 4.4: (a) Number density, (b) temperature and sum of kinetic and collisional contributions to (c) the heat flux and (d) the stress tensor under different $\tilde{T}_\ell$. (e) Comparison of macroscopic quantities between the present kinetic model and EV equation (Frezzotti et al., 2005a) at $\tilde{T}_\ell = 0.45$. The solid line indicates the results obtained from the present kinetic model, while the hollow points depict the results obtained from the EV equation. (f) Evaporation coefficients under different $\tilde{T}_\ell$. Here, two reference temperatures are adopted.

Simulations were performed here for different far-field velocities u_∞ and by varying L accordingly in the range $L = [400\sigma, 1200\sigma]$ to resolve the structure of the Knudsen layer accurately. In fact, the thickness of the Knudsen layer varies from several molecular diameters for very weak evaporation to about $20\lambda_e$, where $\lambda_e = 1/\sqrt{2}\pi n_{sv}\sigma^2$, which corresponds to about 600σ as the far-field velocity approaches the transonic value (Frezzotti et al., 2019; Sibold & Urbassek, 1993; Ytrehus, 1997). The computational cost of these simulations was reduced by examining only half of the domain, i.e. $[0, L/2]$, assuming specular boundary conditions at $x = 0$ and a self-consistent zero force enforced near this boundary. The liquid phase was confined within a slab of width $W = 60\sigma$, and the thermostated region was set to $\Delta = 4\sigma$.

The variation of density, velocity and temperature across the Knudsen layer at $\tilde{T}_\ell = 0.5$ is shown for different evaporation velocities, i.e. $\tilde{u}_\infty = 0.2$ in Figure 4.5(a) and $\tilde{u}_\infty = 0.3$ in Figure 4.5(b). These results are compared with those obtained from DSMC simulations. It should be emphasised that our kinetic model, like the EV equation, provides the solution for both the liquid and vapour phases, including the interfacial region. In contrast, the DSMC simulations only simulate the vapour behaviour and therefore require boundary conditions at the liquid-vapour interface. In the comparison, we assumed that the vapour region begins at the point where the parallel and transverse temperatures separate. Accordingly, at the liquid-vapour interface, we prescribed a Maxwellian boundary condition with a temperature given by the separation temperature, a density given by the saturation density at the separation temperature, and an evaporation coefficient as calculated by our model in the vacuum evaporation studies. In the far field, the DSMC simulations assume the same boundary condition Eq. 4.13 of the kinetic model. A more detailed description of the simulation setup for the DSMC simulations can be found in our previous work (Frezzotti, 2007, 2011).

As Figures 4.5(a) and (b) clearly show, the results obtained by the two methods are in good agreement, although the kinetic model predicts a slightly larger decrease in density and a smaller decrease in temperature. This can be seen more clearly in Figure 4.5(c), where the jump relations of density and temperature computed numerically over a wide range of temperatures are compared with the DSMC predictions and the analytical solutions obtained from Eq. 4.19a and Eq. 4.22.

4.4 Conclusions

A kinetic model has been developed to efficiently simulate liquid-vapour flows. The model approximates particle interactions using a Sutherland potential, which combines a hard-sphere repulsive potential and a soft-attractive potential tail. The repulsive interactions are represented by an approximated collision integral obtained by expanding the Enskog collision integral

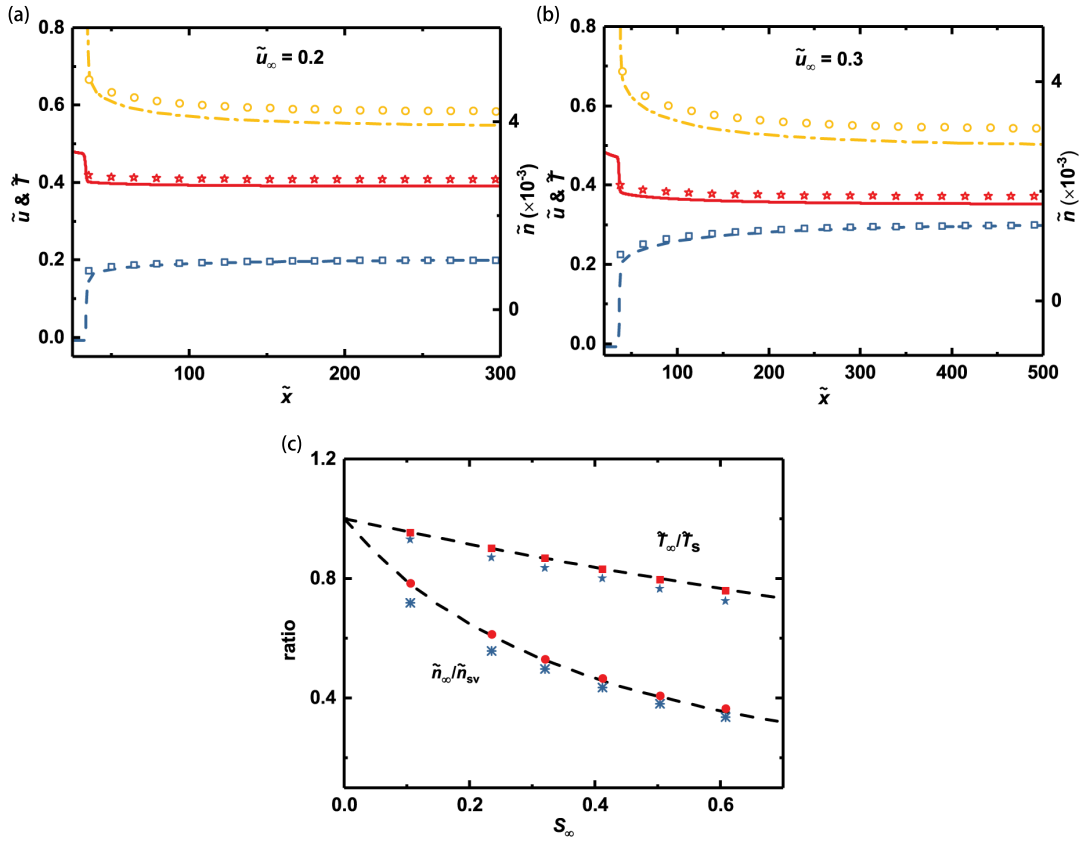

Figure 4.5: Number density, temperature, and velocity profiles across the Knudsen layer for two evaporation velocities: (a) $\tilde{u}_\infty = 0.2$ and (b) $\tilde{u}_\infty = 0.3$. Lines represent kinetic model results; symbols show DSMC simulation results. The colours indicate different macroscopic quantities: yellow, number density $\tilde{n}$; blue, velocity $\tilde{u}$; red, temperature $\tilde{T}$. (c) Jump relations across the Knudsen layer. The analytical solution is the dashed line. Blue symbols are kinetic model results; red symbols are DSMC simulations.

in Taylor series, approximating the zero-order term by a Shahkov-like relaxation term and the higher order terms by assuming that the distribution function is local Maxwellian. The attractive interactions are modelled using a mean-field approximation so that the particles experience a self-consistent force field generated by their interactions.

This approximate kinetic model has been validated by comparison with analytical solutions and with numerical solutions of the EV equation for equilibrium and nonequilibrium evaporation scenarios. Excellent agreement was obtained, especially at higher temperatures. At lower temperatures, some deviations were observed, but the model still adequately captured the essential physics. Most importantly, the kinetic model presented here significantly reduces the computational cost by almost two orders of magnitude compared to solving the EV equation for the one-dimensional problems discussed. It is expected that the computational gain decreases for higher dimensional problems due to the increased effort required to compute the

self-consistent force field. However, in such scenarios, significant reductions in computational time can still be achieved by using adaptive grids instead of simple uniform grids and/or by implementing standard parallelization strategies based on domain decomposition, which can be implemented easily and efficiently.

The favourable trade-off between accuracy and performance suggests that our approximate kinetic model can become a valuable asset for the efficient simulation of liquid-vapor flows. To further its applicability, our future research will focus on two main directions. First, we aim to extend it to higher physical dimensions, allowing the consideration of more complicated fluid dynamics scenarios such as droplet coalescence and capillary waves. Secondly, we aim to formulate boundary conditions to emulate solid walls, thus addressing the challenge of capturing non-local, non-instantaneous effects on the liquid wall scattering dynamics that are crucial at the nanoscale. This will facilitate the study of fluid wetting properties and contact line motion. Together, these advances will enhance the effectiveness of our kinetic model as a useful engineering tool.

Chapter 5

Simplified Kinetic Modelling of Two-Dimensional Liquid-Vapour Flows: Droplet Ripening

N.B. This chapter is being prepared as a manuscript for a journal paper: Li, S., Li, Z., Gibelli, L., Zhang, Y. 'Kinetic modelling of droplet ripening in two-dimensional liquid-vapour system'

Droplet ripening, a near-equilibrium phenomenon in which large droplets grow at the expense of smaller ones, remains poorly understood at the micro- or nanoscale, where interfacial-bulk interactions dominate. This knowledge gap hinders progress in the understanding of many natural phenomena and in the development of several technological applications that rely on this process, ranging from cloud formation to nanomaterial synthesis. In this work, we study droplet ripening at the nanoscale in a two-dimensional one-component liquid-vapour system using a simplified kinetic model that balances accuracy and computational efficiency. Our results confirm that the driving force of the process is the pressure difference between the vapour region and the droplets. Importantly, we find that the rate of change of droplet size is linear with the Laplace pressure if the droplets have a bulk region, otherwise non-linear effects come into play. Furthermore, the slope of this linear relationship increases exponentially with increasing temperature, regardless of droplet number and arrangement. Future work should focus on extending this model to three-dimensional systems and investigating the effects of surface properties on the ripening process.

5.1 Literature Survey

In a metastable system quenched from above its critical temperature, phase separation occurs, with the dense phase nucleating and growing into droplets of different sizes. Following this initial phase separation, the system undergoes a coarsening process in which larger droplets grow at the expense of smaller droplets, which evaporate and dissolve, eventually forming a single large droplet (Bray, 1994; Voorhees, 1985, 1992; Yao, Elder, Guo, & Grant,

1993). This coarsening process occurs through two mechanisms. The first is collisional, where droplets grow by collision and subsequent coalescence (A. J. Wagner & Cates, 2001). The second is collisionless, also known as Ostwald ripening (Kraska, 2008; Onuki, 2002), where large droplets grow at the expense of smaller ones. In Ostwald ripening, mass transfer occurs without liquid bridge formation and is driven by a concentration gradient in the low density phase. This fundamental diffusive mass transfer process has far-reaching implications in various fields of science and engineering. Its applications range from the crystallisation of biological molecules (Ng et al., 1996) to oil-water separation (Ariyaprakai & Dungan, 2010) and nanomaterial synthesis (Yec & Zeng, 2014). Improving our understanding of Ostwald ripening is therefore crucial to progress in these diverse areas.

The first quantitative approach to predicting the Ostwald ripening process was proposed independently by Lifshitz and Slyozov (1961) and by C. Wagner (1961). Their work, known as LSW theory, was originally developed for binary fluids in the limit of zero volume fraction of the dispersed phase. However, subsequent research has demonstrated a wider applicability, extending the theory to finite higher volume fractions (Hardy & Voorhees, 1988; Marqusee & Ross, 1984), two-dimensional systems (Fan, Chen, Chen, & Voorhees, 2002) and even combinations of both (Yao et al., 1993), thus covering a wide range of systems and dimensions. These studies have consistently revealed two important features of the ripening process. First, the average droplet radius grows according to a power law with a different growth exponent for the two- and three-dimensional cases. Second, the droplet size distribution as a function of radius, normalised to the mean radius, remains self-similar throughout the growth process.

Ripening extends beyond droplets in fluid mixtures to systems involving bubbles and single component liquid-vapour transitions. On the one hand, bubble ripening follows mechanisms analogous to droplet ripening and extensive research has led to predictions of growth rates under different environmental conditions and system dimensions (X. Chen, Feng, Hu, Du, & Wang, 2022; Chieco & Durian, 2023; Lemlich, 1978; MacPherson & Srolovitz, 2007; Watanabe, Suzuki, Inaoka, & Ito, 2014). On the other hand, in single component systems, pressure gradients rather than concentration gradients drive the ripening process between large and small droplets. Interestingly, the growth rates in liquid-vapour systems are different from those in mixtures, having the same value for both two- and three-dimensional systems in the absence of collision and coalescence (Koch, Desai, & Abraham, 1983; Negro, Gonnella, Lamura, Busuioc, & Sofonea, 2024; Tateno & Tanaka, 2021).

In addition to theoretical studies, the ripening process has been extensively studied using simulations. Continuum models are commonly employed to describe bulk fluid behaviour in phase separation process. For instance, the Lattice Boltzmann Method (LBM) with the Shan-Chen model for multiphase systems has been used for populations composed of many droplets. The evolution of the droplet size distribution and the critical radius have been investigated under various flow conditions (L. Chen, Kang, Mu, He, & Tao, 2014; X. Chen et

al., 2022; Chibbaro et al., 2008; Gong, Yan, & Chen, 2018; Negro et al., 2024; X. Shan & Chen, 1993, 1994). However, as droplets shrink down to the nanoscale, they transition from being dominated by bulk properties to a state where surface effects become increasingly important. These surface effects can be characterized by the Tolman length, a correction term introduced in thermodynamic theories of curved interfaces, which quantifies how surface tension deviates from its planar value due to interface curvature (Tolman, 1949). Its influence becomes significant when droplet radii are on the order of a few nanometers. At this scale, the continuum methods cannot capture this curvature dependence accurately, and a molecular description such as that provided by Molecular Dynamics (MD) is required (Kraska, 2008; Midya & Das, 2017; Roy & Das, 2012). While MD provides valuable insights into the ripening process at the molecular scale, which is essential for a comprehensive understanding of the overall phenomenon and for improving predictive models, it is computationally expensive when considering the details of individual droplets or the entire droplet population (X. Chen et al., 2022; Kraska, 2008).

To bridge the gap between the computational efficiency of continuum models such as LBM and the accurate nanoscale descriptions provided by MD simulations, kinetic models have gained prominence in the study of liquid-vapour systems. The Enskog-Vlasov (EV) kinetic equation has proved particularly valuable in elucidating evaporation processes in a wide range of systems, complementing the insights gained from single-droplet MD simulations. These include simple fluids composed of mono- (Busuioc, Gibelli, Lockerby, & Sprittles, 2020; Frezzotti et al., 2005a; Kon, Kobayashi, & Watanabe, 2014) and polyatomic molecules (Bruno & Frezzotti, 2019; Busuioc & Gibelli, 2020), mixtures (Frezzotti et al., 2018; Kobayashi, Sasaki, Kon, Fujii, & Watanabe, 2017), and the growth rates of nanodroplets or bubbles in metastable vapours or liquids (Busuioc et al., 2023). Recent research has also focused on developing kinetic models that balance the accuracy of EV with reduced computational cost (T. Chen et al., 2023; Takata et al., 2021; Y. Zhang et al., 2020). In line with these advances, we have recently proposed a model that effectively describes evaporation processes, further extending the capabilities of kinetic modelling in this area (S. Li et al., 2024).

In this chapter, we apply our recently developed model (used in Chapter 4) to study the ripening process in a two-dimensional one-component system. Our aim is to investigate the mechanism of droplet ripening, initially focusing on a simple two-droplet system before extending our investigation to a more complex three-droplet configuration. This will allow us to study the evolution of individual droplet sizes while assessing how different factors - such as temperature, droplet number and arrangement - influence the ripening dynamics.

The rest of this chapter is structured as follows. In Section 5.2, we present our kinetic model and the numerical scheme used to solve the model; then in Section 5.3 we study the ripening process in a two-droplet system, clearly demonstrating the driving mechanism and providing a quantitative prediction of the droplet growth rate; In addition, we extend our analysis to multiple droplets, showing that our theoretical predictions and numerical results are not affected by the number and arrangement of droplets. In Section 5.4, we summarize our main findings and comment on their implications.

5.2 Methodology

5.2.1 Kinetic Model

We consider a fluid composed of identical and spherical molecules of mass m and diameter σ, interacting via the Sutherland potential $\phi(r)$, which results from the superposition of the repulsive hard sphere core and an attractive smooth tail, i.e.

$$\phi(r) = \begin{cases} +\infty, & r < \sigma, \\ -\phi_\sigma \left(\frac{r}{\sigma}\right)^{-\gamma_\sigma}, & r \geq \sigma, \end{cases} \tag{5.1}$$

where ϕ_σ and γ_σ are two positive constants related to the depth of the potential well and the extent of the attractive interaction, respectively, and $r = ||\boldsymbol{x}_1 - \boldsymbol{x}||$ is the distance between the interacting atoms at $\boldsymbol{x}_1$ and $\boldsymbol{x}$. The fluid is described statistically using the molecular distribution function $f(\boldsymbol{x}, \boldsymbol{\xi}, t)$, which represents the number of atoms at time t within an elementary volume of the single-particle phase space centered at position $\boldsymbol{x} = (x, y, z)$ and molecular velocity $\boldsymbol{\xi} = (\xi_x, \xi_y, \xi_z)$. A closed-form evolution equation for the distribution function can be derived under the assumption that long-range particle correlations are negligible, while short-range correlations are approximated by Enskog theory for dense gases (Grmela, 1971; Karkheck & Stell, 1981; Sobrino, 1967). The resulting equation, known as the EV equation, is given by:

$$\frac{\partial f}{\partial t} + \boldsymbol{\xi} \cdot \frac{\partial f}{\partial t} + \frac{\boldsymbol{F}}{m} \cdot \frac{\partial f}{\partial \boldsymbol{\xi}} = \Omega, \tag{5.2}$$

where $\boldsymbol{F}$ is the the self-consistent force field generated by the soft attractive potential tail and Ω is the hard-sphere collision integral derived from Enskog theory.

In this work, droplet ripening is studied in a two-dimensional system, so $\boldsymbol{F}$ simplifies to (Barbante et al., 2015),

$$\begin{aligned} \boldsymbol{F}(x, y, t) = \int [(x_1 - x)\boldsymbol{i} + (y_1 - y)\boldsymbol{j}] n(x_1, y_1, t) \\ K(x_1 - x, y_1 - y) dx_1 dy_1, \end{aligned} \tag{5.3}$$

where $\boldsymbol{i}$ and $\boldsymbol{j}$ are the unit vectors along the x and y axes, n is the number density and the kernel K is given by

$$K(x_1-x,y_1-y)=\int_{-\infty}^{+\infty}\frac{1}{r}\frac{\partial\phi(r)}{\partial r}dz, \tag{5.4}$$

with $r=\sqrt{(x_1-x)^2+(y_1-y)^2+z^2}$. Due to the rapid decay of the integrand, the integral is truncated at five molecular diameters, as contributions beyond this distance are negligible.

To improve the computational efficiency of the EV equation, we implement two simplifications in the collision term Ω. The first simplification involves approximating the non-local terms with a first-order Taylor series expansion, keeping only terms up to the first derivative with respect to the molecular diameter; these zero-order terms are represented using the Shakhov model to ensure an accurate representation of the Prandtl number (Pr); in addition, when evaluating the first-order derivatives, we replace the distribution function with a Maxwellian distribution and introduce a term containing the second derivative of the velocity to properly capture the correct bulk viscosity (Su et al., 2023; P. Wang et al., 2020). The second simplification accounts for the fact that droplet ripening is studied in a two-dimensional system, so the full distribution function can be replaced by two reduced molecular distribution functions, $G_1(\boldsymbol{x},\boldsymbol{\xi},t)$ and $G_2(\boldsymbol{x},\boldsymbol{\xi},t)$, to eliminate the dependence of ξ_z. Specifically, these distribution functions are obtained by integrating out ξ_z from the full distribution function:

$$G_1=\int f d\xi_z,\quad G_2=\int \xi_z^2 f d\xi_z. \tag{5.5}$$

After these simplifications, the EV equation is replaced by two equations for the reduced distribution functions, where G_1 and G_2 satisfy

$$\frac{\partial G_1}{\partial t}+\boldsymbol{\xi}\cdot\frac{\partial G_1}{\partial \boldsymbol{x}}+\frac{\boldsymbol{F}}{m}\cdot\frac{\partial G_1}{\partial \boldsymbol{\xi}}=\frac{G_1^{eq}-G_1}{\tau}+S_a^{G_1}+S_b^{G_1}+S_c^{G_1}, \tag{5.6a}$$

$$\frac{\partial G_2}{\partial t}+\boldsymbol{\xi}\cdot\frac{\partial G_2}{\partial \boldsymbol{x}}+\frac{\boldsymbol{F}}{m}\cdot\frac{\partial G_2}{\partial \boldsymbol{\xi}}=\frac{G_2^{eq}-G_2}{\tau}+S_a^{G_2}+S_b^{G_2}+S_c^{G_2}. \tag{5.6b}$$

The terms on right-hand side of Eq. 5.6a read

$$G_1^{eq}=\frac{nm}{2\pi k_BT}\exp\left(-\frac{mC^2}{2k_BT}\right), \tag{5.7a}$$

$$S_a^{G_1}=\frac{G_1^{eq}}{\tau}\frac{2m(1-Pr)\boldsymbol{q}^K\cdot\boldsymbol{C}}{5n(k_BT)^2}\left(\frac{mC^2}{2k_BT}-2\right)+\frac{\partial}{\partial\boldsymbol{x}}\cdot\left[G_1^{eq}\frac{\boldsymbol{\varpi}}{nk_BT}\left(\frac{\partial}{\partial\boldsymbol{x}}\cdot\boldsymbol{u}\right)\boldsymbol{C}\left(\frac{mC^2}{2k_BT}-1\right)\right], \tag{5.7b}$$

$$\begin{aligned}S_b^{G_1}=-\rho b\chi G_1^{eq}\Bigg\{&\boldsymbol{C}\cdot\left[\frac{2}{n}\frac{\partial n}{\partial\boldsymbol{x}}+\frac{1}{T}\frac{\partial T}{\partial\boldsymbol{x}}\left(\frac{3mC^2}{10k_BT}-\frac{1}{5}\right)\right]+\frac{2m}{5k_BT}\boldsymbol{CC}:\frac{\partial}{\partial\boldsymbol{x}}\boldsymbol{u}\\&+\frac{2}{5}\left(\frac{mC^2}{2k_BT}-2\right)\left(\frac{\partial}{\partial\boldsymbol{x}}\cdot\boldsymbol{u}\right)\Bigg\},\end{aligned} \tag{5.7c}$$

$$S_c^{G_1} = -\rho b \boldsymbol{C} G_1^{eq} \cdot \frac{\partial \chi}{\partial \boldsymbol{x}}. \tag{5.7d}$$

Similarity, the terms on right side of Eq. 5.6b read

$$G_2^{eq} = \frac{T}{2} G_1^{eq}, \tag{5.8a}$$

$$S_a^{G_2} = \frac{G_2^{eq}}{\tau} \frac{2m(1-Pr)\boldsymbol{q}^K \cdot \boldsymbol{C}}{5n(k_B T)^2} \left(\frac{mC^2}{2k_B T} - 1 \right) + \frac{\partial}{\partial \boldsymbol{x}} \cdot \left[G_2^{eq} \frac{\boldsymbol{\varpi}}{nk_B T} \left(\frac{\partial}{\partial \boldsymbol{x}} \cdot \boldsymbol{u} \right) \frac{m\boldsymbol{C}C^2}{2k_B T} \right], \tag{5.8b}$$

$$\begin{aligned} S_b^{G_2} = -\rho b \chi G_2^{eq} \Bigg\{ \boldsymbol{C} \cdot \left[\frac{2}{n} \frac{\partial n}{\partial \boldsymbol{x}} + \frac{1}{T} \frac{\partial T}{\partial \boldsymbol{x}} \left(\frac{3mC^2}{10k_B T} + \frac{2}{5} \right) \right] + \frac{2m}{5k_B T} \boldsymbol{C}\boldsymbol{C} : \frac{\partial}{\partial \boldsymbol{x}} \boldsymbol{u} \\ + \frac{2}{5} \left(\frac{mC^2}{2k_B T} - 1 \right) \left(\frac{\partial}{\partial \boldsymbol{x}} \cdot \boldsymbol{u} \right) \Bigg\}, \end{aligned} \tag{5.8c}$$

$$S_c^{G_2} = -\rho b \boldsymbol{C} G_2^{eq} \cdot \frac{\partial \chi}{\partial \boldsymbol{x}}. \tag{5.8d}$$

In the above equations, χ is the pair correlation function of a hard-sphere fluid in equilibrium, evaluated at the contact point, which accounts for spatial correlations between colliding particles. The pair correlation function depends on the local density ρ and is given by (Carnahan & Starling, 1969)

$$\chi(\rho) = \frac{1 - 0.125 b\rho}{(1 - 0.25 b\rho)^3}, \tag{5.9}$$

where $b = 2\pi\sigma^3/3m$ is a parameter related to the reduced density, defined as $\eta = b\rho/4$. Here, $\boldsymbol{u}$ is the bulk velocity, T is the temperature, $\boldsymbol{q}^K$ is the kinetic heat flux. These macroscopic quantities, as well as the kinetic stress tensor $\boldsymbol{p}^K$, are determined by the velocity moments:

$$\begin{aligned} \left[n, \boldsymbol{u}, T, \boldsymbol{q}^K, \boldsymbol{p}^K \right] = \\ \int \left[G_1, \frac{\boldsymbol{\xi} G_1}{n}, \frac{m}{2nc_v} (C^2 G_1 + G_2), \frac{m\boldsymbol{C}}{2} (C^2 G_1 + G_2), m\boldsymbol{C}\boldsymbol{C} G_1 \right] \mathrm{d}\boldsymbol{\xi}, \end{aligned} \tag{5.10}$$

where $c_v = 3k_B/2m$ is the specific heat capacity at constant volume, k_B is the Boltzmann constant and $\boldsymbol{C} = \boldsymbol{\xi} - \boldsymbol{u}$ is the peculiar velocity. The relaxation time $\tau = \mu/nk_B T$ is related to the viscosity of dense gas which is calculated through (Su et al., 2023)

$$\mu = \frac{\mu^*}{\chi} \left(1 + \frac{2}{5} nb\chi \right)^2 + \frac{3}{5} \boldsymbol{\varpi}. \tag{5.11}$$

Similarity, the thermal conductivity of dense gas can be obtained through

$$\kappa = \frac{\kappa^*}{\chi} \left(1 + \frac{3}{5} nb\chi \right)^2 + c_v \boldsymbol{\varpi}. \tag{5.12}$$

In Eq. 5.11 and Eq. 5.12, the $\mu^* = \frac{5}{16}(mk_BT/\pi)^{\frac{1}{2}}/\sigma^2$ and $\kappa^* = \frac{15k_B}{4m}\mu^*$ are the viscosity and thermal conductivity for dilute gas under reference pressure, and $\varpi = \mu^*\chi(nb)^2$ is the bulk viscosity. From the above equations, the Prandtl number Pr for dense gas is calculated through

$$Pr = \frac{5}{2}\frac{k_B}{m}\frac{\mu}{\kappa} = \frac{2}{3}\frac{(1+\frac{2}{5}nb\chi)^2 + \frac{3}{5}(nb\chi)^2}{(1+\frac{3}{5}nb\chi)^2 + \frac{2}{5}(nb\chi)^2}. \tag{5.13}$$

5.2.2 Simulation Setup

The simulations described in the following sections use a rectangular computational domain with periodic boundary conditions containing one or more circular droplets surrounded by vapour. Three cases with different objectives will be studied:

(a) Case 1 - Single droplet: To evaluate the surface tension of the simulated fluid.
(b) Case 2 - Two droplets: To simulate the ripening process in the simplest possible scenario.
(c) Case 3 -Three droplets: To assess whether the conclusions drawn from the two-droplet ripening analysis hold as the number of droplets increases.

All simulations use dimensionless quantities, with the molecular diameter as the reference length ℓ_0, room temperature as the reference temperature T_0, and the most probable molecular velocity at T_0 as the reference velocity $u_0 = \sqrt{2k_BT_0/m}$. Accordingly, the time t is normalised by ℓ_0/u_0, the number density n by $n_0 = 1/\ell_0^3$, the mean force field by u_0^2/ℓ_0 and the distribution function by n_0/u_0^3.

The kinetic model is solved using the Discrete Velocity Method (DVM) (P. Wang et al., 2020), using a uniform mesh for the spatial discretisation, approximating the derivative by second-order finite differences, and Gaussian-Hermite quadrature nodes for the velocity discretisation. An explicit first-order Euler scheme is used for time integration. Based on mesh independence studies, all simulations use a spatial grid size of $\ell_0/9$ and 8 velocity nodes in each direction.

5.3 Results and Discussion

5.3.1 Surface Tension

In this section, we calculate surface tension, a critical parameter in two-phase flow phenomena, using our kinetic model and compare the results with those predicted by the EV equation (to which our model serves as an approximation) and reported in previous studies (Barbante et al., 2015; Busuioc et al., 2023). We determine the surface tension indirectly using the Young-Laplace equation, which relates the pressure difference between liquid and vapour bulks in a two-dimensional system:

$$\Delta p = p_l - p_v = \frac{\gamma}{R}, \tag{5.14}$$

where γ is the surface tension, R is the droplet radius and the subscripts l and v denote the liquid and vapour phases respectively.

To determine the bulk phase pressure, we first evaluate the density from our simulation results and then use the equation of state for the hard-sphere fluid described by our model,

$$p = nT\frac{1+\eta+\eta^2-\eta^3}{(1-\eta)^3} - \frac{2\pi}{3}\frac{\gamma_\sigma}{\gamma_\sigma-3}\phi_\sigma n^2. \tag{5.15}$$

Under isothermal conditions, the surface tension should remain constant regardless of the droplet radius, as long as it is significantly larger than the Tolman length (Barbante et al., 2015). We will use this property to assess the accuracy of our calculations by calculating the surface tension for droplets of different sizes.

A single droplet with a radius in the range $R \in [6, 12]$ is placed at the centre of a square domain of length $4R$, sufficiently large to mitigate boundary effects, and for three different temperatures of $T = 0.55, 0.6,$ and 0.65. In all cases considered, the bulk region is significantly wider than the interfacial thickness, ensuring that the calculated surface tension is independent of the droplet radius. The initial number densities of the liquid and vapour bulk are set according to the liquid-vapour coexistence curve with a smooth interface following a hyperbolic tangent profile connecting the two regions. The system is then allowed to equilibrate. Figure 5.1 illustrates the relationship between the inverse of the radius and the pressure difference. The constant slope of each fitted line at a given temperature clearly indicates that the surface tension remains constant under fixed temperature conditions, as expected. Table 5.1 summarises our calculated surface tension values alongside results from previous studies. The close agreement between our surface tension measurements and those obtained using the EV equation demonstrates that our model accurately captures this property and suggests its potential for investigating two-phase flow behaviour.

T	Planar	Circular	Spherical	Circular
0.55	0.184	0.178	0.180	0.197
0.6	0.123	0.121	0.118	0.127
0.65	0.0698	0.0675	0.068	0.0695

Table 5.1: Comparison of surface tension values for planar, circular, and spherical interfaces. The results in the first two columns are from Barbante et al. (2015), while the spherical interface results are from Busuioc et al. (2023). The last column presents simulation results from our model in this work.

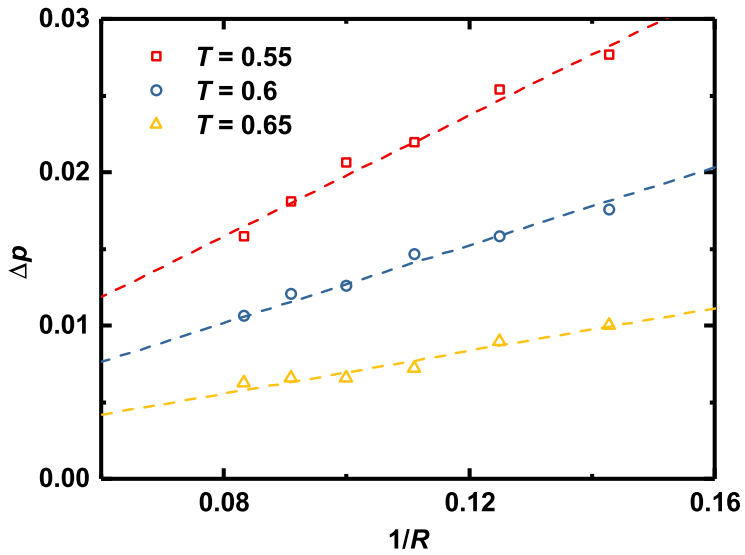

Figure 5.1: Case 1: Relationship between the pressure difference and the reciprocal of the radius. Simulation results at different temperatures are shown as red, blue and yellow points. The best-fit linear line through the origin is also shown.

5.3.2 Ripening in a Two-Droplet System

Qualitative Analysis of the Ripening Mechanism

In this section we describe the evolution of the two-droplet system from initial equilibration to ripening.

The computational setup consists of two droplets of different radii positioned one in front of the other. The centres of the two droplets are located on the centre line of the domain. Due to the periodic boundary conditions, special care must be taken to ensure that the droplets remain stable in their initial positions during the ripening process. Indeed, if asymmetric evaporation were to occur, this would result in a net momentum that would cause the droplets to move. To prevent this, we set the distance between the centres of the droplets to be equal to the sum of the distances from the centre of each droplet to its respective adjacent boundaries.

Figure 5.2 shows the density contour plots with velocity vector fields superimposed at different times for $T = 0.6$. Initially, the liquid-vapour interfaces of the two droplets change rapidly to reach their equilibrium thickness values from the initial arbitrary setting (panel b). Once the transient dynamics subside, the ripening process takes place, as can be seen from the velocity field, which clearly shows the mass transfer from the smaller droplet to the larger one (panels c-e). Note that, during the ripening process, the larger droplet grows at the expense of the

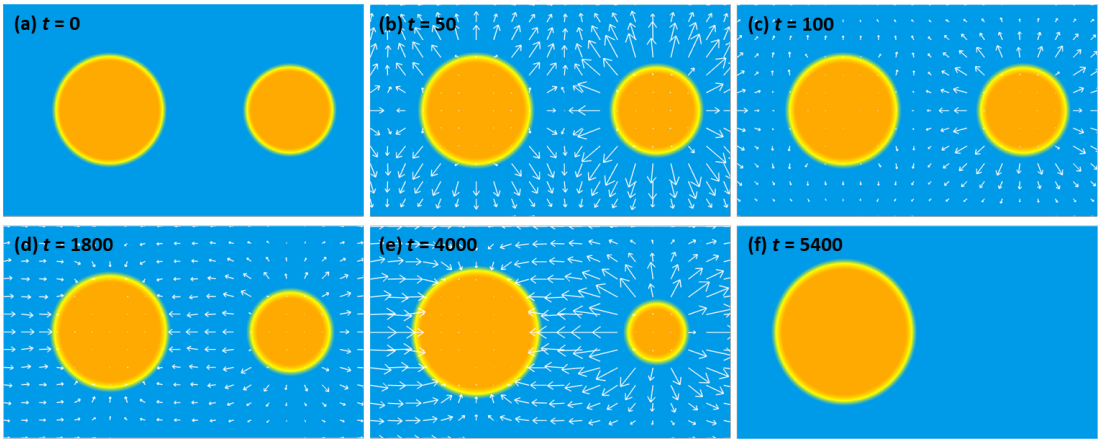

Figure 5.2: Time-lapse images depicting the evolution of morphology and velocity during the droplet ripening process at $T = 0.6$. The timestamp of each image is displayed in the top left corner, and the velocity vector is represented by a white arrow under same reference scale.

smaller one, with no liquid bridge forming between them (Kraska, 2008), and the transfer rate increases significantly as the bulk phase of the smaller droplet disappears (panel e). Eventually the system reaches a steady state and only one stationary droplet remains in the domain (panel f).

It should be emphasised that the ripening behaviour observed in our simulations results from fundamental processes that differ significantly from those described by classical Ostwald ripening theory. Indeed, the latter typically applies to multi-component systems, whereas here we are dealing with a single-component liquid-vapour system where pressure differences rather than concentration gradients drive the process. This mechanism can be easily understood using the Ostwald-Freundlich (OF) equation

$$p_{v1} = p_{eq} \exp\left(\frac{R_c}{R}\right), \tag{5.16}$$

where p_{v1} is the vapour pressure around the droplet, p_{eq} is the equilibrium vapour pressure at a planar liquid surface, and R_c is the critical radius of the droplet. The latter is the radius at which the droplet is in equilibrium with its surrounding vapour, which remains constant at a given temperature. This equation clearly shows that smaller droplets have higher vapour pressures under equilibrium conditions. Consequently, in a system with two droplets of different sizes, a pressure gradient forms between them, with the smaller droplet being surrounded by a higher vapour pressure.

Our simulation results provide direct evidence for the pressure-driven ripening process described by the OF equation. Figure 5.3 shows the number density profile along the centre line of the computational domain at $t = 1800$, highlighting a density gradient between the two droplets that drives mass transfer from the smaller to the larger droplet. It is worth noting

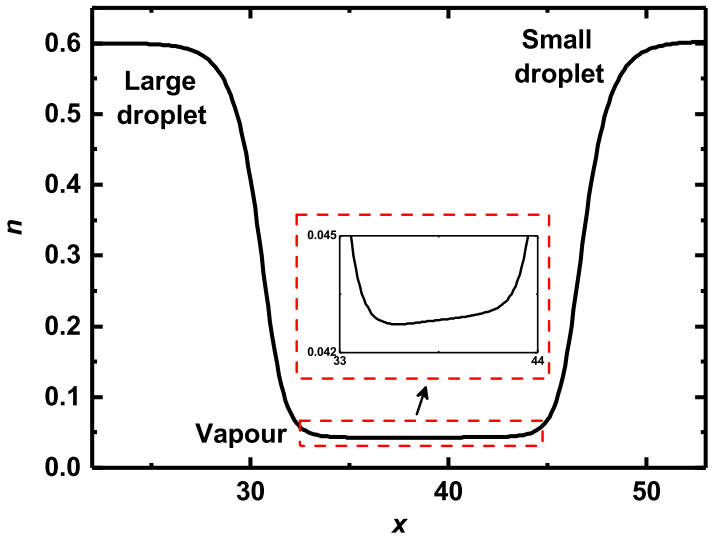

Figure 5.3: Number density profile along the $x-$direction at $y = H/2$. The larger droplet is positioned on the left, while the smaller droplet is on the right. The inset highlights the number density in the vapour region.

that the number density between the droplets is quite low, around 0.042, indicating that the ripening process takes place without liquid bridge formation and/or droplet collision. These simulation results not only confirm our theoretical understanding of pressure-driven ripening in one-component liquid-vapour systems, but also provide a quantitative visualisation of the process.

Quantitative Analysis of Droplet Radius Evolution

In this section, we conduct a detailed quantitative analysis of the ripening process, specifically examining the evolution of individual droplet radius and how the dynamics of ripening are influenced by the presence or absence of a liquid bulk.

A simple model for the rate of change of the droplet radius can be derived by extending the approach to a single component case (X. Chen et al., 2022; Chieco & Durian, 2023; Lemlich, 1978). Specifically, the mass flux is assumed to be proportional to both the droplet surface area $A = 2\pi R$ and the deviation from the equilibrium Laplace pressure, defined as

$$\delta p = \Delta p - \frac{\gamma}{R}, \tag{5.17}$$

so that the mass balance gives

$$\frac{dm}{dt} = kA\delta p, \tag{5.18}$$

where k is a proportional constant. The pressure difference between liquid and vapour in non-equilibrium conditions, Δp, can be easily estimated by considering that the total mass of the two-droplet system is conserved,

$$\Delta p = \frac{2\gamma}{R_1 + R_2}. \tag{5.19}$$

The rates of change for the radii of the two droplets then readily follow

$$\frac{dR_1}{dt} = \frac{k\gamma}{\rho_\ell}\left(\frac{1}{R_{eff}} - \frac{1}{R_1}\right), \tag{5.20a}$$

$$\frac{dR_2}{dt} = \frac{k\gamma}{\rho_\ell}\left(\frac{1}{R_{eff}} - \frac{1}{R_2}\right), \tag{5.20b}$$

where $R_{eff} = (R_1 + R_2)/2$ is calculated by the average radius of the droplets. Note that from Eq. 5.20 it is easy to deduce that the droplet with a radius smaller than the average (i.e. the smaller droplet in this case) will shrink, while the larger droplet will grow.

This simple model can be validated by evaluating the relationship between the radius change rate and the effective Laplace pressure $1/R_{eff} - 1/R$. According to Eqs 5.20, this relationship is expected to be linear with a constant slope of $K = k\gamma/\rho_\ell$, determined solely by the fluid properties. Figure 5.4(a) shows the results for $T = 0.6$, showing a linear relationship up to $t = 4300$, after which the behaviour becomes sub-linear. To investigate the origin of this transition, we have plotted the number density along the horizontal mid-line section at different times. The results clearly show that the transition coincides with the disappearance of the bulk region of the droplet. This is not unexpected, since at this point two key assumptions of the theoretical analysis become invalid, namely the liquid density changes with time and the Young-Laplace equation no longer holds (Blokhuis & Kuipers, 2006; Lulli, Biferale, Falcucci, Sbragaglia, & Shan, 2022).

To complement our understanding of the evolution of the process over time, the dependence of the phase change rate K on temperature is investigated. Figure 5.5(a) shows simulation results for T = 0.55, 0.6 and 0.65. The linear relationship remains valid for these temperatures, with K increasing with temperature. In particular, as shown in Figure 5.5(b), K is found to increase exponentially with temperature, with the best exponential fit giving the relationship $K = 0.525T^{6.52}$.

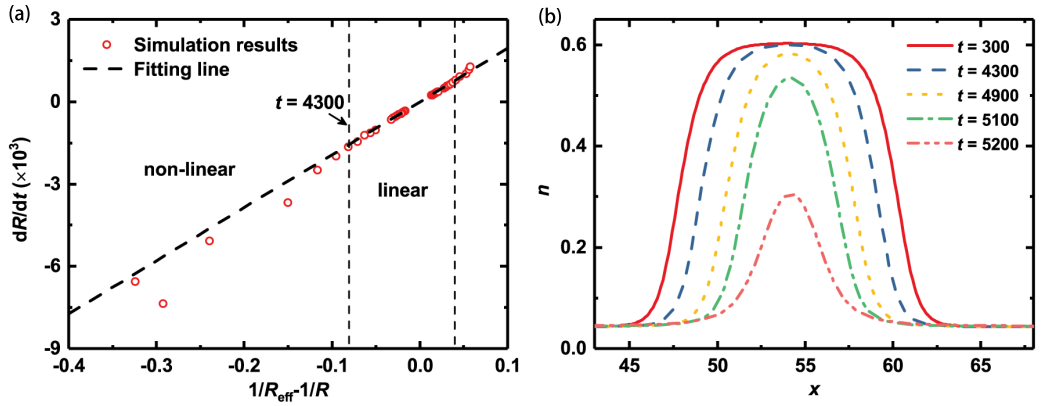

Figure 5.4: (a) The relation between the change rate of radius and the effective Laplace pressure. The red dots are extracted from the simulation while the dashed line is the best linear fitting. The figure is divided into linear and non-linear region with the boundary from the results at $t = 4300$. (b) The number density profile of small droplet along x direction at $y = H/2$.

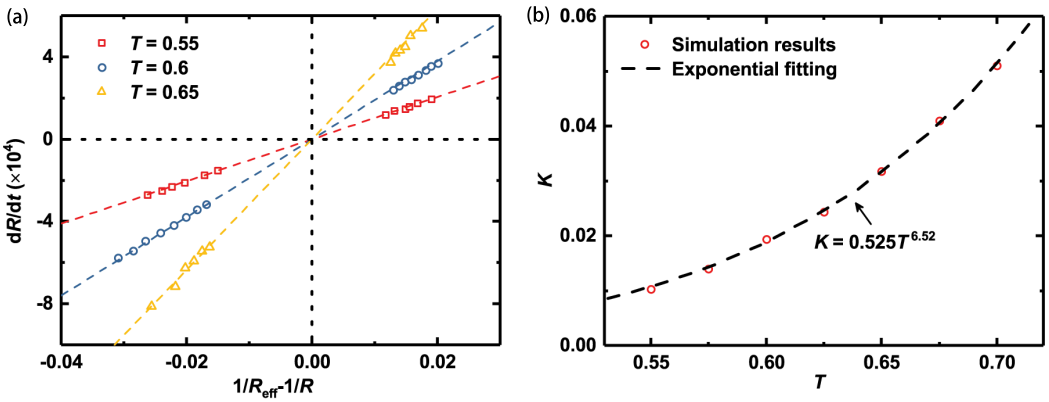

Figure 5.5: (a) The relation between the change rate of radius and the effective Laplace pressure at different temperatures $T = 0.55, 0.6$ and 0.65. The dashed lines are best linear fitting lines of the simulation results. (b) The relation between phase change rate K and the temperature T. The dashed line is the best exponential fitting line in the form of $K = 0.525T^{6.52}$ with coefficient of determination (COD) $= 0.99931$.

5.3.3 Ripening in a Three-Droplet System

In this section we investigate a three-droplet system to assess whether the results of the previous sections are general or depend on the number and arrangement of the droplets. The computational setup consists of three droplets of different radii, $R_1 = 9$, $R_2 = 8$ and $R_3 = 7$, initially randomly distributed in the domain. The temperature in the domain is fixed at $T = 0.6$. The ripening model presented in the previous section can be easily extended to this system and we expect similar main results.

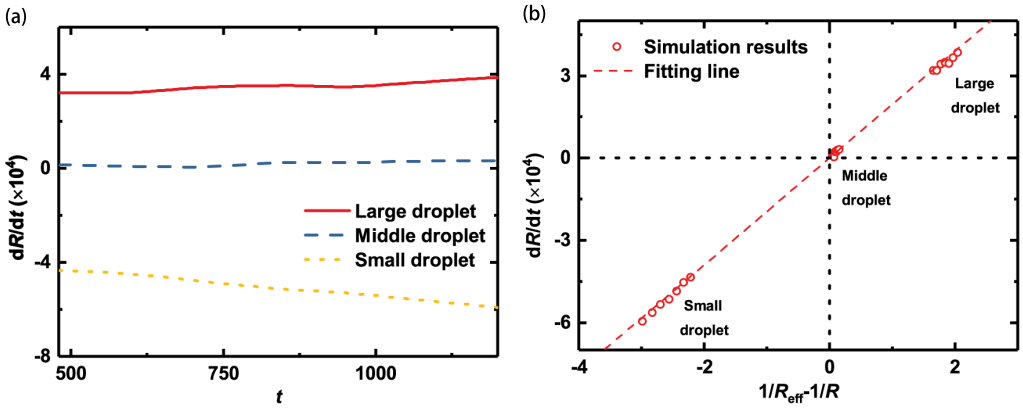

Figure 5.6: (a) The relation between changing rate of radius and the time. (b) The relation between changing rate of radius and effective Laplace pressure. The red dashed line is the best linear fitting line for the simulation results of three droplets.

Figure 5.6(a) shows the relationship between the rate of change of the droplet radii and time in the linear regime when a liquid bulk is present for all droplets, which is consistent with our previous analysis. Since the size of the medium droplet is approximately equal to the average radius of the three droplets, dR_2/dt is expected to be close to zero, and indeed its radius changes only slightly. Meanwhile, the large droplet is increasing in size and the small droplet is decreasing in size, with the rate of change of the small droplet being greater than that of the large droplet. The linear relationship is explicitly shown in Figure 5.6(b) and the slope is found to be 0.01976, which is very close to the value for the two-droplet system, indicating that the number and arrangement of droplets does not affect the overall characteristics of the process.

5.4 Conclusions

In this chapter, we used our recently developed simplified kinetic model to investigate droplet ripening in a two-dimensional, one-component liquid-vapour system. The aim was to demonstrate the model's ability to effectively capture interfacial phenomena overlooked by continuum models, but in a less computationally intensive way than molecular dynamics.

Through simulations and a simple theoretical analysis, our results highlight that the primary driver of droplet ripening is the pressure difference between the vapour phase and the droplets. We observed that the rate of droplet size evolution correlates linearly with the Laplace pressure, provided that the smaller droplet has a bulk region, otherwise non-linear effects come into play, making the relationship sub-linear. Furthermore, we found that the slope of this linear relationship increases exponentially with temperature. Notably, these observations hold across different droplet configurations and numbers.

Looking ahead, future research efforts should focus on extending the current kinetic model to three-dimensional systems in order to more accurately simulate real-world scenarios.

Chapter 6

Concluding Remarks

6.1 Summary of Thesis Content

This thesis focuses on the modelling of polyatomic gases and liquid-vapour flows, where internal energy and dense gas effects significantly influence fluid behaviour. To accurately describe these phenomena, the Boltzmann equation must be extended to include internal degrees of freedom and non-local collision effects in the collision term. While these extended kinetic models offer reliable physical insights, the complexity of the collision terms restricts their applicability to practical engineering problems. To address this limitation, our research simplifies these models by replacing the original collision term with relaxation-based approximations, such as the BGK and Shakhov models. The simplified kinetic models were validated against experimental and MD simulations results, demonstrating their ability to balance computational efficiency with numerical accuracy. These models were subsequently applied to investigate specific cases, including sound wave propagation in confined spaces, evaporation from a planar surface, and droplet ripening. The results provide valuable insights into the design and optimization of relevant MEMS and NEMS devices.

The first study focuses on the simplified kinetic modelling of sound wave propagation in polyatomic gases, employing a BGK-type collision term to account for both elastic and inelastic molecular collisions. Only rotational degrees of freedom are considered as relatively low temperatures are assumed where vibrational modes remain unexcited. The investigation spans a range of rarefaction levels and oscillation frequencies, with an emphasis on understanding how transport coefficients affect gas damping. The results show that both rarefaction and oscillation frequency play significant roles in influencing the pressure amplitude and the resonance/anti-resonance behaviour of sound waves. It was observed that bulk viscosity impacts the pressure amplitude at low rarefaction and oscillation frequency, but this effect diminishes at higher values, where the system exhibits behaviour similar to monatomic gases. The influence of thermal conductivity on the pressure amplitude and total heat flux was found to be minimal. The study also examined the propagation of thermoacoustic waves, with the OCRR being validated analytically and numerically for polyatomic gases.

In the second study, a kinetic model was developed to efficiently simulate liquid-vapour flows, incorporating both repulsive and attractive particle interactions. The repulsive interactions are represented by an approximated collision integral obtained by expanding the Enskog collision integral in Taylor series, approximating the zero-order term by a Shahkov-like relaxation term and the higher order terms by assuming that the distribution function is local Maxwellian. The attractive interactions are modeled using a mean-field approximation so that the particles experience a self-consistent force field generated by their interactions. This hybrid approach allowed the model to handle dense gas effects and interfacial phenomena with greater computational efficiency than MD and DSMC type methods. The model demonstrated excellent agreement with analytical and numerical results from more sophisticated models in equilibrium and nonequilibrium scenarios, offering a reliable and efficient alternative for simulating liquid-vapour flows.

The aforementioned work focuses on the development of a kinetic model for simulating evaporation from a planar surface in a one-dimensional system. Building on this foundation, the model was extended to two dimensions to study droplet ripening in liquid-vapour system, where mass transfer between droplets causes larger droplets to grow while smaller ones shrink. Through simulations and theoretical analysis, it was found that the primary driver of droplet ripening is the Laplace pressure difference between the vapour phase and the droplets. A linear relationship between droplet size evolution and the pressure difference was observed, with non-linear deviations occurring when smaller droplets lacked a bulk region. Additionally, the study highlighted that the slope of this linear relationship increases exponentially with temperature. Notably, these trends are consistent across different droplet configurations and numbers.

The approximate kinetic models developed in this thesis thus provide a good balance between accuracy and computational efficiency, making them valuable tools for investigating and optimising fluid behaviour in MEMS and NEMS applications. Moving forward, we plan to extend our research on the kinetic modelling of liquid-vapour flows in two key directions. First, we aim to modify the EoS to better match the thermal properties of Lennard-Jones fluids, allowing the simulation of more realistic complex fluids. Second, we intend to develop boundary conditions to represent solid walls, thereby addressing the challenge of capturing the fluid-wall interaction dynamics that are critical at the nanoscale. A brief introduction to these two aspects is given in Section 6.2.

6.2 Future Research Directions

6.2.1 Lennard-Jones Fluids within the Enskog-Vlasov Framework

The EV equation is currently the most sophisticated kinetic model for describing liquid-vapour flows (Frezzotti & Barbante, 2017; Frezzotti et al., 2019). It has been successfully applied to describe the evaporation of monatomic fluids (Frezzotti et al., 2005a) and later extended to binary (Frezzotti et al., 2018) and polyatomic (Busuioc & Gibelli, 2020) liquids, demonstrating its robustness. Although the EV provides qualitative agreement with MD at a significantly lower computational cost, it inherently lacks accuracy in reproducing the flow properties of Lennard-Jones fluids due to its underlying assumptions. In fact, MD simulations model molecular interactions using the Lennard-Jones potential, which is expressed as (Meland & Ytrehus, 2003):

$$\phi(r) = \phi_{LJ}\left[\left(\frac{\sigma}{r}\right)^{12} - \left(\frac{\sigma}{r}\right)^{6}\right], \tag{6.1}$$

where the ϕ_{LJ} is the depth of the potential well. By contrast, in the EV equation, molecular interactions are modelled using the Sutherland potential. This assumes infinitely strong repulsion when the molecular distance is less than one diameter, reflecting the hard sphere approximation in Enskog theory, while the attractive interactions are represented by a mean-field approximation of the attractive tail of the Lennard-Jones potential, i.e.,

$$\phi(r) = \begin{cases} +\infty, & r < \sigma, \\ -\phi_{\sigma}\left(\dfrac{\sigma}{r}\right)^{6}, & r \geq \sigma. \end{cases} \tag{6.2}$$

It is evident that the Lennard-Jones and Sutherland potentials exhibit markedly different repulsive interaction characteristics, leading to notable difference in the fluid behaviour. For example, the critical number density and critical temperature of Lennard-Jones fluids are (Chung, Ajlan, Lee, & Starling, 1988):

$$n_c\sigma^3 \approx 0.3185, \quad T_c = 0.3148\frac{\phi_{LJ}}{k_B}, \tag{6.3}$$

whereas these parameters can be obtained through Eq. 4.15 in the EV framework. Although the critical temperature can be matched by adjusting the potential well, the critical reduced number density differs substantially. Moreover, as shown in Figure 6.1, the liquid-vapour coexistence curve derived from the EV equation shows deviations from MD results, particularly at low temperatures.

To address these discrepancies, it is necessary to make appropriate modifications to the EV framework to ensure consistency with MD simulations. A successful attempt was made to model equilibrium liquid-vapour gas flow composed of nearly spherical molecules, such as noble gases (Benilov & Benilov, 2018, 2019a, 2019b). Specifically, within the EV framework,

the EoS was modified to accurately recover the thermal properties of noble gases, as shown below:

$$p = nk_BT\left[1 + n\sigma^3\Phi'(n\sigma^3)\right] - \frac{1}{2}En^2, \tag{6.4}$$

where two free parameters were introduced: the function Φ, which describes the non-ideal part of the fluid's entropy, and the Vlasov parameter E, which characterizes the strength of molecular interaction forces. The expression of Φ was derived to ensure consistency with the critical and triple points of noble gases, including their critical number density, temperature, and pressure, as well as the triple-point number density. Meanwhile, the Vlasov parameter E was determined by fitting a linear relationship to empirical data on the non-ideal component of the per-molecule internal energy for noble gases.

This empirical EoS is incorporated into the simplified kinetic model by adjusting the pair correlation function. Preliminary results comparing the kinetic model with experimental data are shown in Figure 6.1, demonstrating that the model can accurately reproduce key phase-transition properties, including the liquid-vapour coexistence curve and vapour pressure. In the two-dimensional case, the model also predicts the surface tension coefficient of argon, showing close agreement with experimental values. Building on these findings, future work will extend the simplified model to non-equilibrium liquid-vapour flow scenarios to evaluate its consistency with experimental and MD results.

6.2.2 Liquid-Vapour Flows in Confined Geometries

In MEMS and NEMS, liquid-vapour flows in confined channels are more common than the free-boundary cases discussed in Chapters 4 and 5. In these confined spaces, fluid-solid interactions led to fluid inhomogeneities near the wall boundary, where properties such as density, viscosity, and thermal conductivity exhibit significant oscillations at the molecular scale (Hadjiconstantinou, 2024). To capture these effects, Bitsanis, Vanderlick, Tirrell, and Davis (1988) developed a local average density model to determine the viscosity and diffusivity of strongly inhomogeneous fluids. Similarly, Guo, Zhao, and Shi (2006) proposed a simplified kinetic model that applies the local average density approximation to both the pair correlation function and shear viscosity, along with a method for evaluating their gradients. While these models produce results consistent with MD simulations, they are limited by computational complexity or the assumption of isothermal conditions.

To address these limitations, Su et al. (2023) applied the average density theory to the Shakhov-Enskog model, incorporating the fully diffusive Maxwellian boundary condition. Their results for normal shock waves, Couette flow, Fourier flow, and Poiseuille flow showed good agreement with solutions of the Enskog equation, demonstrating that the kinetic model effectively captures inhomogeneities in dense gas flows. Building on this, B. Shan et al. (2023) introduced molecular interactions into the model, further enhancing its accuracy in simulating Couette flows. However, these studies have primarily focused on single-phase dense gas flows.

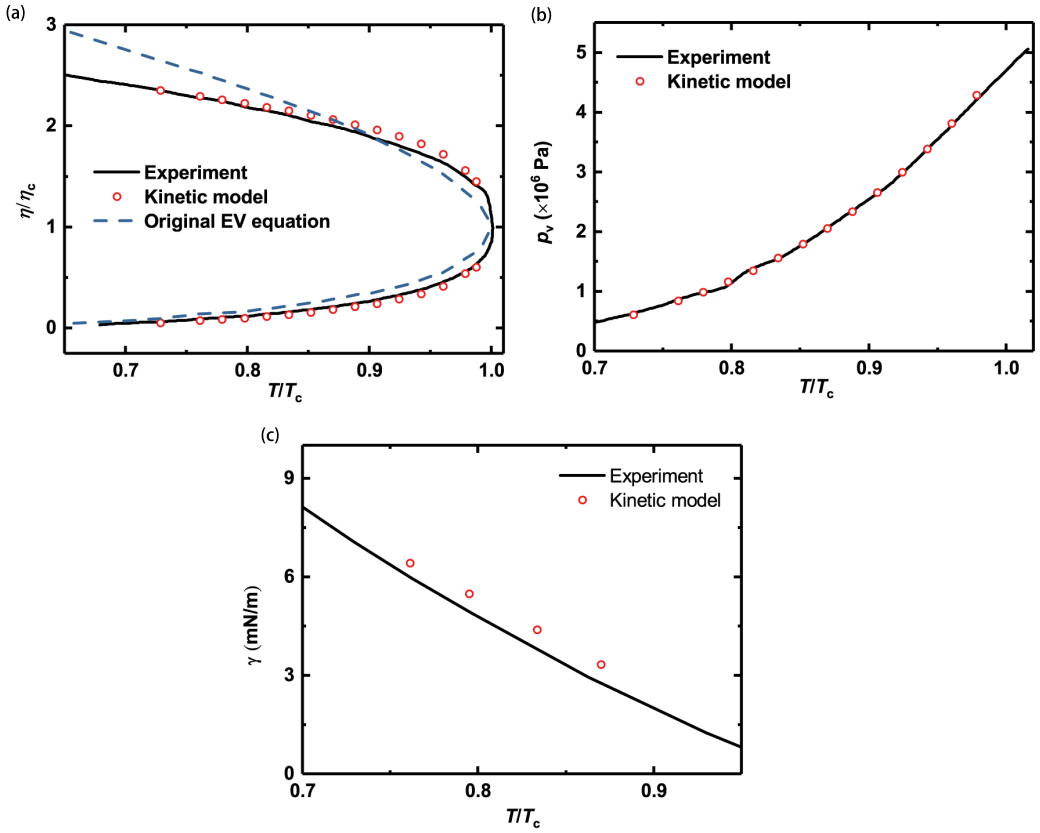

Figure 6.1: Comparison between the results obtained from kinetic model and experiment under different temperatures: (a) reduced number density; (b) vapour pressure; (c) surface tension coefficient. For better illustration, the liquid–vapour coexistence curve obtained from the original EV equation is shown in the figure (a).

Therefore, an important direction for future work is to extend this framework to liquid-vapour flows in confined spaces, where phase transitions introduce new sources of inhomogeneity not present in single-phase systems. For example, molecular-scale density variations, slip velocity and temperature discontinuities at the liquid-solid interface become more pronounced during evaporation and condensation. By applying Shan's model to liquid-vapour flows, we have been able to better understand these complex interactions and investigate the effect of confinement on the phase transition process.

Appendix A

Derivation of the One-Dimensional Kinetic Model

To reduce the computational cost, we first eliminate the dependency of h on the rotational energy I by introducing the following two reduced distribution functions

$$h_0 = \int E_r^0 h \mathrm{d}I, \quad h_1 = \int E_r^0 I h \mathrm{d}I, \tag{A.1}$$

and further letting

$$h_2 = h_1 - \frac{d}{2} h_0, \tag{A.2}$$

where the equilibrium distribution function E_r^0 can be expressed as

$$E_r^0 = \frac{I^{d/2-1}}{\Gamma(d/2)} \exp(-I). \tag{A.3}$$

The governing equations eventually become

$$\begin{aligned} iSt h_0 + v_x \frac{\partial h_0}{\partial x} = \delta & \left[\rho + 2U v_x + \tau_t \left(|\boldsymbol{v}|^2 - \frac{3}{2} \right) + \frac{4}{15} Q_t v_x \left(|\boldsymbol{v}|^2 - \frac{5}{2} \right) - h_0 \right] \\ & + \frac{\delta}{Z} \left[(\tau - \tau_t) \left(|\boldsymbol{v}|^2 - \frac{3}{2} \right) + \frac{4(Q' - Q_t) v_x}{15} \left(|\boldsymbol{v}|^2 - \frac{5}{2} \right) \right], \end{aligned} \tag{A.4}$$

$$h_2 + v_x \frac{\partial h_2}{\partial x} = \delta \left[\frac{d}{2} \tau_r - h_2 \right] + \frac{d\delta}{2Z} (\tau - \tau_r) + \frac{2\delta}{Z} Q''' v_x, \tag{A.5}$$

where

$$Q''' = -A_{rt} Z Q_t + Z(1 - A_{rr}) Q_r. \tag{A.6}$$

The macroscopic quantities are calculated from h_0 and h_2 as

$$[\rho, U, \tau_t, Q_t] = \int \left[1, v_x, \frac{2}{3} |\boldsymbol{v}|^2 - 1, v_x \left(|\boldsymbol{v}|^2 - \frac{5}{2} \right) \right] E_t^0 h_0 \mathrm{d}\boldsymbol{v}, \tag{A.7}$$

$$[\tau_r, Q_r] = \int \left[\frac{2}{d}, v_x \right] E_t^0 h_2 \mathrm{d}\boldsymbol{v}. \tag{A.8}$$

Now we transform the governing equations from the three-dimensional velocity space to the one-dimensional velocity space by introducing the following reduced distributions:

$$\Phi_0(x,v_x) = \frac{1}{\pi}\int \exp(-v_y^2 - v_z^2) h_0 \mathrm{d}v_y \mathrm{d}v_z, \tag{A.9}$$

$$\Phi_1(x,v_x) = \frac{1}{\pi}\int \exp(-v_y^2 - v_z^2)\left(v_y^2 + v_z^2 - 1\right) h_0 \mathrm{d}v_y \mathrm{d}v_z, \tag{A.10}$$

$$\Psi(x,v_x) = \frac{1}{\pi}\int \exp(-v_y^2 - v_z^2) h_2 \mathrm{d}v_y \mathrm{d}v_z. \tag{A.11}$$

Then the governing equations become

$$\begin{aligned} iSt\Phi_0 + v_x\frac{\partial \Phi_0}{\partial x} = \delta\left[\rho + 2Uv_x + \tau_t\left(v_x^2 - \frac{1}{2}\right) + \frac{4}{15}Q_t v_x\left(v_x^2 - \frac{3}{2}\right) - \Phi_0\right] \\ + \frac{\delta}{Z}\left[(\tau - \tau_t)\left(v_x^2 - \frac{1}{2}\right) + \frac{4(Q^{'} - Q_t)v_x}{15}\left(v_x^2 - \frac{3}{2}\right)\right], \end{aligned} \tag{A.12}$$

$$iSt\Phi_1 + v_x\frac{\partial \Phi_1}{\partial x} = \delta\left[\tau_t + \frac{4}{15}Q_t v_x - \Phi_1\right] + \frac{\delta}{Z}\left[(\tau - \tau_t) + \frac{4(Q^{'} - Q_t)v_x}{15}\right], \tag{A.13}$$

$$\Psi + v_x\frac{\partial \Psi}{\partial x} = \delta\left[\frac{d}{2}\tau_r - \Psi\right] + \frac{d\delta}{2Z}(\tau - \tau_r) + \frac{2\delta}{Z}Q^{'''}v_x. \tag{A.14}$$

The full diffuse boundary conditions for Φ_0, $\Phi_1$and Ψ can be obtained using

$$\Phi_0(x=0, v_x>0) = \sqrt{\pi}U_m - 2\sqrt{\pi}\int_{v_x\le 0} v_x E_t^{01}\Phi_0 \boldsymbol{d}v_x + 2U_m v_x + \tau_m(v_x^2 - 1), \tag{A.15}$$

$$\Phi_0(x=1, v_x<0) = \sqrt{\pi}U_m + 2\sqrt{\pi}\int_{v_x\ge 0} v_x E_t^{01}\Phi_0 \boldsymbol{d}v_x + 2U_m v_x + \tau_m(v_x^2 - 1), \tag{A.16}$$

$$\Phi_1(x=1, v_x<0) = \Phi_1(x=1, v_x>0) = \tau_w(v_x^2 - \frac{3}{2}), \tag{A.17}$$

$$\Psi(x=1, v_x<0) = \Psi(x=1, v_x>0) = \frac{d}{2}\tau_w, \tag{A.18}$$

with the equilibrium distribution function

$$E_t^{01} = \frac{1}{\sqrt{\pi}}\exp(-v_x^2). \tag{A.19}$$

The macroscopic quantities can be calculated by

$$\begin{aligned}[\rho, U, \tau_t, Q_t] = &\int \left[1, v_x, \frac{2}{3}(v_x^2 - \frac{1}{2}), v_x\left(v_x^2 - \frac{3}{2}\right)\right] E_t^{01} \Phi_0 \mathrm{d}v_x \\ &+ \int \left[0, 0, \frac{2}{3}, v_x\right] E_t^{01} \Phi_1 \mathrm{d}v_x,\end{aligned} \tag{A.20}$$

$$[\tau_r, Q_r] = \int \left[\frac{2}{d}, v_x\right] E_t^{01} \Psi \mathrm{d}v_x. \tag{A.21}$$

Appendix B

Derivation of the Pressure Contributions

In a dense fluid, the stress tensor and the heat flux contain kinetic and collisional contributions, the former associated with the flow of molecules and the latter associated with the collisional transfer of molecules (Kremer, 2010). The kinetic contributions to the stress tensor and the heat flux are given by

$$\boldsymbol{p}^K = \int m\boldsymbol{C}\boldsymbol{C} f(\boldsymbol{x},\boldsymbol{\xi},t)\mathrm{d}\boldsymbol{\xi}, \tag{B.1}$$

and Eq. 4.6, respectively.

To derive the collisional part of the stress tensor $\boldsymbol{p}^C$ and heat flux $\boldsymbol{q}^C$, we first multiply Eq. 4.2a by the collision invariants $m, m\boldsymbol{\xi}, \frac{1}{2}m\boldsymbol{\xi}^2$ and integrate over the molecular velocity $\boldsymbol{\xi}$. The resulting balance equations for mass, momentum, and energy are as follows:

$$\frac{\partial \rho}{\partial t} + \nabla\cdot(\rho\boldsymbol{u}) = \int m\Omega d\boldsymbol{\xi}, \tag{B.2a}$$

$$\frac{\partial(\rho\boldsymbol{u})}{\partial t} + \nabla\cdot(\rho\boldsymbol{u}\boldsymbol{u}) + \nabla\cdot\boldsymbol{p}^K = \rho\frac{\boldsymbol{F}}{m} + \int m\boldsymbol{\xi}\Omega d\boldsymbol{\xi}, \tag{B.2b}$$

$$\frac{\partial \rho e}{\partial t} + \nabla\cdot(\rho e\boldsymbol{u}) + \nabla\cdot(\boldsymbol{q}^K + \boldsymbol{p}^K\cdot\boldsymbol{u}) = \rho\frac{\boldsymbol{F}}{m}\cdot\boldsymbol{u} + \int \frac{m}{2}\boldsymbol{\xi}^2\Omega d\boldsymbol{\xi}, \tag{B.2c}$$

where $e = c_v T + \frac{1}{2}\boldsymbol{u}^2$ is the total energy per unit mass of the gas. For dense gases, the integral terms on the right side of the equations do not vanish. These nonlocal transport terms can be written as (Cercignani & Lampis, 1988; Frezzotti, 1999)

$$\int m\Omega d\boldsymbol{\xi} = 0, \tag{B.3a}$$

$$\int m\boldsymbol{\xi}\Omega d\boldsymbol{\xi} = -\nabla\cdot\boldsymbol{p}^C, \tag{B.3b}$$

$$\int \frac{m}{2}\boldsymbol{\xi}^2\Omega d\boldsymbol{\xi} = -\nabla\cdot(\boldsymbol{q}^C + \boldsymbol{p}^C\cdot\boldsymbol{u}). \tag{B.3c}$$

Substituting Eq. 4.4b and Eq. 4.4c into the left side of Eq. (B.3b) and Eq. (B.3c), the following equations are obtained:

$$\int m\boldsymbol{\xi} J_S d\boldsymbol{\xi} = 0, \tag{B.4a}$$

$$\int m\boldsymbol{\xi} J_e d\boldsymbol{\xi} = -\nabla\cdot[\rho b\chi n k_B T - \varpi(\nabla\cdot\boldsymbol{u})]\boldsymbol{I}, \tag{B.4b}$$

$$\int \frac{m}{2}\boldsymbol{\xi}^2 J_S d\boldsymbol{\xi} = 0, \tag{B.4c}$$

$$\int \frac{m}{2}\boldsymbol{\xi}^2 J_e d\boldsymbol{\xi} = -\nabla\cdot[\rho b\chi n k_B T - \varpi(\nabla\cdot\boldsymbol{u})]\boldsymbol{u}, \tag{B.4d}$$

where $\boldsymbol{I}$ is the unit tensor. Accordingly, the collisional contributions to the stress tensor and heat flux turn out to be

$$\boldsymbol{p}^C = [\rho b\chi n k_B T - \varpi(\nabla\cdot\boldsymbol{u})]\boldsymbol{I}, \tag{B.5a}$$

$$\boldsymbol{q}^C = 0. \tag{B.5b}$$

Note that in equilibrium the gradient of the kinetic and collisional contributions to the xx-component of the stress tensor must balance the self-consistent force field (Frezzotti & Gibelli, 2003),

$$\frac{d}{dx}(p_{xx}^K + p_{xx}^C) = n(x)F_x(x), \tag{B.6}$$

where the one-dimensional kinetic and collisional contributions to the stress tensor are

$$p_{xx}^K = n k_B T, \tag{B.7a}$$

$$p_{xx}^C = \rho b\chi n k_B T - \varpi\frac{\partial u_x}{\partial x}. \tag{B.7b}$$

Bibliography

Alder, B. J., & Wainwright, T. E. (1957). Phase transition for a hard sphere system. *The Journal of Chemical Physics*, *27*(5), 1208–1209.

Alder, B. J., & Wainwright, T. E. (1959). Studies in molecular dynamics. I. General method. *The Journal of Chemical Physics*, *31*(2), 459–466.

Alexander, F. J., Garcia, A. L., & Alder, B. J. (1997). The consistent Boltzmann algorithm for the van der Waals equation of state. *Physica A: Statistical Mechanics and its Applications*, *240*(1-2), 196–201.

Alsmeyer, H. (1976). Density profiles in argon and nitrogen shock waves measured by the absorption of an electron beam. *Journal of Fluid Mechanics*, *74*(3), 497–513.

Aoki, K., Sone, Y., & Yamada, T. (1990). Numerical analysis of gas flows condensing on its plane condensed phase on the basis of kinetic theory. *Physics of Fluids A: Fluid Dynamics*, *2*(10), 1867–1878.

Arima, T., Ruggeri, T., & Sugiyama, M. (2017). Rational extended thermodynamics of a rarefied polyatomic gas with molecular relaxation processes. *Physical Review E*, *96*(4), 042143.

Ariyaprakai, S., & Dungan, S. (2010). Influence of surfactant structure on the contribution of micelles to Ostwald ripening in oil-in-water emulsions. *Journal of Colloid and Interface Science*, *343*(1), 102–108.

Aursand, E., & Ytrehus, T. (2019). Comparison of kinetic theory evaporation models for liquid thin-films. *International Journal of Multiphase Flow*, *116*, 67–79.

Barbante, P. F., Frezzotti, A., & Gibelli, L. (2015). A kinetic theory description of liquid menisci at the microscale. *Kinetic and Related Models*, *8*(2), 235–254.

Benilov, E. S., & Benilov, M. S. (2018). Energy conservation and H theorem for the Enskog-Vlasov equation. *Physical Review E*, *97*(6), 062115.

Benilov, E. S., & Benilov, M. S. (2019a). The Enskog-Vlasov equation: a kinetic model describing gas, liquid, and solid. *Journal of Statistical Mechanics: Theory and Experiment*, *2019*(10), 103205.

Benilov, E. S., & Benilov, M. S. (2019b). Peculiar property of noble gases and its explanation through the Enskog-Vlasov model. *Physical Review E*, *99*(1), 012144.

Bhatnagar, P. L., Gross, E. P., & Krook, M. (1954). A model for collision processes in gases. i. Small amplitude processes in charged and neutral one-component systems. *Physical Review*, *94*(3), 511.

Bird, G. A. (1994). *Molecular gas dynamics and the direct simulation of gas flows*. Oxford university press.

Bisi, M., & Lorenzani, S. (2016). High-frequency sound wave propagation in binary gas mixtures flowing through microchannels. *Physics of Fluids*, *28*(5), 052003.

Bitsanis, I., Vanderlick, T. K., Tirrell, M., & Davis, H. T. (1988). A tractable molecular theory of flow in strongly inhomogeneous fluids. *The Journal of Chemical Physics*, *89*(5), 3152–3162.

Blokhuis, E. M., & Kuipers, J. (2006). Thermodynamic expressions for the Tolman length. *The Journal of Chemical Physics*, *124*(7).

Boley, C. D., Desai, R. C., & Tenti, G. (1972). Kinetic models and Brillouin scattering in a molecular gas. *Canadian Journal of Physics*, *50*(18), 2158–2173.

Boltzmann, L. E. (1872). Further studies on the thermal equilibrium of gas molecules. *The Kinetic Theory of Gases. An Anthology of Classic Papers with Historical Commentary*, 262-349.

Boom, B. A., Bertolini, A., Hennes, E., & van den Brand, J. F. J. (2021). Gas damping in capacitive MEMS transducers in the free molecular flow regime. *Sensors*, *21*(7), 2566.

Borgnakke, C., & Larsen, P. S. (1975). Statistical collision model for Monte Carlo simulation of polyatomic gas mixture. *Journal of Computational Physics*, *18*(4), 405–420.

Bray, A. J. (1994). Theory of phase-ordering kinetics. *Advances in Physics*, *43*(3), 357–459.

Bruno, D., & Frezzotti, A. (2019). Dense gas effects in the rayleigh-brillouin scattering spectra of SF6. *Chemical Physics Letters*, *731*, 136595.

Brutin, D., Sobac, B., Loquet, B., & Sampol, J. (2011). Pattern formation in drying drops of blood. *Journal of Fluid Mechanics*, *667*, 85–95.

Busuioc, S. (2023). Quadrature-based lattice Boltzmann model for non-equilibrium dense gas flows. *Physics of Fluids*, *35*(1).

Busuioc, S. (2024). Mesoscopic lattice Boltzmann modeling of dense gas flows in curvilinear geometries. *Physical Review Fluids*, *9*(5), 053401.

Busuioc, S., Frezzotti, A., & Gibelli, L. (2023). A weighted particle scheme for enskog-vlasov equation to simulate spherical nano-droplets/bubbles. *Journal of Computational Physics*, *475*, 111873.

Busuioc, S., & Gibelli, L. (2020). Mean-field kinetic theory approach to langmuir evaporation of polyatomic liquids. *Physics of Fluids*, *32*(9), 093314.

Busuioc, S., Gibelli, L., Lockerby, D. A., & Sprittles, J. E. (2020). Velocity distribution function of spontaneously evaporating atoms. *Physical Review Fluids*, *5*(10), 103401.

Busuioc, S., & Sofonea, V. (2024). Bounded flows of dense gases. *Physical Review Fluids*, *9*(2), 023401.

Carnahan, N. F., & Starling, K. E. (1969). Equation of state for nonattracting rigid spheres. *The Journal of Chemical Physics*, *51*(2), 635–636.

Casimir, H. B. G. (1945). On Onsager's principle of microscopic reversibility. *Reviews of Modern Physics*, *17*(2-3), 343.

Cercignani, C., & Lampis, M. (1988). Kinetic theory of a dense gas of rough spheres. *Journal of Statistical Physics*, *53*, 655.

Chapman, S., & Cowling, T. G. (1952). *The mathematical theory of Non-Uniform gases*. Cambridge University Press.

Chen, L., Kang, Q., Mu, Y., He, Y., & Tao, W. (2014). A critical review of the pseudopotential multiphase lattice Boltzmann model: Methods and applications. *International Journal of Heat and Mass Transfer*, *76*, 210–236.

Chen, S., Xu, K., & Cai, Q. (2015). A comparison and unification of ellipsoidal statistical and Shakhov BGK models. *Advances in Applied Mathematics and Mechanics*, *7*(2), 245–266.

Chen, T., Wu, L., Wang, L., & Chen, S. (2023). Rarefaction effects in head-on collision of two near-critical droplets. *International Journal of Multiphase Flow*, *164*, 104451.

Chen, X., Feng, J., Hu, H., Du, P., & Wang, T. (2022). Lattice Boltzmann method based simulation of two dimensional bubble group ripening process br. *Acta Physica Sinica*, *71*(11).

Chibbaro, S., Falcucci, G., Chiatti, G., Chen, H., Shan, X., & Succi, S. (2008). Lattice Boltzmann models for nonideal fluids with arrested phase-separation. *Physical Review E—Statistical, Nonlinear, and Soft Matter Physics*, *77*(3), 036705.

Chieco, A. T., & Durian, D. J. (2023). Simply solvable model capturing the approach to statistical self-similarity for the diffusive coarsening of bubbles, droplets, and grains. *Physical Review E*, *108*(3), 034606.

Chigullapalli, S., Weaver, A., & Alexeenko, A. (2012). Nonlinear effects in squeeze-film gas damping on microbeams. *Journal of Micromechanics and Microengineering*, *22*(6), 065010.

Chung, T. H., Ajlan, M., Lee, L. L., & Starling, K. E. (1988). Generalized multiparameter correlation for nonpolar and polar fluid transport properties. *Industrial & Engineering Chemistry Research*, *27*(4), 671–679.

Clark, J. R., Hsu, W. T., Abdelmoneum, M. A., & Nguyen, C. C. (2005). High-Q UHF micromechanical radial-contour mode disk resonators. *Journal of Microelectromechanical Systems*, *14*(6), 1298–1310.

Cox, E. A., Mortell, M. P., & Reck, S. (2002). Nonlinear standing and resonantly forced oscillations in a tube with slowlychanging length. *SIAM Journal on Applied Mathematics*, *62*(3), 965–989.

Cramer, M. S. (2012). Numerical estimates for the bulk viscosity of ideal gases. *Physics of Fluids*, *24*(6).

Dąbrowski, A. (2001). Adsorption—from theory to practice. *Advances in Colloid and Interface Science*, *93*(1-3), 135–224.

Dain, Y., & Lueptow, R. M. (2001a). Acoustic attenuation in a three-gas mixture: Results. *The Journal of the Acoustical Society of America*, *110*(6), 2974–2979.

Dain, Y., & Lueptow, R. M. (2001b). Acoustic attenuation in three-component gas mixtures—Theory. *The Journal of the Acoustical Society of America*, *109*(5), 1955–1964.

Desvillettes, L., & Lorenzani, S. (2012). Sound wave resonances in micro-electro-mechanical systems devices vibrating at high frequencies according to the kinetic theory of gases. *Physics of Fluids*, *24*(9), 092001.

Dong, Y., Poredoš, P., Ma, Q., & Wang, R. (2022). High-yielding and stable desalination via photothermal membrane distillation with free-flow evaporation channel. *Desalination*, *543*, 116103.

Ejakov, S. G., Phillips, S., Dain, Y., Lueptow, R. M., & Visser, J. H. (2003). Acoustic attenuation in gas mixtures with nitrogen: Experimental data and calculations. *The Journal of the Acoustical Society of America*, *113*(4), 1871–1879.

Emerson, D. R., Gu, X., Stefanov, S. K., Sun, Y., & Barber, R. W. (2007). Nonplanar oscillatory shear flow: From the continuum to the free-molecular regime. *Physics of Fluids*, *19*(10).

Enskog, D. (1922). Kinetische theorie der wärmeleitung: Reibung und selbst-diffusion in gewissen verdichteten gasen und flüssigkeiten. *Almqvist Wiksells Boktryckeri*.

Eucken, A. (1913). Über das wärmeleitvermögen, die spezifische wärme und die innere reibung der gase. *Physikalische Zeitschrift*, *14*(8), 324–332.

Fan, D., Chen, S. P., Chen, L., & Voorhees, P. W. (2002). Phase-field simulation of 2-D Ostwald ripening in the high volume fraction regime. *Acta Materialia*, *50*(8), 1895–1907.

Fei, F., Liu, H., Liu, Z., & Zhang, J. (2020). A benchmark study of kinetic models for shock waves. *AIAA Journal*, *58*(6), 2596–2608.

Frangi, A., Frezzotti, A., & Lorenzani, S. (2007). On the application of the BGK kinetic model to the analysis of gas-structure interactions in MEMS. *Computers & Structures*, *85*(11-14), 810–817.

Frezzotti, A. (1997). A particle scheme for the numerical solution of the Enskog equation. *Physics of Fluids*, *9*(5), 1329–1335.

Frezzotti, A. (1999). Monte Carlo simulation of the heat flow in a dense hard sphere gas. *European Journal of Mechanics-B/Fluids*, *18*(1), 103–119.

Frezzotti, A. (2007). A numerical investigation of the steady evaporation of a polyatomic gas. *European Journal of Mechanics-B/Fluids*, *26*(1), 93–104.

Frezzotti, A. (2011). Boundary conditions at the vapor-liquid interface. *Physics of Fluids*, *23*(3), 030609.

Frezzotti, A., & Barbante, P. (2017). Kinetic theory aspects of non-equilibrium liquid-vapor flows. *Mechanical Engineering Reviews*, *4*(2), 16–00540.

Frezzotti, A., Barbante, P., & Gibelli, L. (2019). Direct simulation Monte Carlo applications to liquid-vapor flows. *Physics of Fluids*, *31*(6).

Frezzotti, A., & Gibelli, L. (2003). A kinetic model for equilibrium and non-equilibrium structure of the vapor-liquid interface. In *Aip conference proceedings* (Vol. 663, pp. 980–987).

Frezzotti, A., Gibelli, L., Lockerby, D. A., & Sprittles, J. E. (2018). Mean-field kinetic theory approach to evaporation of a binary liquid into vacuum. *Physical Review Fluids*, *3*(5), 054001.

Frezzotti, A., Gibelli, L., & Lorenzani, S. (2005a). Mean field kinetic theory description of evaporation of a fluid into vacuum. *Physics of Fluids*, *17*(1).

Frezzotti, A., Gibelli, L., & Lorenzani, S. (2005b). Mean field kinetic theory description of evaporation of a fluid into vacuum. *Physics of Fluids*, *17*(1).

Gad-el Hak, M. (1999). The fluid mechanics of microdevices—the Freeman scholar lecture. *Journal of Fluids Engineering*, *121*, 5-33.

Gallis, M., & Torczynski, J. (2000). The application of the BGK model in particle simulations. In *34th thermophysics conference* (p. 2360).

Gan, C., Chen, S., & Zhang, J. (2023). DSMC study of micro-ablation for reentry vehicles. *Chinese Journal of Theoretical and Applied Mechanics*, *55*(9), 1847–1857.

Garcia, R. D. M., & Siewert, C. E. (2005). The linearized Boltzmann equation: sound-wave propagation in a rarefied gas. *Zeitschrift fur Angewandte Mathematik und Physik ZAMP*, *57*(1), 94–122.

Gavasane, A., Agrawal, A., Pradeep, A. M., & Bhandarkar, U. (2017). Simulation of a temperature drop for the flow of rarefied gases in microchannels. *Numerical Heat Transfer*, *71*(10), 1066-1079.

Goldstein, D., Sturtevant, B., & Broadwell, J. E. (1989). Investigations of the motion of discrete-velocity gases. *Progress in Astronautics and Aeronautics*, *117*, 100–117.

Gong, W., Yan, Y., & Chen, S. (2018). A study on the unphysical mass transfer of SCMP pseudopotential LBM. *International Journal of Heat and Mass Transfer*, *123*, 815–820.

Gorji, M. H., & Jenny, P. (2013). A Fokker–Planck based kinetic model for diatomic rarefied gas flows. *Physics of Fluids*, *25*(6), 062002.

Graur, I. A., Gatapova, E. Y., Wolf, M., & Batueva, M. A. (2021). Non-equilibrium evaporation: 1D benchmark problem for single gas. *International Journal of Heat and Mass Transfer*, *181*, 121997.

Green, M. S. (1954). Markoff random processes and the statistical mechanics of time-dependent phenomena. II. Irreversible processes in fluids. *The Journal of Chemical Physics*, *22*(3), 398–413.

Greenspan, M. (1959). Rotational relaxation in nitrogen, oxygen, and air. *The Journal of the Acoustical Society of America*, *31*(2), 155–160.

Grmela, M. (1971). Kinetic equation approach to phase transitions. *Journal of Statistical Physics*, *3*, 347–364.

Gross, E. P., & Jackson, E. A. (1959). Kinetic models and the linearized Boltzmann equation. *The Physics of Fluids*, *2*(4), 432–441.

Guo, Z., & Shu, C. (2013). *Lattice Boltzmann method and its application in engineering* (Vol. 3). World Scientific.

Guo, Z., Zhao, T. S., & Shi, Y. (2006). Generalized hydrodynamic model for fluid flows: From nanoscale to macroscale. *Physics of Fluids*, *18*(6).

Hadjiconstantinou, N. G. (2002). Sound wave propagation in transition-regime micro-and nanochannels. *Physics of Fluids*, *14*(2), 802–809.

Hadjiconstantinou, N. G. (2024). Molecular mechanics of liquid and gas slip flow. *Annual Review of Fluid Mechanics*, *56*(1), 435–461.

Hanley, H. J. M., McCarty, R. D., & Cohen, E. G. D. (1972). Analysis of the transport coefficients for simple dense fluid: Application of the modified Enskog theory. *Physica*, *60*(2), 322–356.

Hanson, F. B., & Morse, T. F. (1967). Kinetic models for a gas with internal structure. *The Physics of Fluids*, *10*(2), 345–353.

Hardy, S. C., & Voorhees, P. W. (1988). Ostwald ripening in a system with a high volume fraction of coarsening phase. *Metallurgical Transactions A*, *19*, 2713–2721.

He, X., & Doolen, G. D. (2002). Thermodynamic foundations of kinetic theory and lattice Boltzmann models for multiphase flows. *Journal of Statistical Physics*, *107*, 309–328.

Hertz, H. (1882). Ueber die Verdunstung der Flüssigkeiten, insbesondere des Quecksilbers, im luftleeren Raume. *Annalen der Physik*, *253*(10), 177–193.

Heyes, D. M., & Santos, A. (2016). Chemical potential of a test hard sphere of variable size in a hard-sphere fluid. *The Journal of Chemical Physics*, *145*(21), 214504.

Holway, L. H. (1966). New statistical models for kinetic theory: methods of construction. *The Physics of Fluids*, *9*(9), 1658–1673.

Huang, R., Wu, H., & Adams, N. A. (2021). Mesoscopic lattice Boltzmann modeling of the liquid-vapor phase transition. *Physical Review Letters*, *126*(24), 244501.

Ivanov, M. S., & Rogasinskii, S. V. (1991). Theoretical analysis of traditional and modern schemes of the DSMC method. *Rarefied Gas Dynamics*, 629–642.

Jaeger, F., Matar, O. K., & Müller, E. A. (2018). Bulk viscosity of molecular fluids. *The Journal of Chemical Physics*, *148*(17), 174504.

John, B., Enright, R., Sprittles, J. E., Gibelli, L., Emerson, D. R., & Lockerby, D. A. (2019). Numerical investigation of nanoporous evaporation using direct simulation Monte Carlo. *Physical Review Fluids*, *4*(11), 113401.

John, B., Gibelli, L., Enright, R., Sprittles, J. E., Lockerby, D. A., & Emerson, D. R. (2021). Evaporation from arbitrary nanoporous membrane configurations: An effective evaporation coefficient approach. *Physics of Fluids*, *33*(3), 032022.

Kalempa, D., & Sharipov, F. (2009). Sound propagation through a rarefied gas confined between source and receptor at arbitrary Knudsen number and sound frequency. *Physics of Fluids*, *21*(10), 103601.

Kalempa, D., & Sharipov, F. (2012). Sound propagation through a rarefied gas. Influence of the gas–surface interaction. *International Journal of Heat and Fluid Flow*, *38*, 190–199.

Kalempa, D., & Sharipov, F. (2014). Numerical modelling of thermoacoustic waves in a rarefied gas confined between coaxial cylinders. *Vacuum*, *109*, 326–332.

Karkheck, J., & Stell, G. (1981). Kinetic mean-field theories. *The Journal of Chemical Physics*, *75*(3), 1475–1487.

Kavokine, N., Netz, R. R., & Bocquet, L. (2021). Fluids at the nanoscale: from continuum to subcontinuum transport. *Annual Review of Fluid Mechanics*, *53*(1), 377–410.

Khayet, M. (2011). Membranes and theoretical modeling of membrane distillation: A review. *Advances in Colloid and Interface Science*, *164*(1-2), 56–88.

Khodabandeh, R., & Furberg, R. (2010). Heat transfer, flow regime and instability of a nano- and micro-porous structure evaporator in a two-phase thermosyphon loop. *International Journal of Thermal Sciences*, *49*(7), 1183–1192.

Knudsen, M. (1915). Die maximale verdampfungsgeschwindigkeit des quecksilbers. *Annalen der Physik*, *352*(13), 697–708.

Kobayashi, K., Sasaki, K., Kon, M., Fujii, H., & Watanabe, M. (2017). Kinetic boundary conditions for vapor–gas binary mixture. *Microfluidics and Nanofluidics*, *21*, 1–13.

Koch, S. W., Desai, R. C., & Abraham, F. F. (1983). Dynamics of phase separation in two-dimensional fluids: spinodal decomposition. *Physical Review A*, *27*(4), 2152.

Kon, M., Kobayashi, K., & Watanabe, M. (2014). Method of determining kinetic boundary conditions in net evaporation/condensation. *Physics of Fluids*, *26*(7).

Kosuge, S., & Aoki, K. (2018). Shock-wave structure for a polyatomic gas with large bulk viscosity. *Physical Review Fluids*, *3*(2), 023401.

Kraska, T. (2008). Direct observation of single Ostwald ripening processes by molecular dynamics simulation. *The Journal of Physical Chemistry B*, *112*(39), 12408–12413.

Kremer, G. M. (2010). *An introduction to the Boltzmann equation and transport processes in gases*. Springer Science & Business Media.

Kremer, G. M., Kunova, O. V., Kustova, E. V., & Oblapenko, G. P. (2018). The influence of vibrational state-resolved transport coefficients on the wave propagation in diatomic gases. *Physica A: Statistical Mechanics and its Applications*, *490*, 92–113.

Kubo, R. (1957). Statistical-mechanical theory of irreversible processes. I. General theory and simple applications to magnetic and conduction problems. *Journal of the Physical Cociety of Japan*, *12*(6), 570–586.

Kustova, E., Mekhonoshina, M., Bechina, A., Lagutin, S., & Voroshilova, Y. (2023). Continuum models for bulk viscosity and relaxation in polyatomic gases. *Fluids*, *8*(2), 48.

Labuntsov, D. A., & Kryukov, A. P. (1979). Analysis of intensive evaporation and condensation. *International Journal of Heat and Mass Transfer*, *22*(7), 989–1002.

Larina, I. N., & Rykov, V. A. (2010). Kinetic model of the Boltzmann equation for a diatomic gas with rotational degrees of freedom. *Computational Mathematics and Mathematical Physics*, *50*, 2118–2130.

Lauga, E., Michael, B. P., & Stone, H. A. (2005). Microfluidics: the no-slip boundary condition. *arXiv preprint cond-mat/0501557*.

Lemlich, R. (1978). Prediction of changes in bubble size distribution due to interbubble gas diffusion in foam. *Industrial & Engineering Chemistry Fundamentals*, *17*(2), 89–93.

Li, J. (2011). Direct simulation method based on BGK equation. In *Aip conference proceedings* (Vol. 1333, pp. 283–288).

Li, Q., Zeng, J., Huang, Z., & Wu, L. (2023). Kinetic modelling of rarefied gas flows with radiation. *Journal of Fluid Mechanics*, *965*, A13.

Li, Q., Zeng, J., Su, W., & Wu, L. (2021). Uncertainty quantification in rarefied dynamics of molecular gas: rate effect of thermal relaxation. *Journal of Fluid Mechanics*, *917*, A58.

Li, R., Wang, J., & Xia, G. (2021). Theoretical and numerical study of nanoporous evaporation with receded liquid surface: effect of Knudsen number. *Journal of Fluid Mechanics*, *928*, A9.

Li, R., Yan, Z., & Xia, G. (2023). Effect of inter-pore interference on liquid evaporation rates from nanopores by direct simulation Monte Carlo. *Physics of Fluids*, *35*(3).

Li, S., Su, W., Shan, B., Li, Z., Gibelli, L., & Zhang, Y. (2024). Molecular kinetic modelling of non-equilibrium evaporative flows. *Journal of Fluid Mechanics*, *994*, A16.

Li, S., Su, W., & Zhang, Y. (2023). Sound wave propagation in rarefied molecular gases. *Journal of Fluid Mechanics*, *973*, A35.

Lifshitz, I. M., & Slyozov, V. V. (1961). The kinetics of precipitation from supersaturated solid solutions. *Journal of Physics and Chemistry of Solids*, *19*(1-2), 35–50.

Liu, S., Yu, P., Xu, K., & Zhong, C. (2014). Unified gas-kinetic scheme for diatomic molecular simulations in all flow regimes. *Journal of Computational Physics*, *259*, 96–113.

Lulli, M., Biferale, L., Falcucci, G., Sbragaglia, M., & Shan, X. (2022). Mesoscale perspective on the Tolman length. *Physical Review E*, *105*(1), 015301.

Luo, L. (1998). Unified theory of lattice Boltzmann models for nonideal gases. *Physical Review Letters*, *81*(8), 1618.

Luo, L. (2000). Theory of the lattice Boltzmann method: Lattice Boltzmann models for nonideal gases. *Physical Review E*, *62*(4), 4982.

MacPherson, R. D., & Srolovitz, D. J. (2007). The von Neumann relation generalized to coarsening of three-dimensional microstructures. *Nature*, *446*(7139), 1053–1055.

Macrossan, M. N. (2001). A particle simulation method for the BGK equation. In *Aip conference proceedings* (Vol. 585, pp. 426–433).

Mandelshtam, L. I., & Leontovich, M. A. (1937). A theory of sound absorption in liquids. *Journal of Experimental and Theoretical Physics*, *7*(3), 438–449.

Marqusee, J., & Ross, J. (1984). Theory of Ostwald ripening: Competitive growth and its dependence on volume fraction. *The Journal of Chemical Physics*, *80*(1), 536–543.

Mason, E. A., & Monchick, L. (1962). Heat conductivity of polyatomic and polar gases. *The Journal of Chemical Physics*, *36*(6), 1622–1639.

Maxwell, J. C. (1878). Iii. On stresses in rarefied gases arising from inequalities of temperature. *Proceedings of the Royal Society of London*, *27*(185-189), 304–308.

McCormack, F. J. (1968). Kinetic equations for polyatomic gases: the 17-moment approximation. *The Physics of Fluids*, *11*(12), 2533-2543. Retrieved from `https://aip.scitation.org/doi/abs/10.1063/1.1691855` doi: 10.1063/1.1691855

Meland, R., & Ytrehus, T. (2003). Evaporation and condensation Knudsen layers for nonunity condensation coefficient. *Physics of Fluids*, *15*(5), 1348–1350.

Meng, J., Wu, L., Reese, J. M., & Zhang, Y. (2013). Assessment of the ellipsoidal-statistical Bhatnagar–Gross–Krook model for force-driven Poiseuille flows. *Journal of Computational Physics*, *251*, 383–395.

Midya, J., & Das, S. K. (2017). Droplet growth during vapor-liquid transition in a 2D Lennard-Jones fluid. *The Journal of Chemical Physics*, *146*(2).

Mieussens, L. (2000). Discrete-velocity models and numerical schemes for the Boltzmann-BGK equation in plane and axisymmetric geometries. *Journal of Computational Physics*, *162*(2), 429–466.

Mieussens, L., & Struchtrup, H. (2004). Numerical comparison of Bhatnagar–Gross–Krook models with proper Prandtl number. *Physics of Fluids*, *16*(8), 2797–2813.

Montanero, J. M., & Santos, A. (1996). Monte Carlo simulation method for the Enskog equation. *Physical Review E*, *54*(1), 438.

Morse, T. F. (1964). Kinetic model for gases with internal degrees of freedom. *The Physics of Fluids*, *7*(2), 159–169.

Mouhot, C., & Pareschi, L. (2006). Fast algorithms for computing the Boltzmann collision operator. *Mathematics of Computation*, *75*(256), 1833–1852.

Negro, G., Gonnella, G., Lamura, A., Busuioc, S., & Sofonea, V. (2024). Growth regimes in three-dimensional phase separation of liquid-vapor systems. *Physical Review E*, *109*(1), 015305.

Ng, J. D., Lorber, B., Witz, J., Théobald-Dietrich, A., Kern, D., & Giegé, R. (1996). The crystallization of biological macromolecules from precipitates: evidence for Ostwald ripening. *Journal of Crystal Growth*, *168*(1-4), 50–62.

Ohashi, K., Kobayashi, K., Fujii, H., & Watanabe, M. (2020). Evaporation coefficient and condensation coefficient of vapor under high gas pressure conditions. *Scientific Reports*, *10*(1), 8143.

Onsager, L. (1931a). Reciprocal relations in irreversible processes. I. *Physical Review*, *37*(4), 405.

Onsager, L. (1931b). Reciprocal relations in irreversible processes. II. *Physical Review*, *38*(12), 2265.

Onuki, A. (2002). *Phase transition dynamics*. Cambridge University Press.

Pan, X., Shneider, M. N., & Miles, R. B. (2004). Coherent Rayleigh-Brillouin scattering in molecular gases. *Physical Review A—Atomic, Molecular, and Optical Physics*, *69*(3), 033814.

Park, J. H., Bahukudumbi, P., & Beskok, A. (2004). Rarefaction effects on shear driven oscillatory gas flows: A direct simulation Monte Carlo study in the entire Knudsen regime. *Physics of Fluids*, *16*(2), 317–330.

Persad, A. H., & Ward, C. A. (2016). Expressions for the evaporation and condensation coefficients in the Hertz-Knudsen relation. *Chemical Reviews*, *116*(14), 7727–7767.

Perumanath, S., Borg, M. K., Chubynsky, M. V., Sprittles, J. E., & Reese, J. M. (2019). Droplet coalescence is initiated by thermal motion. *Physical Review Letters*, *122*(10), 104501.

Pinto, G., Silva, F., Porteiro, J., Míguez, J., & Baptista, A. (2018). Numerical simulation applied to PVD reactors: An overview. *Coatings*, *8*(11), 410.

Pöschel, T., & Schwager, T. (2005). *Computational granular dynamics: models and algorithms*. Springer Science & Business Media.

Rahimi, B., & Struchtrup, H. (2014). Capturing non-equilibrium phenomena in rarefied polyatomic gases: A high-order macroscopic model. *Physics of Fluids*, *26*(5).

Richardson, S. (1973). On the no-slip boundary condition. *Journal of Fluid Mechanics*, *59*(4), 707–719.

Roohi, E., Stefanov, S., Shoja-Sani, A., & Ejraei, H. (2018). A generalized form of the Bernoulli Trial collision scheme in DSMC: Derivation and evaluation. *Journal of Computational Physics*, *354*, 476–492.

Roy, S., & Das, S. K. (2012). Nucleation and growth of droplets in vapor-liquid transitions. *Physical Review E*, *85*(5), 050602.

Rykov, V. A. (1975). A model kinetic equation for a gas with rotational degrees of freedom. *Fluid Dynamics*, *10*(6), 959–966.

Schrage, R. W. (1953). A theoretical study of interphase mass transfer. In *A theoretical study of interphase mass transfer.* Columbia University Press.

Shakhov, E. M. (1968). Generalization of the Krook kinetic relaxation equation. *Fluid Dynamics*, *3*(5), 95–96.

Shan, B., Su, W., Gibelli, L., & Zhang, Y. (2023). Molecular kinetic modelling of non-equilibrium transport of confined van der Waals fluids. *Journal of Fluid Mechanics*, *976*, A7.

Shan, X., & Chen, H. (1993). Lattice Boltzmann model for simulating flows with multiple phases and components. *Physical Review E*, *47*(3), 1815.

Shan, X., & Chen, H. (1994). Simulation of nonideal gases and liquid-gas phase transitions by the lattice Boltzmann equation. *Physical Review E*, *49*(4), 2941.

Sharipov, F. (2006). Onsager-Casimir reciprocal relations based on the Boltzmann equation and gas-surface interaction: Single gas. *Physical Review E*, *73*(2), 026110.

Sharipov, F., & Kalempa, D. (2008). Numerical modeling of the sound propagation through a rarefied gas in a semi-infinite space on the basis of linearized kinetic equation. *The Journal of the Acoustical Society of America*, *124*(4), 1993–2001.

Sharipov, F., Marques Jr, W., & Kremer, G. M. (2002). Free molecular sound propagation. *The Journal of the Acoustical Society of America*, *112*(2), 395–401.

Shavaliyev, M. S. (1993). Super-Burnett corrections to the stress tensor and the heat flux in a gas of Maxwellian molecules. *Journal of Applied Mathematics and Mechanics*, *57*(3), 573–576.

Sibold, D., & Urbassek, H. M. (1993). Monte Carlo study of Knudsen layers in evaporation from elemental and binary media. *Physics of Fluids A: Fluid Dynamics*, *5*(1), 243–256.

Sobrino, L. d. (1967). On the kinetic theory of a van der Waals gas. *Canadian Journal of Physics*, *45*(2), 363–385.

Sone, Y. (1988). Steady evaporation and condensation on a plane condensed phase. *Theoretical and Applied Mechanics*.

Struchtrup, H. (2012). Resonance in rarefied gases. *Continuum Mechanics and Thermodynamics*, *24*, 361-376. doi: 10.1007/s00161-011-0202-0

Su, W., Gibelli, L., Li, J., Borg, M., & Zhang, Y. (2023). Kinetic modeling of nonequilibrium flow of hard-sphere dense gases. *Physical Review Fluids*, *8*(1), 013401.

Su, W., Li, Q., Zhang, Y., & Wu, L. (2022). Temperature jump and Knudsen layer in rarefied molecular gas. *Physics of Fluids*, *34*(3), 032010.

Su, W., Wang, P., Zhang, Y., & Wu, L. (2020). Implicit discontinuous Galerkin method for the Boltzmann equation. *Journal of Scientific Computing*, *82*, 1–35.

Su, W., Zhang, Y., & Wu, L. (2021). Multiscale simulation of molecular gas flows by the general synthetic iterative scheme. *Computer Methods in Applied Mechanics and Engineering*, *373*, 113548.

Takata, S., Matsumoto, T., & Hattori, M. (2021). Kinetic model for the phase transition of the van der Waals fluid. *Physical Review E*, *103*(6), 062110.

Takata, S., & Noguchi, T. (2018). A simple kinetic model for the phase transition of the van der Waals fluid. *Journal of Statistical Physics*, *172*, 880–903.

Tang, H., Cheng, P., & Xu, K. (2001). Numerical simulations of resonant oscillations in a tube. *Numerical Heat Transfer: Part A: Applications*, *40*(1), 37–54.

Tantos, C., Ghiroldi, G. P., Valougeorgis, D., & Frezzotti, A. (2016). Effect of vibrational degrees of freedom on the heat transfer in polyatomic gases confined between parallel plates. *International Journal of Heat and Mass Transfer*, *102*, 162–173.

Tateno, M., & Tanaka, H. (2021). Power-law coarsening in network-forming phase separation governed by mechanical relaxation. *Nature Communications*, *12*(1), 912.

Tcheremissine, F. G., & Agarwal, R. K. (2008). Computation of hypersonic shock waves in diatomic gases using the generalized Boltzmann equation. In *AIP Conference Proceedings* (Vol. 1084, pp. 427–433).

Tenti, G., Boley, C. D., & Desai, R. C. (1974). On the kinetic model description of Rayleigh–Brillouin scattering from molecular gases. *Canadian Journal of Physics*, *52*(4), 285–290.

Tisza, L. (1942a). Supersonic absorption and Stokes' viscosity relation. *Physical Review*, *61*(7-8), 531.

Tisza, L. (1942b). Supersonic absorption and Stokes' viscosity relation. *Physical Review*, *61*(7-8), 531.

Tolman, R. C. (1949). The effect of droplet size on surface tension. *Journal of Chemical Physics*, *17*(3), 333–337.

Torrilhon, M. (2016). Modeling nonequilibrium gas flow based on moment equations. *Annual Review of Fluid Mechanics*, *48*(1), 429–458.

Vaartstra, G., Lu, Z., Lienhard, J. H., & Wang, E. N. (2022). Revisiting the Schrage equation for kinetically limited evaporation and condensation. *Journal of Heat Transfer*, *144*(8), 080802.

Vaartstra, G., Zhang, L., Lu, Z., Díaz-Marín, C. D., Grossman, J., & Wang, E. (2020). Capillary-fed, thin film evaporation devices. *Journal of Applied Physics*, *128*(13), 130901.

Voorhees, P. W. (1985). The theory of Ostwald ripening. *Journal of Statistical Physics*, *38*, 231–252.

Voorhees, P. W. (1992). Ostwald ripening of two-phase mixtures. *Annual Review of Materials Science*, *22*(1), 197–215.

Wagner, A. J., & Cates, M. E. (2001). Phase ordering of two-dimensional symmetric binary fluids: A droplet scaling state. *Europhysics Letters*, *56*(4), 556.

Wagner, C. (1961). Theorie der alterung von niederschlägen durch umlösen (ostwald-reifung). *Zeitschrift für Elektrochemie, Berichte der Bunsengesellschaft für physikalische Chemie*, *65*(7-8), 581–591.

Wagner, W. (1992). A convergence proof for bird's direct simulation Monte Carlo method for the Boltzmann equation. *Journal of Statistical Physics*, *66*, 1011–1044.

Wang, J., Xia, G., & Li, R. (2022). Numerical analysis of evaporation from nanopores using the direct simulation Monte Carlo method. *Journal of Molecular Liquids*, *347*, 118348.

Wang, P., Wu, L., Ho, M. T., Li, Z. H., & Zhang, Y. (2020). The kinetic Shakhov–Enskog model for non-equilibrium flow of dense gases. *Journal of Fluid Mechanics*, *883*, A48.

Wang, P., Zhu, L., Su, W., Wu, L., & Zhang, Y. (2018). Nonlinear oscillatory rarefied gas flow inside a rectangular cavity. *Physical Review E*, *97*(4), 043103.

Wang, R. J., & Xu, K. (2012). The study of sound wave propagation in rarefied gases using unified gas-kinetic scheme. *Acta Mechanica Sinica*, *28*(4), 1022–1029.

Wang, Y., Ubachs, W., & Van De Water, W. (2019). Bulk viscosity of co2 from Rayleigh-Brillouin light scattering spectroscopy at 532 nm. *The Journal of Chemical Physics*, *150*(15).

Wang, Z., Yan, H., Li, Q., & Xu, K. (2017). Unified gas-kinetic scheme for diatomic molecular flow with translational, rotational, and vibrational modes. *Journal of Computational Physics*, *350*, 237–259.

Wang-Chang, C. S., & Uhlenbeck, G. E. (1951). Transport phenomena in polyatomic gases. *Research Rep. CM-681. University of Michigan Engineering*.

Watanabe, H., Suzuki, M., Inaoka, H., & Ito, N. (2014). Ostwald ripening in multiple-bubble nuclei. *The Journal of Chemical Physics*, *141*(23).

Wu, L. (2016). Sound propagation through a rarefied gas in rectangular channels. *Physical Review E*, *94*(5), 053110.

Wu, L. (2022). *Rarefied gas dynamics: kinetic modeling and multi-scale simulation*. Springer Nature.

Wu, L., Li, Q., Liu, H., & Ubachs, W. (2020). Extraction of the translational Eucken factor from light scattering by molecular gas. *Journal of Fluid Mechanics*, *901*, A23.

Wu, L., Liu, H., Reese, J. M., & Zhang, Y. (2016). Non-equilibrium dynamics of dense gas under tight confinement. *Journal of Fluid Mechanics*, *794*, 252–266.

Wu, L., Reese, J. M., & Zhang, Y. (2014). Oscillatory rarefied gas flow inside rectangular cavities. *Journal of Fluid Mechanics*, *748*, 350–367.

Wu, L., White, C., Scanlon, T. J., Reese, J. M., & Zhang, Y. (2013). Deterministic numerical solutions of the Boltzmann equation using the fast spectral method. *Journal of Computational Physics*, *250*, 27–52.

Wu, L., White, C., Scanlon, T. J., Reese, J. M., & Zhang, Y. (2015). A kinetic model of the Boltzmann equation for non-vibrating polyatomic gases. *Journal of Fluid Mechanics*, *763*, 24–50.

Wu, L., Zhang, Y., & Reese, J. M. (2015). Fast spectral solution of the generalized Enskog equation for dense gases. *Journal of Computational Physics*, *303*, 66–79.

Yang, J. Y., & Huang, J. C. (1995). Rarefied flow computations using nonlinear model Boltzmann equations. *Journal of Computational Physics*, *120*(2), 323–339.

Yang, M., & Sheng, P. (2017). Sound absorption structures: From porous media to acoustic metamaterials. *Annual Review of Materials Research*, *47*, 83–114.

Yang, Y., Cui, G., & Lan, C. Q. (2019). Developments in evaporative cooling and enhanced evaporative cooling-A review. *Renewable and Sustainable Energy Reviews*, *113*, 109230.

Yao, J. H., Elder, K. R., Guo, H., & Grant, M. (1993). Theory and simulation of Ostwald ripening. *Physical Review B*, *47*(21), 14110.

Yec, C. C., & Zeng, H. C. (2014). Synthesis of complex nanomaterials via Ostwald ripening. *Journal of Materials Chemistry A*, *2*(14), 4843–4851.

Ytrehus, T. (1997). Molecular-flow effects in evaporation and condensation at interfaces. *Multiphase Science and Technology*, *9*(3).

Zhang, Q., Zhuo, C., Mu, J., Zhong, C., & Liu, S. (2023). A multiscale discrete velocity method for diatomic molecular gas. *Physics of Fluids*, *35*(7).

Zhang, Y., Xu, A., Qiu, J., Wei, H., & Wei, Z. (2020). Kinetic modeling of multiphase flow based on simplified Enskog equation. *Frontiers of Physics*, *15*, 1–13.